Understanding of Road-Bioretention Strip Design and Improvement from Hydraulic Perspective

by

Xiaoning Li

A dissertation submitted to the Graduate Faculty of

Auburn University

in partial fulfillment of the

requirements for the Degree of

Doctor of Philosophy

Auburn, Alabama

August 03, 2019

Keywords: Time of concentration; Curb inlet efficiency; Road bioretention design; Overland flow simulation; Particle tracking method; Impervious and pervious surface

Approved by

Xing Fang, Arthur H. Feagin Chair Professor of Civil Engineering

Jose G. Vasconcelos, Associate Professor of Civil Engineering

Frances O'Donnell, Assistant Professor of Civil Engineering

Jeyhoon (Jay) M. Khodadadi, Professor of Mechanical Engineering

Qinghua (Peter) He, Associate Professor of Chemical Engineering

Abstract

This study is to understand and quantify the hydraulic and hydrological performance of road bioretention facilities as well as the basic problems in urban drainage and road bioretention design. An open-source two-dimensional flow simulation program, FullSWOF_2D, which fully (Full) solves shallow water (SW) equations for overland flow (OF) and river flow, was updated and applied to this study. The particle tracking method (PTM) module was first added into FullSWOF_2D program to estimate the time of concentration (T_c) for impervious and pervious surfaces. The updated program FullSWOF-PTM was applied to 446 impervious modeling cases to simulate and calculate T_{ci} of overland flow on impervious surfaces. T_{ci} equation derived using PTM correlates well with T_{ci} from other five published equations, which proves PTM can also be used to estimate T_{cp} of overland flow on pervious surfaces. Seven hundred fifty (750) pervious modeling cases were developed and simulated to explore the T_{cp} equation. A regression equation for T_{cp} was developed and has higher accuracy compared to Akan's equation wide ranges of input parameters.

The FullSWOF_2D program was also revised to include 2D plane zones with different rainfall and infiltration parameters and a 2D-1D grate inlet flow interception module. The updated program called FullSWOF-ZG was tested with 20 locally depressed Texas type D curb inlet cases to simulate the inlet efficiency (E_{ci}). It was also validated with 80 laboratory tests to simulate the curb inlet length of 100% interception (L_T). These validation runs indicated that the FullSWOF-ZG program can be used to determine L_T and E_{ci}. One thousand (1000) undepressed curb inlet modeling cases of the road with 10 longitudinal slopes S_0, 10 cross slopes S_x, and 10 upstream inflows Q_{in} were established and modeled to

determine L_T. The second 1000 road modeling cases of undepressed curb inlet with 10 S_0, 10 S_x, and 10 curb inlet opening lengths L_{ci} and constant Q_{in} (10 L/s) were established and modeled to determine E_{ci}. Two new regression equations of L_T and E_{ci} were developed and compared with three previous methods, and the newly developed equations give more accurate estimations of L_T and E_{ci} over a wide range of input parameters and can be applied to design urban drainage and road bioretention facilities.

Twenty road-bioretention strip (RBS) modeling cases were designed based on the commonly used parameters and evaluated using FullSWOF-ZG. The simulation results were analyzed and demonstrated that the RBS's hydrological performance was jointly influenced by several parameters such as road gemoetry, inlet design and efficiency, bioretention infiltration capacity, and overflow discharge capacity. When the road, curb inlet, and bioretention strip were modeled together as an integral system, it was found that the RBS's curb inlet could be the bottleneck of RBS's hydrologic performance and should be designed based on hydraulic calculation. The curb inlet and road grate inlet combination is necessary for continuous RBS because the road surface runoff could not be 100% intercepted by the curb inlet alone.

The FullSWOF-ZG program was applied to explore whether the deep cut over the curb and the road-curb cut inlets can improve the curb-inlet's efficiency E_{ci}. The deep-cut curb inlets were used in some retrofitting projects for improving E_{ci}. However, the simulation results show that the E_{ci} improvement of the deep cut over the curb inlet only is very small compared to corresponding undepressed curb inlet. The curb inlets with the road-curb deep cuts were also simulated, and it proved that the curb inlets with the road-cut width = 0.10 m could improve the efficiency compared to the undepressed curb inlets.

Acknowledgments

I would like to deeply thank my academic advisor, Dr. Xing Fang, for providing me the opportunity to purse my Ph.D. degree under his guidance. I really appreciate his support, continuous encouragement, patience and guidance he has shown towards me in accomplishing my goals.

I am also equally thankful to my graduate committee members: Dr. Jose G. Vasconcelos, Dr. Jay Khodadadi, Dr. Frances O'Donnell, and the university reader Dr. Qinghua (Peter) He for their valuable time to review my dissertation and provide the insights and suggestions on my research problems and motivating me which substantially improved my research and study.

I would also like to acknowledge my friends Gang Chen, Liping Jiang, Xueqian Li, and Yun Yan during my research at Auburn University. I wish to express my gratitude to the Chinese Scholarship Council for financial support pursuing my graduate study at Auburn University.

Finally, I would like to express my sincere gratitude and appreciation to my parents and an older sister who have supported me tirelessly throughout my study period. Without your love, care, and encouragement I would not have been capable of completing this study. I am blessed to be surrounded by such a good support system at home, school, and work.

Table of Contents

List of Tables

List of Figures

List of Abbreviations

BMP	Best Management Practice
D_b	bioretention depth
DEM	digital elevation model
E_{ci}	curb inlet interception efficiency
f	bioretention infiltration rate
F	cumulative infiltration depth
h_b	overflow height
HEC-22	Urban Drainage Design Manual: Hydraulic Engineering Circular No. 22
h_{max}	bioretention maximum ponding depth
K	saturated hydraulic conductivity
φ	suction head
ΔE	differences of simulated and observed interception efficiencies
$\Delta\theta$	moisture deficit
ΔV	the percent difference between simulated RBS runoff volume and rainfall volume
ΔV_p	percent difference of simulated and observed runoff volume
ΔV_{rb}	the percent difference between simulated bioretention runoff volume and rainfall volume
ΔV_{rd}	the percent difference between simulated road runoff volume and rainfall volume
ΔQ_p	percent difference in simulated peak discharge
L	upstream catchment length
L_{ci}	curb inlet length
LID	Low impact development
L_T	theoretical curb-inlet length required to intercept 100% of the flow
NSE	Nash-Sutcliffe Efficiency
P_{bp}	percent of bypass runoff volume
P_{ci}	percent of runoff volume intercepted by curb inlet
PD_E	percent differences in simulated and observed intercepted efficiencies
P_{inf}	percent of bioretention cumulative infiltration volume
P_{rg}	percent of road grate inlet captured runoff volume
Q_{bp}	the remainder of runoff discharged downstream along the road
Q_{ci}	road runoff intercepted by the curb inlet
Q_{cio}	observed curb intercepted flow rate
Q_{cis}	simulated curb intercepted flow rate
Q_i	total inflow rate
Q_{og}	overflows runoff through the bioretention grate inlet

Q_{pbp}	peak discharges of the bypass flow
Q_{po}	observed peak runoff rate
Q_{pog}	overflow grate inlet peak discharge
Q_{prg}	peak discharges of the grate inlet
Q_{prgb}	road grate inlet peak discharge for RBS cases
Q_{ps}	simulated peak runoff rate
Q_{rg}	road runoff captured by the road grate inlet
RBS	Road-bioretention strip
S_0	longitudinal slopes of the road/street
SPC	Sponge city
SWEs	Shallow-Water Equations
S_x	cross slope of the road/street
T_{bog}	bioretention overflow-start-time
V_{bio}	bioretention ponding runoff volume
$V_{bio}(t)$	runoff volume stays in the bioretention strip
V_{bog}	bioretention overflow grate inlet discharge volume
V_{bp}	bypass runoff volume
V_{ci}	runoff volume intercepted by curb inlet
V_{inf}	bioretention cumulative infiltration volume
V_{ob}	observed total runoff volume
V_{pc}	calculated bioretention ponding volume
V_r	calculated rainfall volume
V_{rb}	runoff generated on the bioretention surface from rainfall
V_{rd}	road rainfall volume
V_{rg}	runoff volume captured by the road grate inlet
V_{si}	simulated total runoff volume
V_{srd}	simulated road runoff volume
y_b	bioretention water depth

Chapter 1. Introduction

1.1 Background

Over the past 40 years to 2016, China's urban population rose from 17.6% in 1977 to 57.4% of its total population, which led to rapid urbanization, and this trend will keep increasing by 1% per year to reach approximately 60% by 2020 (China, 2017). Consequently, different city syndromes, such as water shortage, water pollution, flood inundation, and ecologic deterioration, have happened frequently over the past decades, causing huge economic loss and becoming large obstacles to sustainable development in China (China, 2017; Li et al., 2017) as well as in other parts of the world (Cheshmehzangi, 2016; Moglen, 2009; Todeschini, 2016). The national New-type Urbanization Plan (2014–2020) (China, 2014) was launched in March 2014 by the Chinese central government and emphasized environmental-friendly and sustainable urbanization approaches as an important component of the blueprint (Cheshmehzangi, 2016). To endorse the sustainable urbanization plan, the Sponge City (SPC) paradigm based on green and gray stormwater management infrastructure integration was announced in 2013 as a relief countermeasure to city syndromes in China (Jia et al., 2016; Li et al., 2016; Yu and Jia, 2016).

As an important and typical practice, road bioretention facilities, which combine green/gray infrastructures to facilitate road runoff control through infiltration and storage, remove certain contaminants and sediments, and decrease roads' local flood inundation risk, are widely used in the pilot Sponge City construction in China (Li et al., 2016) and all over the world. A continuous road bioretention strip (RBS) (Figures 1.1a) is built along an urban road or street over a relatively long distance and could be separated into several

cells/units by check dams (berms) when the longitudinal slope is large enough. Figure 1.1 (b) and (c) show two RBS projects in two SPC pilot cities, indicating that road-bioretention systems are widely built in China. Different from right-of-way individual bioretention cells constructed in the USA, road-bioretention projects in SPC pilot cities are always very long along the roadside and are combined with tree planters (Li et al., 2016).

Figure 1.1. (**a**) Schematic diagram of a continuous road-bioretention strip. (**b**) and (**c**) road-bioretention strips constructed in China with red box showing the curb inlet.

Different types of curb inlets (outlined by red rectangles in Figure 1.1) have been used in different projects while no guidance for designing curb inlets of the RBS systems is available. Continuous RBS performance on intercepting road runoff and reducing local flooding under different rainfall events or upstream inflows is still unclear. Key design parameters of continuous RBS also need to be explored and determined.

A road bioretention strip includes impervious road surface and pervious bioretention strip that are connected through curb inlets (Figure 1.1). To understand the hydraulic and hydrological performance of an RBS system, one has to study overland flow on both impervious and pervious surface, infiltration in bioretention, and flow interception through inlets. The rational equation (Kuichling, 1889) is typically used to determine peak discharge (Q_p) to design urban drainage systems using the time of concentration (T_c) as input. Time of concentration is the runoff travel time from the hydraulically most remote point of the watershed to the outlet. Using the rational equation only is most likely not adequate for understanding and designing an RBS system.

Understanding and quantifying the time of concentration on pervious surface (T_{cp}) were first studied. To understand and estimate T_{cp} for pervious surfaces is particularly important and useful to the smart stormwater management using the lower impact development (LID) and green infrastructures (GI) that promote the infiltration (García Serrana et al., 2017).

Peak discharges and time of concentration are two key parameters used to design urban drainage facilities (Brown et al., 2009) and green infrastructures (Guo, 1998). Bondelid et al. (1982) demonstrated that as much as 75% of the total error in an estimate of the peak discharge could result from errors in the T_c estimation. There are dozens of studies where researchers developed and tested/compared T_c equations (Kibler, 1982; McCuen et al., 1984). Only Akan developed a time of concentration calculation chart (Akan, 1986) and a formula (Akan, 1989) using the Manning's friction law on rectangular pervious plots under constant-intensity rainfall based on the kinematic wave equations and Green-Ampt (GA) (Rawls et al., 1983) infiltration model. The time of concentration in

Akan's study is measured from the beginning of the rainfall event, which means the ponding time (t_p) and runoff travel time were lumped together in the formula. The chart and formula are mainly appropriate for the cases that the Manning's friction law is acceptable and limited ranges of rainfall and soil infiltration parameters. Further work is still needed, e.g., to expand the formula to other flow resistance laws and wide ranges of rainfall and soil infiltration parameters.

Li et al. (2018a) found that the curb inlet could be the bottleneck of road bioretention facilities that impedes the runoff generated from the road flowing into the bioretention to infiltrate, detain (pond), and improve the stormwater quality. Stoolmiller et al. (2018) surveyed curb inlets for road bioretention facilities in Philadelphia, and the curb inlet opening ranged from 0.15 m (6 inches) to 1.52 m (5 ft). Some of these inlets seem to have been designed based on the landscape and safety perspectives, instead of hydraulic performance considering inlet interception efficiency. Therefore, understanding and quantifying hydraulic performance of inlets are important parts of this study.

The hydraulic performance of curb inlets for roadway drainage has been studied for more than 60 years, which was reviewed and summarized by Izzard (1950), Li (1954), and presently systematically documented in the Hydraulic Engineering Circular No. 22 (HEC-22) by Brown et al. (2009). The most recent HEC-22 (Brown et al., 2009) was published and widely used in the USA and refined the design procedures stated in HEC-12. However, most of the currently used curb inlet E_{ci} equations were based on simple theoretical derivation with assumptions and revised coefficients or exponents determined using experimental data. Guo and MacKenzie (2012) stated that the HEC-22 procedure overestimates the capacity of a curb-opening inlet when the water depth is shallow, and

then becomes underestimating when water depth exceeds 7 inches for 3 ft curb inlet in the sump.

To determine inlet efficiency and performance, the reduced-scale physical models were used and based on Froude number scaling—that is, a 3:4 scale model for Hammonds and Holley's study (1995), 1:4 for Uyumaz's research (2002), and 1:3 for Guo and Mackenzie's tests (2012); only Schalla et al. (2017) conducted full-scale experiments for the curb inlet. In this study, full-scale numerical models were used to study the hydraulic performance of curb inlet, which is discussed in more details in section 1.3. The two-dimensional (2D) open source FullSWOF_2D (version 1.07, Dieudonné Laboratory J.A., Polytech Nice Sophia, Nice, France) (Delestre et al., 2014) program based on shallow-water equations (SWEs) could simulate the complex flow through an inlet accurately. The program could be updated and validated to determine the 100% interception curb inlet length (L_T) and efficiency (E_{ci}) with full-scale road curb inlet model established and simulated.

The deep-cut (DC) curb inlets were used in some of the retrofit SPC projects for that they were easily implemented and based on engineer's or design's field experience. The efficiencies of the deep-cut curb inlets in those projects were unknown because there is no standard equation that can be used to calculate their efficiencies. Two kinds of retrofit scenarios were simulated in this study (Figure 1.2): 1) the deep cut is made only over the width of the curb inlet (Figure 1.2b); 2) both the curb inlet and a small part of road surface have a deep cut (Figure 1.2c). Compared to undepressed curb inlets, the composite-cross-slope curb inlets with larger cross slope at the gutter have larger interception capacity for the road-bioretention strips (Brown et al., 2009). However, the performance of the UD curb

inlets with two kinds of deep cuts (Figure 1.2b and Figure 1.2c) was still not quantified in previous studies. The FullSWOF-ZG program could be used to establish full-scale modeling cases for the deep cut curb inlets to explore and quantify the efficiency improvement by cutting the curb inlet simply.

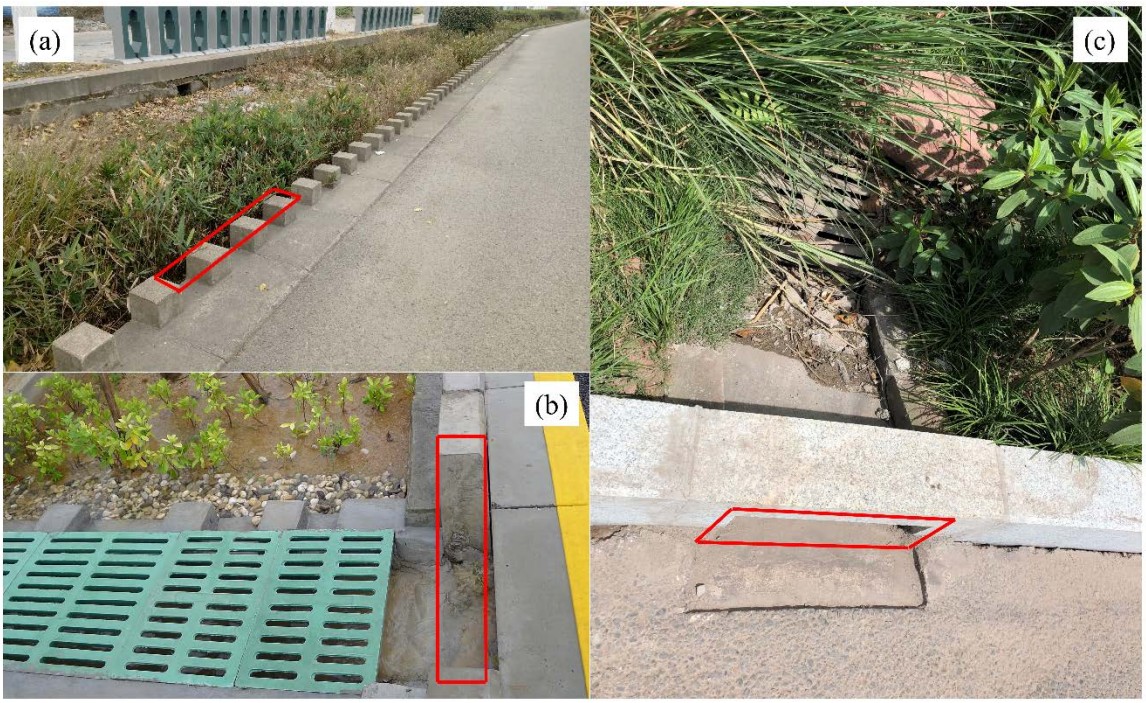

Figure 1.2. (**a**) Undepressed curb inlet, (**b**) the deep cut over the curb inlet width only, (**c**) the deep cut over the curb inlet and a small part of the road surface. Photos (**b**) and (**c**) show these deep cuts have been implemented in sponge city projects.

1.2 Knowledge Gap and Research Objective

The curb inlet of road-bioretention strips should be designed based on the time of concentration and peak design discharge (Q_p) for the upstream contribution catchment area. The T_c value of upstream contribution catchment area is important to find the required curb inlet length for road-bioretention strips based on the design Q_p and curb inlet interception efficiency. Empirical equations to determine T_c for impervious road surface are available,

but for pervious surfaces of bioretention cell, only Akan (1989) provided an equation for T_{cp} that is limited to a small range of soil infiltration parameters. A more applicable T_{cp} estimation equation should be developed to use for LID facility design and software such as EPA-SWMM.

The estimation equation of curb inlet interception efficiency under different rainfall-runoff conditions is needed for road-bioretention strip design. However, curb inlet equations were mainly developed either to fit solely to experimental data using multiple variable regression (Fiuzat et al., 2000; MacCallan and Hotchkiss, 1996) or to derive theoretical equation form and determine coefficients and exponents using experimental data (Mark Alan Hammonds and Edward Holley, 1995; Uyumaz, 2002). In previous studies, the reduced-scale physical models were based on Froude number scaling, e.g., 1:4, 1:3, and 3:4 (Guo and MacKenzie, 2012; Mark Alan Hammonds and Edward Holley, 1995; Uyumaz, 2002) or full-scale experiments (Schalla et al., 2017). However, the scaling recently has been discussed as a possible reason for significant discrepancies in equation predictions (Comport and Thornton, 2012; Russo and Gómez, 2013).

The influence of runoff generation and concentration process, curb inlet interception process, bioretention infiltration process, and bioretention overflow process on the performance of road bioretention strips have not been explored and quantified with one single model. The hydraulic performance of curb inlet in bioretention and the hydrologic performance of road bioretention strips such as infiltration process should be evaluated together which treated the road bioretention strips integrally rather than separately.

The deep-cut and road cut curb inlets have been used to retrofit the undepressed curb inlets in China for a number of SPC projects. The performance of the deep cut and road-

curb cut for curb inlets is unknown and should be quantified. The curb inlet efficiency improvement with the deep cut (Figure 1.2) should be explored and quantified with simulation results.

Based on the above knowledge gaps, the objectives of the study are summarized below:

1) Develop a T_{cp} equation of overland flow on pervious surfaces that can be applied to wide ranges of rainfall, watershed (sloping plane), and soil parameters after summarizing and comparing the current time of concentration T_c equations for impervious and pervious surfaces.

2) Develop new equations to evaluate the curb inlet interception efficiency under different upstream inflow conditions based on numerical simulation results.

3) Develop modeling cases of road-bioretention strips based on common situations and evaluate them using the FullSWOF-ZG program to explore key design parameters for the road-bioretention strip system.

4) Quantify the performance improvement (efficiency increase) of curb inlets with the deep cut and the road-curb cut using the FullSWOF-ZG program.

1.3 Fundamental Information on Model and Methods

This study is to design and conduct a series of numerical experiments by solving numerical flow simulation models. Basic information of governing equations and models updated/used is briefly discussed below, and more detail information is given in each chapter for specific applications.

1.3.1 Governing Equations—Shallow Water Equations (SWEs)

As a Saint-Venant system (Barré de Saint-Venant, 1871), the SWEs model is widely used to simulate the incompressible Navier-Stokes flow occurring in rivers, channels, ocean, and land surfaces (Zhang and Cundy, 1989). It is derived with two assumptions, one is the fluid velocity is constant along the vertical (z) direction for that the water depth is much smaller than the horizontal (x, y) dimensions; another is the pressure of the fluid is hydrostatic ($\frac{\partial p}{\partial z} = -g$) which means the pressure field could be calculated with simple integration along the vertical (z) direction (Audusse et al., 2004; Delestre et al., 2014). The conservative form of the 2D SWEs including the continuity equation (with rainfall and infiltration) and two momentum equations for x and y directions are stated as the following equations.

$$\frac{\partial h}{\partial t} + \frac{\partial hu}{\partial x} + \frac{\partial hv}{\partial y} = R - I \tag{1.1}$$

$$\frac{\partial hu}{\partial t} + \frac{\partial}{\partial x}\left(hu^2 + \frac{gh^2}{2}\right) + \frac{\partial}{\partial y}(huv) = gh\left(\frac{\partial z}{\partial x} - S_{fx}\right) \tag{1.2}$$

$$\frac{\partial hv}{\partial t} + \frac{\partial}{\partial x}(huv) + \frac{\partial}{\partial y}\left(hv^2 + \frac{gh^2}{2}\right) = gh\left(\frac{\partial z}{\partial y} - S_{fy}\right) \tag{1.3}$$

Where R (m/s) is the rainfall intensity; I (m/s) is the infiltration rate; h (m) is the cell water depth; z (m) is the cell topography elevation; u (m/s) and v (m/s) are the cell's depth-averaged velocities in x and y directions, respectively; S_{fx} and S_{fy} are the cell's friction slopes in x and y directions, respectively; g (m/s^2) is gravity acceleration; t (s) is time. In hydrologic and hydraulic models, two families of friction laws are mainly used to calculate S_{fx} and S_{fy} based on empirical considerations. On one hand, the friction term could be calculated using the Manning's friction law as the following equation:

$$S_{fx} = C_f \frac{\sqrt{u^2+v^2}}{h^{4/3}} u \qquad S_{fy} = C_f \frac{\sqrt{u^2+v^2}}{h^{4/3}} v \tag{1.4}$$

where $C_f = n^2$ and n is the Manning's coefficient. On the other hand, the friction term could be calculated using the Darcy-Weisbach's friction law as the following equation:

$$S_{fx} = f \frac{\sqrt{u^2+v^2}}{8gh} u \qquad S_{fx} = f \frac{\sqrt{u^2+v^2}}{8gh} v \tag{1.5}$$

where f is the dimensionless Darcy-Weisbach's coefficient.

1.3.2 FullSWOF_2D Program

The FullSWOF_2D program fully solves SWEs on a structured mesh in two space dimensions using the finite volume method (FVM) which ensures mass conservation compared to finite difference method (FDM) (Unterweger et al., 2015). A well-balanced scheme was adapted to guarantee the positivity of water height and the preservation of steady states for specific hydrological features such as during wet-dry transitions and tiny water depth (Cordier et al., 2013; Delestre et al., 2014). Different boundary conditions, friction laws, and numerical schemes were developed which make the program a very powerful overland flow simulation software. The parallelization strategies of FullSWOF_2D were also examined to improve its simulation efficiency when dealing with large-scale cases (Cordier et al., 2013). A modified bi-layer (crust- and soil-layer) Green-Ampt (GA) infiltration model (Esteves et al., 2000) to calculate *I* for Equation (1.1) was coupled in the FullSWOF_2D (Unterweger et al., 2015) which enables the program to simulate overland flow on impervious and pervious surfaces.

FullSWOF_2D has five boundary condition choices including the imposed discharge and water height case, wall condition, Neumann boundary (open boundary) condition,

periodic variations of discharge and water height, and imposed discharge condition. It has three options of friction formulas including the Manning's equation, Darcy-Weisbach equation, and the laminar law, as well as the no friction setting. The simulation domain could be set non-uniformly by defining the friction value of every computational cell with an input file. The Rusanov flux, Harten-Lax-Van Leer (HLL) flux, Harten-Lax-Van Leer with Contact surface (HLLC) flux, HLL2, and HLLC2 (Delestre et al., 2014) methods are provided to calculate every time-level flux between computational cells. Three linear reconstruction methods include the MUSCL, ENO (essentially non-oscillatory), and modified ENO, as well as three slope limiters, include the classical Minmod slope limiter, Van Albada limiter, and Van Leer's limiter are used in the reconstruction part of the 2nd order numerical scheme. The details about the numerical flux, reconstruction methods, and the limiters could be found in Bouchut's (2004) book.

The FullSWOF_2D has been validated using several analytical solutions and benchmarks of the steady-state solutions and the transitory solutions. The steady-state solutions validated by FullSWOF_2D include the emerged bump at rest and Mac Donald test cases with different settings. The transitory solutions include the dam break on a dry domain and Thacker test case with a planar surface in paraboloid (Delestre et al., 2013). It is also widely used in the river flood simulation in a complex environment based on high-resolution topographic data (Abily et al., 2016b) and spatial global sensitivity analysis of high resolution classified topographic data in 2D urban flood modeling (Abily et al., 2016a).

FullSWOF_2D was the primary model used in this study and coded using C++. Even some updates and additional functions, which will be discussed in the next few subsections,

were added by the author, the basic solver for SWEs was not altered. This study is not to improve the basic solver of FullSWOF_2D.

1.3.3 Mathematical Property and Numerical Treatment of Boundary Condition

The one-dimensional homogeneous equations of shallow-water equations could be rewritten using vectors in the following format:

$$\frac{\partial W}{\partial t} + \frac{\partial F(W)}{\partial x} = 0 \tag{1.6}$$

where $W = \begin{pmatrix} h \\ hu \end{pmatrix}$, $F(\mathrm{W}) = \begin{pmatrix} hu \\ hu^2 + \frac{gh^2}{2} \end{pmatrix}$ being the flux terms of the equation. The transport of W is more clearly evidenced in the following non-conservative form:

$$\frac{\partial W}{\partial t} + A(W)\frac{\partial W}{\partial x} = 0 \tag{1.7}$$

where $A(W) = F'(W) = \begin{pmatrix} 0 & 1 \\ -u^2 + gh & 2u \end{pmatrix}$ is the matrix of transport coefficients. The matrix $A(W)$ turns out to be diagonalizable with eigenvalues $\lambda_1(W) = u - \sqrt{gh} < u + \sqrt{gh} = \lambda_2(W)$. The equations is called strict hyperbolicity if the matrix have two real and distinct eigenvalues (Godlewski and Raviart, 2013). The eigenvalues are the velocities of the surface waves of the fluid which are the fundamental characteristics of the flow. The eigenvalues coincide if $h = 0$ which is for dry zones. Therefore, the system will no longer hyperbolic which induces difficulties at both the theoretical and numerical levels.

The flow could be classified based on the relative values of the velocities of the fluid, u, and of the waves, $\sqrt{gh}$. The characteristics velocities $u - \sqrt{gh}$ and $u + \sqrt{gh}$ have opposite signs if $|u| < \sqrt{gh}$, and information propagates upward as well as downward; the flow is said to be subcritical. In contrast, all the information propagates downward when $|u| > \sqrt{gh}$, and the flow is said to be supercritical.

For boundary condition treatment, the SW equations have two unknowns h and u (or equivalently, h and $q = hu$) to solve, a subcritical flow is determined by one upstream value and one downstream value while a supercritical flow completely determined by the two upstream values. Therefore, only one of the two variables for a subcritical inflow/outflow boundary was used for numerical simulations. For a supercritical inflow boundary, both variables should be provided and set for numerical simulations. For a supercritical outflow boundary, the Neumann free-boundary conditions were considered which was introduced in the report conducted by Bristeau and Coussin (2001). In this case, it is necessary to determine whether the flow is subcritical or supercritical. In FullSWOF_2D, there are two quantities calculated to determine whether the flow is subcritical or supercritical. The first quantity is the Froude number for every computation cell:

$$F_r = \frac{|u|}{\sqrt{gh}} \tag{1.8}$$

The flow is subcritical or supercritical if $F_r < 1$ or $F_r > 1$, respectively. Another criterion is obtained through the so-called critical depth h_c, which can be calculated as:

$$h_c = \frac{|q|}{\sqrt{g}}^{2/3} \tag{1.9}$$

for a given discharge $q = hu$. The flow is subcritical or supercritical if $h > h_c$ or $h < h_c$, respectively.

1.3.4 Particle Tracking Method (PTM) and FullSWOF-PTM

The PTM is a powerful method to study the characteristics of complex flow velocity fields during steady and transient-state using simulated velocities from flow governing equations, e.g., Equations (1.1), (1.2), and (1.3) for shallow overland flow. It is widely used in different research areas especially the groundwater flow and pollutant transport study (Cordes and Kinzelbach, 1992). Most of the commonly used PTMs provide satisfactory results for steady-state analysis (Pollock, 1994). PTMs could also be used for transient analysis under the assumption that the velocity field does not significantly change during the simulation duration. In Cheng's study (1996), a PTM was developed based on the Lagrangian-Eulerian finite element method which could reduce the numerical errors considerably and enable the PTM to trace fictitious particles in a complex flow field. It is suggested that the PTM could be extended to transient simulations by tracking velocity calculated with the velocity field of previous time level and current time level (stepwise approximation) when the finite element method (FEM) is used to solve the transport equations. Bensabat et al. (2000) and Lu (1994) developed a linear temporal interpolation scheme instead of a stepwise temporal approximation to count for the changes in velocity during a time step in complex unsteady flow while it is only suited to the FDM rather than FEM or FVM. The travel time and the path lines could be generated using PTM directly incorporated with the overland flow simulation velocity field results.

In the previous study (KC and Fang, 2015), the PTM using simulated velocities from DWM was developed to determine the travel time of different percentage particles arrival

at the outlet. The travel time of each particle in the simulation domain is computed using the PTM module that uses flow velocity fields simulated by the quasi-two-dimensional DWM at every time level. Over each time step, the particle travel distance is determined by the product of the appropriate tracking velocity (interpolated by linear spatial method) and time step interval. In this study, a PTM module was incorporated with FullSWOF_2D using simulated velocity field at each time step, and the updated program becomes FullSWOF-PTM. A fourth-order Runge-Kutta (RK4) spatial interpolation scheme rather than a linear spatial interpolation scheme (Pollock, 1994) was adapted to get the particle velocity at each time step at different locations of the simulation domain. The temporal change of all particles was calculated and updated using the simulated particle velocity and the time interval at every time step.

The following algorithm is implemented in the PTM code of FullSWOF-PTM at each time step. 1) The particle location is checked to determine whether it is within the simulation domain. If the particle arrives at the outlet cell, it is ignored, and the tracking process moves on to the next particle. 2) The computational cell that the particle locates in and the adjacent cell for each particle is determined based on the particle location. 3) The particle velocities in *x*- and *y*-directions are spatially interpolated using an RK4 scheme based on the simulated *x* and *y* velocities of the cell that the particle locates in and adjacent computational cells at the time step. 4) The new locations of all particles are calculated and updated using the previous location, current particle velocities, and time step interval. 5) The particle with the new location is checked again to determine whether it stays in the simulation domain or arrives at the outlet cell and gets out of the domain. 6) The percentage of particles remained in the simulation domain is counted. The particle evolution

information of each time step including the total number and percentage of particles remained in the simulation domain is outputted during the whole simulation period with FullSWOF-PTM. A user interface for FullSWOF-PTM was developed using Matlab r2017a (2017) to run all impervious and pervious cases in batches.

1.3.5 FullSWOF-ZG Program

The FullSWOF-ZG program includes the rainfall input and the infiltration determination by zone and a new 2D-1D drainage inlet submodule. Therefore, the program can simulate impervious road and pervious bioretention surfaces with different infiltration capabilities simultaneously. The simulation domain can have several grate inlets; therefore, the 2D overland flow can drain into these 2D grate inlets (rectangles) to become a 1D flow in underground drainage pipes. Currently, the FullSWOF-ZG program does not further simulate the 1D flow in the drainage pipes, assuming the pipe capability is large enough to accept all inflow from inlets (Brown et al., 2009). The simulation domain has curb inlets connecting the road (impervious surface) and the RBS. Normally, the runoff on the road flows through the curb inlet(s) into the RBS. Only under extreme conditions would the runoff in the RBS be able to flow back to the road, but the extreme conditions were not simulated in this study.

1.3.6 Full-Scale Numerical Experiment Models

The full-scale numerical-experiment models of road-surface and road bioretention cases under different situations were build up in this study to develop the new equations for the time of concentration, inlet efficiencies, and 100% interception inlet length that can be used in road bioretention design and evaluation. The two-dimensional overland flow

simulation model FullSWOF_2D is based on the digital elevation model (DEM) to accurately describe the geometry dimension and elevation changes of the impervious and pervious surfaces. All DEMs for all numerical models established for this study are the full-scale model. When Manning's roughness coefficients were used for FullSWOF_2D model validation, laboratory determined roughness coefficients were used.

In Chapter 2, the full-scale numerical-experiment models of overland flow surfaces with different longitudinal slopes, lengths, and roughness representing for 1-dimensional impervious and pervious surfaces were built up to develop the time of concentration calculate equations which could be used for road bioretention design.

In Chapter 3, the models for the road with undepressed curb opening inlet under different longitudinal slopes, cross slopes, and upstream inflows representing for two-dimensional impervious road surfaces were built up. New equations used to evaluate curb intercept efficiency were developed based on the model results.

In Chapter 4, the models for road bioretention strips that combined impervious and pervious surfaces under different road and bioretention configurations were also developed. The main factors of road bioretention design and evaluation were promoted based on the simulation results.

In Chapter 5, the models for roads with the deep-cut curb inlet and the road-curb-cut curb inlets (Figure 1.2) were built up. The deep-cut and road-curb-cut curb inlets are two kinds of curb inlets commonly used in the road bioretention retrofit projects in China. The performance of these two kinds of curb inlets was determined based on the model results.

1.3.7 Flow Simulation Regions and Model Convergence

The FullSWOF_2D program could deal with the mixed subcritical and supercritical flow on the road surface and through the curb inlet. Compared to kinematic wave and diffusive wave approaches or other approximation (Gourbesville et al., 2014; Teng et al., 2017), the FullSWOF_2D program is stable and efficient in solving the SWEs accurately. The CFL (Courant-Friedrichs-Lewy) condition (Godlewski and Raviart, 2013) was used to ensure the numerical scheme stabilization and convergence. To avoid any loss of information, the numerical speed of propagation $\Delta x/\Delta t$ must be larger than any possible physical velocity.

$$C\frac{\Delta x}{\Delta t^n} \geq \max_i \left[\left|u_i^{n-1}\right| + \sqrt{g h_i^{n-1}}\right] \tag{1.10}$$

C is a parameter depending on the dimension and on the order of the schemes that are considered (in 1D, at the first order, *C* = (0, 1], and, at the second order, *C* = (0, 0.5]; in 2D, at the first order, *C* = (0, 0.5], and, at the second order, *C* = (0, 0.25]. Thus, the computation of the time step could be replaced by a sequence of variable time steps Δt^n according the following rule:

$$\Delta t^n \leq \frac{C\Delta x}{\max_i \left[\left|u_i^{n-1}\right| + \sqrt{g h_i^{n-1}}\right]} \tag{1.11}$$

If the denominator $\max_i \left[\left|u_i^{n-1}\right| + \sqrt{g h_i^{n-1}}\right] \geq 1$, $C\Delta x$ is larger than $\frac{C\Delta x}{\max_i \left[\left|u_i^{n-1}\right| + \sqrt{g h_i^{n-1}}\right]}$, therefore, $\Delta t^n = \frac{C\Delta x}{\max_i \left[\left|u_i^{n-1}\right| + \sqrt{g h_i^{n-1}}\right]}$; otherwise, $C\Delta x$ is smaller than $\frac{C\Delta x}{\max_i \left[\left|u_i^{n-1}\right| + \sqrt{g h_i^{n-1}}\right]}$, then $\Delta t^n = C\Delta x$.

Overall, the following equation is used to calculate the time interval for all simulations:

$$\Delta t^n = C \min\left(\Delta x, \frac{\Delta x}{\max_i\left[\left|u_i^{n-1}\right| + \sqrt{g h_i^{n-1}}\right]}\right) \tag{1.12}$$

where Δt is the time interval of the next time level, C is the Courant number within [0,1], Δx is the space interval of the simulation domain, u_i^{n-1} and h_i^{n-1} are the velocity and water height of computation cell i in current time level, g (m/s^2) is gravity acceleration.

In this study, the Courant number is 0.45 under the consideration of the numerical scheme convergence and computation time-consuming. Before the batch run of 446 impervious surface cases and 750 pervious cases in Chapter 2, the combination of the 2nd order numerical scheme choices were tested with one impervious modeling case (S_0 = 0.05, L = 35 m, n = 0.01, and i = 12.7 mm/hr, domain cells = 560, simulation duration = 390 seconds) using the FullSWOF-PTM program. The best numerical scheme combination was chosen based on the simulation results and time consumption. Finally, the HLL, ENO, and VanLeer combination was chosen as the best numerical scheme for the least time consuming and smallest error. The numerical test results for all combinations are summarized in Table 1.1. The numerical test was conducted using a ThinkStation Desktop with Intel(R) Xeon (R) CPU E3-1241 v3 3.5 GHz. The results also show that the combination of ENOmod with VanAlbada and VanLeer will be oscillated and could not provide reasonable results.

Table 1.2 summarized the mean Froude number (*MFr*) over the simulation domain of the final time step for modeling cases O10X10Q1–O10X10Q10 (S_0 = 1% and S_x =1.5%) with different upstream inflows, which are presented in Chapter 3. *MFr* is calculated using

Equation (1.13). The Froude number (*Fr*) for the first cell of curb inlet is also calculated using Equation (1.8). Simulated water depth and velocities of the first cell at the curb inlet are also summarized in Table 1.2 for modeling cases O10X10Q1–O10X10Q10.

Table 1.1. Numerical test for scheme combinations with case (S_0 = 0.05, L = 35 m, n = 0.01, and i = 12.7 mm/hr, computation cells = 560, simulation duration = 390 sec)

Combination No.	Numerical Flux	Reconstruction	Limiter	Time (sec)	Q_{ps}[1] (L/s)	Q_{pc}[2] (L/s)	Q_{pe}[3] (%)
1	Rusanov	MUSCL	Minmod	32	0.1237	0.1235	0.21
2	Rusanov	MUSCL	VanAlbada	31	0.1235	0.1235	0.03
3	Rusanov	MUSCL	VanLeer	31	0.1236	0.1235	0.14
4	Rusanov	ENO	Minmod	33	0.1237	0.1235	0.18
5	Rusanov	ENO	VanAlbada	34	0.1236	0.1235	0.14
6	Rusanov	ENO	VanLeer	34	0.1237	0.1235	0.20
7	Rusanov	ENOmod	Minmod	34	0.1237	0.1235	0.18
8	Rusanov	ENOmod	VanAlbada	34	0.0007	0.1235	-99.44
9	Rusanov	ENOmod	VanLeer	35	0.0007	0.1235	-99.44
10	HLL	MUSCL	Minmod	36	0.1234	0.1235	-0.02
11	HLL	MUSCL	VanAlbada	37	0.1234	0.1235	-0.03
12	HLL	MUSCL	VanLeer	36	0.1234	0.1235	-0.04
13	HLL	ENO	Minmod	38	0.1234	0.1235	-0.02
14	HLL	ENO	VanAlbada	39	0.1234	0.1235	-0.03
15	HLL	ENO	VanLeer	41	0.1235	0.1235	0.00
16	HLL	ENOmod	Minmod	39	0.1234	0.1235	-0.02
17	HLL	ENOmod	VanAlbada	38	0.0009	0.1235	-99.29
18	HLL	ENOmod	VanLeer	37	0.0009	0.1235	-99.29
19	HLL2	MUSCL	Minmod	32	0.1234	0.1235	-0.02
20	HLL2	MUSCL	VanAlbada	33	0.1234	0.1235	-0.03
21	HLL2	MUSCL	VanLeer	30	0.1234	0.1235	-0.04
22	HLL2	ENO	Minmod	33	0.1234	0.1235	-0.02
23	HLL2	ENO	VanAlbada	33	0.1234	0.1235	-0.03
24	HLL2	ENO	VanLeer	32	0.1235	0.1235	0.00
25	HLL2	ENOmod	Minmod	33	0.1234	0.1235	-0.02
26	HLL2	ENOmod	VanAlbada	33	0.0009	0.1235	-99.29
27	HLL2	ENOmod	VanLeer	32	0.0009	0.1235	-99.29
28	HLLC	MUSCL	Minmod	37	0.1235	0.1235	-0.01
29	HLLC	MUSCL	VanAlbada	37	0.1235	0.1235	-0.02
30	HLLC	MUSCL	VanLeer	36	0.1234	0.1235	-0.03
31	HLLC	ENO	Minmod	40	0.1235	0.1235	-0.01
32	HLLC	ENO	VanAlbada	42	0.1235	0.1235	0.01
33	HLLC	ENO	VanLeer	41	0.1235	0.1235	0.05
34	HLLC	ENOmod	Minmod	41	0.1235	0.1235	-0.01
35	HLLC	ENOmod	VanAlbada	40	0.0008	0.1235	-99.38
36	HLLC	ENOmod	VanLeer	38	0.0008	0.1235	-99.37
37	HLLC2	MUSCL	Minmod	35	0.1235	0.1235	-0.01
38	HLLC2	MUSCL	VanAlbada	33	0.1235	0.1235	-0.02
39	HLLC2	MUSCL	VanLeer	32	0.1234	0.1235	-0.03

40	HLLC2	ENO	Minmod	35	0.1235	0.1235	-0.01
41	HLLC2	ENO	VanAlbada	35	0.1235	0.1235	0.01
42	HLLC2	ENO	VanLeer	36	0.1235	0.1235	0.05
43	HLLC2	ENOmod	Minmod	36	0.1235	0.1235	-0.01
44	HLLC2	ENOmod	VanAlbada	35	0.0008	0.1235	-99.38
45	HLLC2	ENOmod	VanLeer	40	0.0008	0.1235	-99.37

Note: [1] the simulated peak discharge at the end of the simulation domain, [2] calculated peak discharge at the end of the simulation domain using rational method = 1×35×1×12.7/3600, [3] percentage error between simulated and calculated peak discharge = (Q_{ps} - Q_{pc})/ Q_{pc} × 100%.

$$MF_r = \sqrt{\frac{\left(\frac{\sum u_{ij}}{N_x N_y}\right)^2 + \left(\frac{\sum v_{ij}}{N_x N_y}\right)^2}{g\frac{\sum h_{ij}}{N_x N_y}}} \tag{1.13}$$

where u_{ij}, v_{ij}, and h_{ij} are the velocity in *x*- and *y*-direction of computation cell [i][j], and the water height of computation cell [i][j], N_x and N_y are the total computational cells number in *x*- and *y*-direction, and g (m/s^2) is gravity acceleration.

The overall Froude numbers range from 0.31 to 0.46 which are all smaller than 1. This indicates that the overland flow on the road surface for these ten cases are in overall subcritical flow. The velocities for the most of the computation cells are relatively small compared to the celerity of gravity waves ($\sqrt{gh}$) in shallow water of the computation cells. If local Froude number *Fr* is computed for an individual cell, *Fr* could be greater than 1.0 as supercritical flow, especially for the cells inside the curb inlet (Table 1.2), cells over the transition length and the inlet opening of the locally depressed curb inlets (Texas Type C and D inlets). Table 1.2 shows simulated water depth and velocity components (*u* and *v*) at the first cell of curb inlet increase with the increase of discharges (6–24 L/s); the flow dynamics and characteristics are not the focus of this study but should be further explored in future studies, especially for locally depressed curb inlets with upstream/downstream flow transition zones.

The most part of overland flow simulated over the road surface and over the curb inlet is typically a turbulent flow when local Reynolds number $Re = uR_h/v$ is used/calculated and greater than 500 (Chow, 1959), where u is the flow velocity in a cell, R_h is the hydraulic radius that is equal to the water depth for a cell inside the simulation domain, v is the kinematic viscosity of water (10^{-6} m^2/s at 20 ^oC). It is possible that some of cells in the simulation domain have laminar flow when simulated flow depths and velocities are extremely small. In FullSWOF program, when h is less than 10^{-12} m, those cells are considered as dry cells; therefore, the program ignores them or does not solve the SW equations for those cells.

Table 1.2. Summary of mean Froude number and simulated results of 100% interception curb inlet length determination cases O10X10Q1-O10X10Q10 in Chapter 3

Case name	Q_{in} (L/s)	MF_r (-) [1]	h (m) [2]	u (m/s) [2]	v (m/s) [2]	Fr (-) [2]
O10X10Q1	6	0.31	0.024	0.747	0.078	1.539
O10X10Q2	8	0.33	0.027	0.798	0.082	1.545
O10X10Q3	10	0.36	0.030	0.839	0.085	1.550
O10X10Q4	12	0.38	0.033	0.874	0.088	1.555
O10X10Q5	14	0.40	0.035	0.906	0.090	1.560
O10X10Q6	16	0.41	0.037	0.934	0.093	1.564
O10X10Q7	18	0.43	0.039	0.960	0.095	1.568
O10X10Q8	20	0.43	0.040	0.984	0.096	1.572
O10X10Q9	22	0.44	0.042	1.006	0.098	1.576
O10X10Q10	24	0.46	0.043	1.027	0.099	1.580

Note: [1] – mean Froude number, MFr over the simulation domain of the final time step; [2] – simulated results for the first cell of curb inlet at the final time step, h (m) is the cell water depth, u (m/s) and v (m/s) are the cell's velocities along the longitudinal slope and cross slope directions, Fr is the calculated Froude number based on Eequation (1.8) for the first cell of curb inlet.

1.4 Organization of the Dissertation

This dissertation is organized into six chapters. Chapter 1 provides background and introduction information. Chapters 2 to 4 are three journal papers published in *Water* (https://www.mdpi.com/journal/water), free online access peer-reviewed journal with 2017 impact factor of 2.069. Chapter 5 summarizes recent work about curb inlet retrofit simulations that have not been prepared as a journal paper yet. Chapter 6 summarizes the study, promotes the conclusions and suggestions, and provides limitations and future direction of the study.

Related literature review for the study is given in Chapters 2 to 4 for corresponding journal papers. The references for all four papers, Chapter 1 and Chapter 5 were combined, sorted, and listed at the end of the dissertation.

In Chapter 2, the open-source FullSWOF_2D program, which fully solves Shallow Water equations for Overland Flow in 2-Dimensional, was coupled with particle tracking method (PTM) to explore the time of concentration for previous surfaces. New equations used to calculate the time of concentration for pervious and impervious surfaces were developed based on the simulation results. The work of this chapter has been published in *Water* as Paper 1:

> Xiaoning Li, Xing Fang, and Junqi Li et al. “Estimating Time of Concentration for Overland Flow on Pervious Surfaces by Particle Tracking Method”. *Water*, 2018, 10(4): 379, DOI: 10.3390/w10040379.

Chapter 3 built up the full-scale road and curb inlet numerical-experiment model and simulated with updated FullSWOF-ZG program. New equations that can be used to design

the curb inlet in urban drainage and road bioretention facilities were developed based on the simulation results of 1000 modeling cases. The work of this chapter has been published in *Water* as Paper 2:

> Xiaoning Li, Xing Fang, and Gang Chen et al. “Evaluating Curb Inlet Efficiency for Urban Drainage and Road Bioretention Facilities”. *Water*, 2019, 11(4): 851, DOI: 10.3390/w11040851.

In Chapter 4, the full-scale numerical experimental models of twenty road bioretention strips were built up with updated FullSWOF-ZG program. The hydraulic and hydrology performance was evaluated based on the simulated results. The key factors that need consideration in the RBS design were promoted in this chapter. This chapter has been published in *Water* as Paper 3:

> Xiaoning Li, Xing Fang, and Yongwei Gong et al. “Evaluating the Road-Bioretention Strip System from a Hydraulic Perspective—Case Studies”. *Water*, 2018, 10(12): 1778, DOI: 10.3390/w10121778.

In chapter 5, the full-scale numerical models of a road surface including two kinds of curb inlets such as the deep cut over the curb-inlet width and the road-curb cut with two cut widths on the road were build up with FullSWOF-ZG program. The curb inlet efficiencies of those two kinds of curb inlets usually used in the Sponge City retrofit project were determined based on the simulation results. This part of the work is only summarized in the dissertation but not prepared as a journal paper yet.

Chapter 2. Estimating Time of Concentration for Overland Flow on Pervious and Impervious Surfaces

The particle tracking method (PTM) module was added into the open-source Full Shallow-Water equations for Overland Flow in two-dimension (FullSWOF_2D) program, which has coupled rainfall-runoff and infiltration modules, to determine the time of concentration (T_c) for impervious (T_{ci}) and pervious (T_{cp}) surfaces. The updated program FullSWOF-PTM was tested using observed rainfall events with Nash-Sutcliffe efficiencies ranging 0.60 to 0.95 (average of 0.75) for simulated runoff hydrographs. More than 400 impervious modeling cases with different surface slope (S_0), roughness coefficient (n), length (L), and rainfall intensity (i) combinations were developed and simulated to obtain the T_{ci} for developing the regression equation of T_{ci} as a function of the four input parameters. More than 700 pervious modeling cases with different combinations of S_0, n, L, i, and infiltration parameters including the saturated hydraulic conductivity, suction head, and moisture deficit were simulated to estimate the T_{cp} based on the travel time of 85% particles arriving at the outlet and the ponding time. The regression equation of T_{cp} was developed as the sum of T_{ci} and additional travel time as a function of infiltration parameters and i. The T_{cp} equation can be applied to wide ranges of input parameters in comparison to Akan's equation.

2.1 Introduction

Mulvany (1851) first put forward the concept time of concentration (T_c), and Kuichling (1889) defined T_c as the time needed for the runoff from the most remote part of a catchment to travel to the outlet during the rainfall-runoff process. It is widely used to

design the highway and urban stormwater drainage facilities (Brown et al., 2009) using T_c as design rainfall duration (Guo, 1998). There are dozens of studies where researchers developed and tested/compared T_c equations (Kibler, 1982; McCuen et al., 1984). They obtained the T_c estimation using hydrograph analysis for laboratory plots/watersheds (Izzard, 1946; Muzik, 1974; Wong, 2005), theoretical derivation based on kinematic wave theory (Akan, 1986; Guo, 1998; Wooding, 1965; Woolhiser and Liggett, 1967), and distributed physically-based numerical simulation programs utilizing topographic elevation and geometric data (Hromadka II et al., 1987; Niri et al., 2012; Olivera and Maidment, 1999; Su and Fang, 2003). Izzard (1946) developed a method to calculate the runoff hydrography and the time necessary substantially to reach an equilibrium of flow resulting from given rainfall intensity, roughness, slope, and the length of the overland flow plan based on the laboratory experiments. Compared to laboratory analysis and theory deduction, the distributed and physically based numerical models solving the shallow-water equations (SWEs) are more and more widely used in overland flow simulation for its better performance dealing with mixed subcritical and supercritical flow compared to kinematic wave and diffusive wave approach or other approximation (Gourbesville et al., 2014; Teng et al., 2017). Su and Fang (2003) established a two-dimensional numerical model based on shallow-water equations to estimate traveling time for different rainfall intensity, roughness, length, and slope modeling cases and developed the traveling time estimation equation for relatively steep and very flat watersheds. Recently, more and more researchers moved their focus to the overland flow of pervious surfaces (Akan, 1985; Deng et al., 2005; García Serrana et al., 2017; Hamouda and Lahbassi, 2012). Hjelmfelt (1978) analyzed the infiltration influence on the overland flow by combining the storage-depletion

model of the U.S. Soil Conservation Service with the kinematic wave equations and find the variation of infiltration rate during a storm has a significant effect on the time of concentration and the shape of the runoff hydrograph. In Guo's study (1998), the Wooding's solution was expanded to overland flow on pervious surfaces by coupling the kinematic wave equations with Horton infiltration model. Only Akan developed a time of concentration calculation chart (Akan, 1986) and a formula (Akan, 1989) using the Manning's friction law on rectangular pervious plots under constant-intensity rainfall based on the kinematic wave equations and Green-Ampt (GA) infiltration model. The time of concentration in Akan's study is measured from the beginning of the rainfall event, which means the ponding time (t_p) and runoff travel time were lumped together in the formula. The chart and formula are mainly appropriate for the cases that the Manning's friction law is acceptable and limited ranges of rainfall and soil infiltration parameters. Further work is still needed, e.g., to expand the formula to other flow resistance laws and wide ranges of rainfall and soil infiltration parameters.

Conceptually, the time of concentration is when the entire catchment becomes contributory to the runoff at the outlet, but there are various methods that have been developed/used to estimate T_c. T_c for impervious areas (T_{ci}) was typically estimated from hydrograph analysis, e.g., T_{ci} as lapse time from the beginning of rainfall event to the outlet flow reaching 98% of the peak discharge, which is called T_{c_q98} hereafter, since the runoff starts immediately after the rainfall, and T_c and the runoff equilibrium time are basically the same for impervious surfaces. Above method does not work for determining the time of concentration on pervious surfaces (T_{cp}) since the runoff does not start before the ponding time (t_p) and then discharge increases asymptotically to peak or equilibrium

discharge under constant rainfall intensity even after a long period of simulation. Guo (1998) suggested evaluating T_{cp} of a small catchment by velocity-based methods rather than those empirical formulas developed for and calibrated by the observed hydrographs. The particle tracking method (PTM) is popular for generating path lines and travel time information since it directly utilizes the simulated velocity field results (Bensabat et al., 2000; Cheng et al., 1996; Schafer‐Perini and Wilson, 1991; Suk and Yeh, 2010). KC and Fang (2015) developed a quasi-two-dimensional (2D) diffusion wave model (DWM) coupled with particle tracking to determine the time parameters including the travel time for 85%, 95%, 100% of particles to arrive at the outlet (T_{r_p85}, T_{r_p95}, T_{r_p100}) of overland flow on impervious surfaces. These travel times have significant linear correlations with each other, and a significant agreement between the T_{r_p85} and T_{c_q98} was found.

To understand and estimate T_{cp} for pervious surfaces is particularly important and useful to the smart stormwater management using the lower impact development (LID) and green infrastructures (GI) that promote the infiltration (García Serrana et al., 2017). Therefore, the goal of this study is to develop a T_{cp} equation for pervious surfaces that can be applied to wide ranges of rainfall, watershed and soil parameters. First, the particle tracking method (PTM) module was added into the open-source Full Shallow-Water equations for Overland Flow in two-dimension (FullSWOF_2D, version 1.07) (Delestre et al., 2014) program for determining T_{cp} for pervious surfaces. The FullSWOF_2D program has already coupled the rainfall-runoff modules with the infiltration module (KC and Fang, 2015) for possibly exploring T_{cp} after adding PTM module (called FullSWOF-PTM). Total 750 pervious modeling cases that are combinations of diverse values of rainfall intensity i (m/s or mm/hr); watershed slope S_0, Manning's roughness coefficient n, length L (m);

hydraulic conductivity K (m/s), suction head φ (m), and moisture deficit $\Delta\theta$ of pervious surfaces were generated considering different types of soil groups. Travel time for 85% of particles arriving at the outlet from the beginning of rainfall, which is determined using FullSWOF-PTM and called T_{r_p85} hereafter, was used directly to evaluate T_{ci} for impervious surfaces, and the T_{r_p85} subtracting the ponding time t_p was used to evaluate T_{cp} for pervious surfaces, which is consistent with Guo's (1998) study but different from Akan's equation (Hjelmfelt, 1978). The multiple linear regression (MLR) method was used to derive the T_{cp} equation as a function of input parameters.

2.2 Materials and Methods

2.2.1 Shallow-Water Equations (SWEs) and FullSWOF_2D

As a Saint-Venant system (Barré de Saint-Venant, 1871), the simplified SWEs model is widely used to simulate the incompressible Navier-Stokes flow occurring in rivers, channels, ocean, and land surfaces (Zhang and Cundy, 1989). It is derived with two assumptions, one is the fluid velocity is constant along the vertical (z) direction for that the water depth is small with respect to the horizontal (x, y) dimensions; another is the pressure of the fluid is hydrostatic ($\frac{\partial p}{\partial z} = -g$) which means the pressure field could be calculated with simple integration along the vertical (z) direction (Audusse et al., 2004; Delestre et al., 2014). The conservative form of the 2D SWEs including the continuity equation and two momentum equations for x and y directions are stated as the following equations.

$$\frac{\partial h}{\partial t} + \frac{\partial hu}{\partial x} + \frac{\partial hv}{\partial y} = R - I \quad (2.1)$$

$$\frac{\partial hu}{\partial t} + \frac{\partial}{\partial x}\left(hu^2 + \frac{gh^2}{2}\right) + \frac{\partial}{\partial y}(huv) = gh\left(\frac{\partial z}{\partial x} - S_{fx}\right) \quad (2.2)$$

$$\frac{\partial hv}{\partial t} + \frac{\partial}{\partial x}(huv) + \frac{\partial}{\partial y}\left(hv^2 + \frac{gh^2}{2}\right) = gh\left(\frac{\partial z}{\partial y} - S_{fy}\right) \quad (2.3)$$

where R (m/s) is the rainfall intensity; I (m/s) is the infiltration rate; h (m) is the cell water height; z (m) is the cell topography elevation; u (m/s) and v (m/s) are the cell depth-averaged velocities in x and y directions, respectively; S_{fx} and S_{fy} are the cell friction slopes in x and y directions, respectively; g (m/s^2) is gravity acceleration; t (s) is time.

The FullSWOF_2D program fully solves SWEs on a structured mesh in two space dimensions using the finite volume method (FVM) which ensures mass conservation compared to finite difference method (FDM) (Unterweger et al., 2015). A well-balanced scheme was adapted to guarantee the positivity of water height and the preservation of steady states for specific hydrological features such as during wet-dry transitions and tiny water depth (Cordier et al., 2013; Delestre et al., 2014). Different boundary conditions, friction laws, and numerical schemes were developed which make the program a very powerful overland flow simulation software. The parallelization strategies of FullSWOF_2D were also examined to improve its simulation efficiency deal with large-scale cases (Cordier et al., 2013). A modified bi-layer (crust- and soil-layer) Green-Ampt (GA) infiltration model (Esteves et al., 2000) to calculate I for equation (2.1) was coupled in the FullSWOF_2D (Unterweger et al., 2015) which enables the program to simulate overland flow on impervious and pervious surfaces.

FullSWOF_2D has five boundary condition choices including the imposed discharge and water height case, wall condition, Neumann boundary (open boundary) condition, periodic variations of discharge and water height, and imposed discharge condition. It has three options of friction formulas including the Manning's equation, Darcy-Weisbach equation, and the laminar law, as well as the no friction setting. The simulation domain could be set nonuniformly by defining the friction value of every computational cell with an input file. The Rusanov flux, Harten-Lax-Van Leer (HLL) flux, Harten-Lax-Van Leer with Contact surface (HLLC) flux, HLL2, and HLLC2 (Delestre et al., 2014) methods are provided to calculate every time level flux between computational cells. Three linear reconstruction methods include the MUSCL, ENO, and modified ENO, as well as three slope limiters, include the classical Minmod slope limiter, Van Albada limiter, and Van Leer's limiter are used in the reconstruction part of the 2^{nd} order numerical scheme. The details about the numerical flux, reconstruction methods, and the limiters could be found in Bouchut's (2004) book.

The FullSWOF_2D has been validated using several analytical solutions and benchmarks of the steady-state solutions and the transitory solutions. The steady-state solutions validated by FullSWOF_2D include the emerged bump at rest and Mac Donald test cases with different settings. The transitory solutions include the dam break on a dry domain and Thacker test case with a planar surface in paraboloid (Delestre et al., 2013). It is also widely used in the river flood simulation in a complex environment based on high-resolution topographic data (Abily et al., 2016b) and spatial global sensitivity analysis of high resolution classified topographic data in 2D urban flood modeling (Abily et al., 2016a).

2.2.2 Particle Tracking Method (PTM) and FullSWOF-PTM

The PTM is a powerful method to study the characteristics of complex flow velocity fields during steady and transient-state using simulated velocities from flow governing equations, e.g., equations (2.1), (2.2), and (2.3) for shallow overland flow. It is widely used in different research areas especially the groundwater flow and pollutant transport study (Cordes and Kinzelbach, 1992). Most of the commonly used PTMs provide satisfactory results for steady-state analysis (Pollock, 1994). PTMs could also be used for transient analysis under the assumption that the velocity field does not significantly change during the simulation duration. In Cheng's (1996) study, a PTM was developed based on the Lagrangian-Eulerian finite element method which could reduce the numerical errors considerably and enable the PTM to trace fictitious particles in a complex flow field. It is suggested that the PTM could be extended to transient simulations by tracking velocity calculated with the velocity field of previous time level and current time level (stepwise approximation) when the finite element method (FEM) is used to solve the transport equations. Bensabat et al. (2000) and Lu (1994) developed a linear temporal interpolation scheme instead of a stepwise temporal approximation in order to count for the changes in velocity during a time step in complex unsteady flow while it is only suited to the FDM rather than FEM or FVM. The travel time and the path lines could be generated using PTM directly incorporated with the overland flow simulation velocity field results.

In the previous study (KC and Fang, 2015), the PTM using simulated velocities from DWM was developed to determine the travel time of different percentage particles arrival at the outlet. The travel time of each particle in the simulation domain is computed using the PTM module that uses flow velocity fields simulated by the quasi-two-dimensional

DWM at every time level. Over each time step, the particle travel distance is determined by the product of the appropriate tracking velocity (interpolated by linear spatial method) and time step interval. In this study, a PTM module was incorporated with FullSWOF_2D using simulated velocity field at each time step, and the updated program becomes FullSWOF-PTM. A fourth-order Runge-Kutta (RK4) spatial interpolation scheme rather than a linear spatial interpolation scheme (Pollock, 1994) was adapted to get the particle velocity at each time step at different locations of the simulation domain. The temporal change of all particles was calculated and updated using the simulated particle velocity and the time interval at every time step.

The following algorithm is implemented in the PTM code of FullSWOF-PTM at each time step. 1) The particle location is checked to determine whether it is within the simulation domain. If the particle arrives at the outlet cell, it is ignored, and the tracking process moves on to the next particle. 2) The computational cell that the particle locates in and the adjacent cell for each particle is determined based on the particle location. 3) The particle velocities in *x*- and *y*-directions are spatially interpolated using an RK4 scheme based on the simulated *x* and *y* velocities of the cell that the particle locates in and adjacent computational cells at the time step. 4) The new locations of all particles are calculated and updated using the previous location, current particle velocities, and time step interval. 5) The particle with the new location is checked again to determine whether it stays in the simulation domain or arrives at the outlet cell and gets out of the domain. 6) The percentage of particles remained in the simulation domain is counted. The particle evolution information of each time step including the total number and percentage of particles remained in the simulation domain is outputted during the whole simulation period with

FullSWOF-PTM. A user interface for FullSWOF-PTM was developed using Matlab r2017a (2017) to run all impervious and pervious cases in batches.

2.2.3 Modeling Cases

Three kinds of modeling cases were developed and simulated in this study: 11 testing cases, 446 impervious cases, and 750 pervious cases; and details are described below.

2. 2.3.1 FullSWOF-PTM Testing Cases

FullSWOF-PTM was validated using 11 rainfall events as testing cases to demonstrate that it can be used for accurate overland flow simulations. In Esteves's study (2000), a 2D overland flow model solving SWEs based on an explicit FDM and coupled with GA infiltration module was developed and calibrated/validated with the observed data on a natural hillslope plot. These observed rainfall and runoff data from 11 events plus the plot topography and soil infiltration data were obtained from Dr. Esteves and first used to test the FullSWOF-PTM model. The plot is 14.25 m long and 5 m wide that is bordered by 150 mm wide cement blocks drove about 50 mm into the ground (Peugeot et al., 1997). The cell size used in the simulation is 0.25 m based on a detailed topographic survey. The Darcy-Weisbach friction law (friction coefficient = 0.25) is used in the simulation. The plot is crusted, almost without vegetation. The infiltration model parameters including the saturated hydraulic conductivity (K, 0.0162 mm/hr for crust and 77.4 mm/hr for soil below), saturated water content (θ_s, 0.245 for crust and 0.296 for soil), and suction head (φ) of crust layer and soil, as well as the crust layer thickness (0.005 m) were all the same as the calibrated parameters used in Esteves's study (2000).

The plot slope in *x*- and *y*-directions are 0.0640 ± 0.0292 (from the right to left boundary) and 0.0196 ± 0.0155 (from top to bottom boundary), respectively. The right, top, and bottom boundaries of the study plot were all set as wall condition, and the left (downstream) boundary was as Neumann (open) condition based on the field situation. The HLLC flux choice in FullSWOF-PTM was selected from the 1st order numerical scheme to calculate the new time level flux of each computational cells in the simulation. The Courant-Friedrichs-Lewy (CFL) condition (CFL = 0.45) was used to guarantee the numerical stability and calculate the time step interval for the simulation.

The rainfall data was measured with an electronic tipping-bucket recording rain gauge (each tip corresponding to 0.5 mm of rainfall). The discharge at the plot outlet was measured through a triangular 20° V-notch weir every 5-second interval. The initial water content of the soil at the beginning of the rainfall was measured using a neutron-probe access tube located in the center of the plot (Esteves et al., 2000). The moisture deficit $\Delta\theta$ was calculated as the difference of saturation water content (θ_s = porosity) and initial moisture content (θ_i). Green-Ampt method (Rawls et al., 1983) assumes a sharp wetting front from the wet soil with θ_s to a dryer soil with θ_i.

The goodness of fit for the simulated hydrograph is evaluated using the Nash-Sutcliffe Efficiency (NSE) coefficient (Nash and Sutcliffe, 1970).

$$NSE = 1 - \frac{\sum_{j=1}^{m}(Q_{oj} - Q_{sj})^2}{\sum_{j=1}^{m}(Q_{oj} - \bar{Q})^2} \tag{2.4}$$

where Q_{oj} (m^3/s) is the j^{th} observed runoff rate, Q_{sj} (m^3/s) is the corresponding simulated runoff rate, $\bar{Q}$ (m^3/s) is the mean observed runoff rate, and m [-] is the total number of observed runoff rates. The NSE values for 11 rainfall events were calculated and compared

with those reported by Esteves's program to evaluate the FullSWOF-PTM. The FullSWOF-PTM's performance was further evaluated by comparing simulated and observed runoff depth and peak discharge at the outlet.

2. 2.3.2 Impervious modeling cases

Using FullSWOF-PTM to model the overland flow on impervious surfaces has two purposes: 1) validating FullSWOF-PTM since calculated T_{ci} can be compared with many previous studies or established equations, and 2) T_{ci} will be used to develop T_{cp} equation. Total 446 impervious modeling cases with different combinations of S_0, n, L, and i were simulated. In this study, the cell size in x- and y-directions and simulation domain width used for impervious and pervious modeling cases are 0.25 m and 1 m (4 cells in the y-direction, no cross slope), respectively. The Manning's friction formula was selected among three friction formulas of FullSWOF-PTM. Figure 2.1 shows the model-parameter value distributions of the 446 cases, which also prove the parameter values are representative and set in the commonly used ranges (Brown et al., 2009).

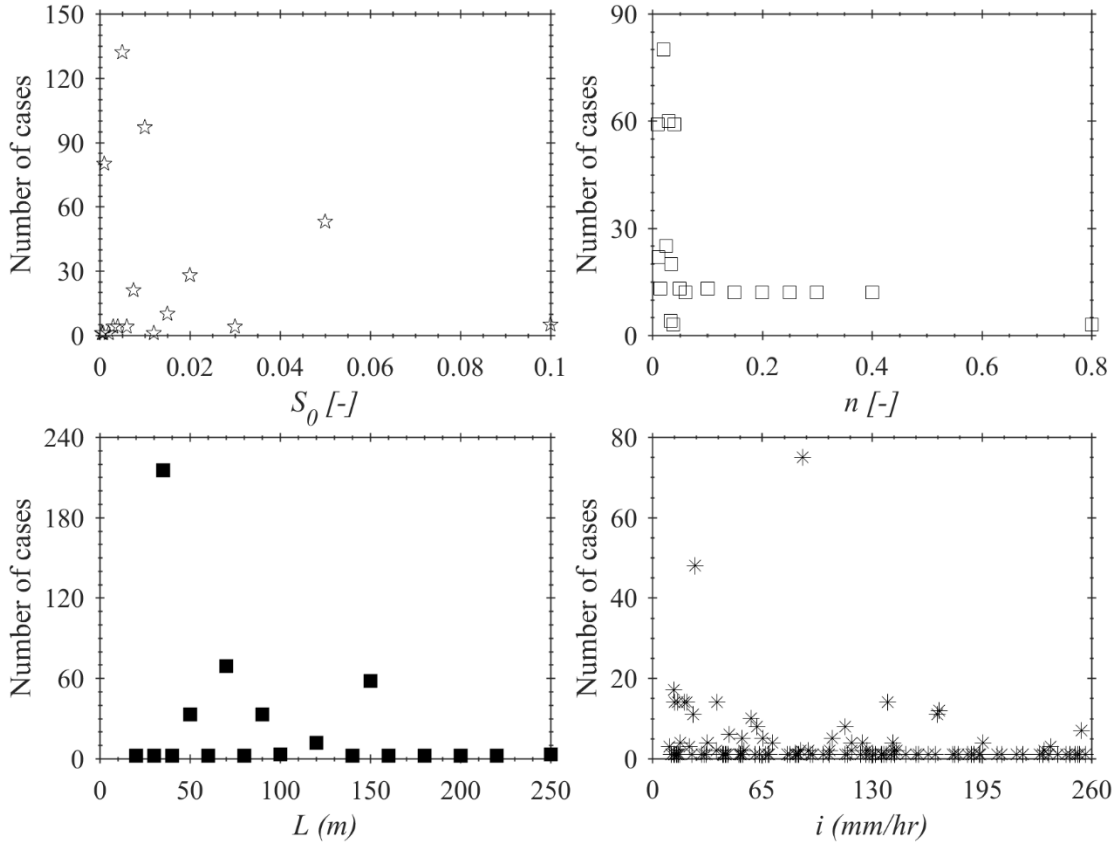

Figure 2.1. Distributions of the values of four model input parameters used for the 446 impervious modeling cases.

For 446 impervious modeling cases, the plot longitudinal slope S_0 ranges from 0.0005 to 0.1 with the average slope of 0.0133 and standard deviation of 0.0175, and 86% of the cases have $S_0 \leq 2\%$. The Manning's roughness n ranges from 0.01 to 0.8 with 86% of n values less than 0.1. The plot length L ranges from 20 m to 250 m; the rainfall intensity i ranges from 10.2 mm/hr to 256.5 mm/hr with the average value and standard deviation of 80.8 mm/hr and 64.0 mm/hr, respectively. There are 384 modeling cases with $S_0 \leq 0.02$, 395 cases with $n \leq 0.15$, 435 cases with $L \leq 150$ m, and 381 cases with $i \leq 150$ mm/hr.

The topography file, rainfall file, particle initialization file, and model parameter file are required for FullSWOF-PTM in the impervious modeling cases, which were created

using user-developed MATLAB code. The 2nd order numerical scheme in FullSWOF-PTM including the numerical flux methods (5 choices), linear reconstruction settings (3 choices), and slope limiters (3 choices) were tested using one impervious modeling case (S_0 = 0.05, L = 35 m, n = 0.01, and i = 12.7 mm/hr), which aims to identify the best numerical scheme among the 45 combinations. After performing the tests, all other impervious modeling cases were run in batches with MATLAB code using the tested best numerical scheme combination.

2. 2.3.3 Pervious Modeling Cases

The GA infiltration parameters for different soil types of pervious surfaces were adapted from the research conducted by Rawls et al. (1983). The soil was categorized in this study into three groups: sand (K ranging 25.4 to 127.0 mm/hr), loam (K ranging 2.54 to 12.7 mm/hr), and clay (K ranging 0.23 to 1.52 mm/hr) groups depending upon the saturated hydraulic conductivity. There were 204, 350, and 196 modeling cases for sand, loam, and clay soil, respectively. Total 750 modeling cases were developed and simulated while one T_{cp} equation was derived from results of all pervious surfaces rather than developing three equations for different soil groups. The crust thickness of the pervious plots is set equal to zero because this study focused on the influence of soil property on the T_{cp} for pervious surfaces. The soil infiltration parameters: saturated hydraulic conductivity K, suction head φ, and moisture deficit $\Delta\theta$ used for 750 modeling cases are shown in Figure 2.2. A dimensionless saturated hydraulic conductivity K' $(=K/i)$, which was used by Akan in the derivation of the T_{cp} equation for pervious surfaces (Akan, 1989), was calculated and ranged from 0.001 to 0.97 for 750 modeling cases (Figure 2). Since K' is less than 1, it means $K < i$ and all previous modeling cases should produce runoff eventually when the

rainfall duration is long enough. Equation (2.5) developed by Akan (1989) is limited to $K' \leq 0.4$, i.e., $i \geq 2.5\,K$, which means Akan's equation does not apply to relatively small rainfall intensity in comparison to K, but in reality i can be larger or even smaller than K. When $i \leq K$, it is not applicable to determine the T_{cp} for pervious surfaces since there is no surface runoff as all rainfall is infiltrated.

$$T_{cp_A} = \left(\frac{Ln}{\sqrt{S_0}}\right)^{0.60} \frac{1}{(i-K)^{0.40}} + 3.1\frac{K^{1.33}\varphi\Delta\theta}{i^{2.33}} \qquad \text{(For } K' \leq 0.4\text{)} \qquad (2.5)$$

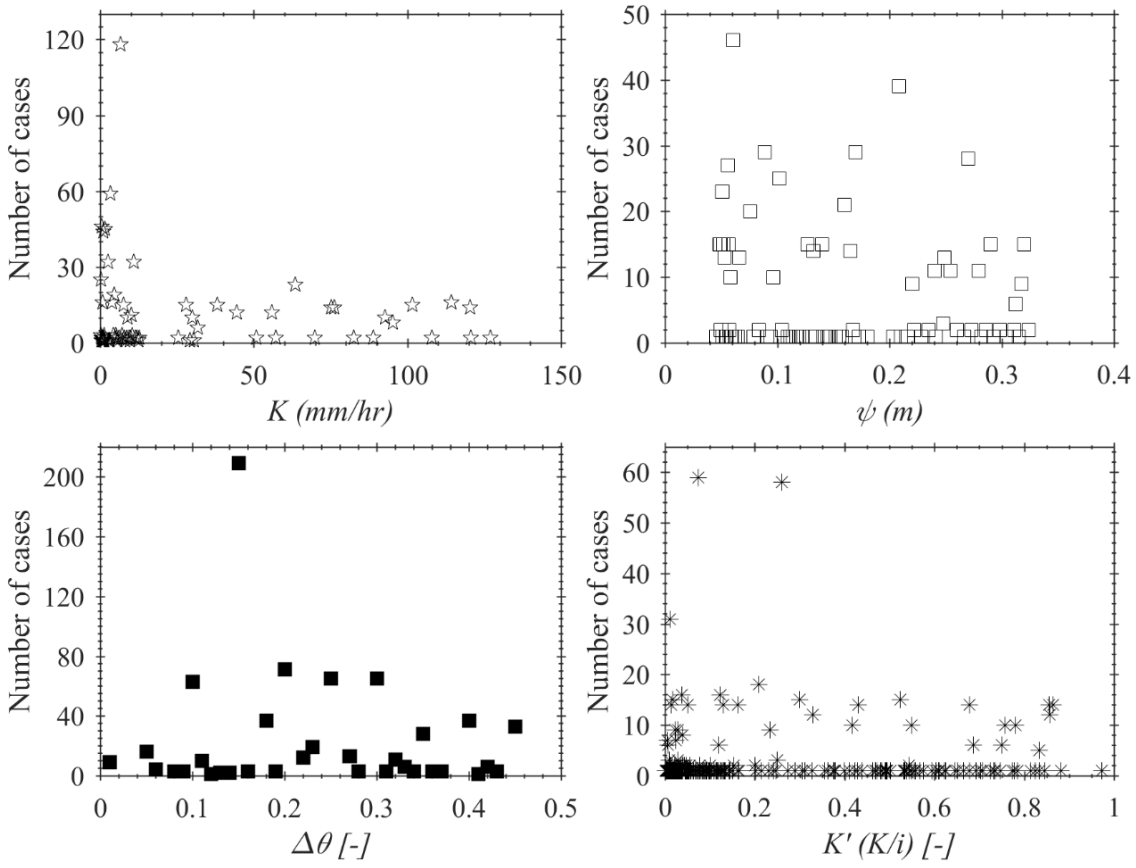

Figure 2.2. Distributions of the values of three soil infiltration parameters and calculated $K' = K/i$ used for 750 pervious modeling cases.

The representative values of infiltration parameters of three soil groups were selected from literature (Rawls et al., 1983) for 750 modeling cases. The saturation hydraulic conductivity ranges from 0.23 mm/hr to 127 mm/hr. The soil dry suction head ranges from 0.0457 m to 0.3238 m. The moisture deficit ranges from 0.01 to 0.45.

2.3 Results and Discussions

2.3.1 FullSWOF-PTM Testing Results

The simulated discharges from FullSWOF-PTM were divided by the drainage area and compared to the observed runoff data (mm/hr) for all 11 testing events. The comparison of observed and simulated discharge hydrographs on August 24 and September 4, 1994, are shown in Figure 2.3 as sample results, and the hydrographs closely follow rainfall variations. It shows that the FullSWOF-PTM simulation results have strong consistency with the observed data during the whole rainfall period.

For 11 rainfall events, the initial moisture content θ_i ranged from 0.048 to 0.106. Since the soil porosity of the field is 0.296, the moisture deficit $\Delta\theta$ ranged from 0.190 to 0.248. The discharge NSE values of FullSWOF-PTM and Esteves's programs range from 0.64 to 0.95 (average $\pm$ standard deviation as 0.75 ± 0.11) and from 0.46 to 0.93 (0.79 ± 0.15), respectively; and this indicates FullSWOF-PTM performed as well as Esteves's program in simulating overland flows.

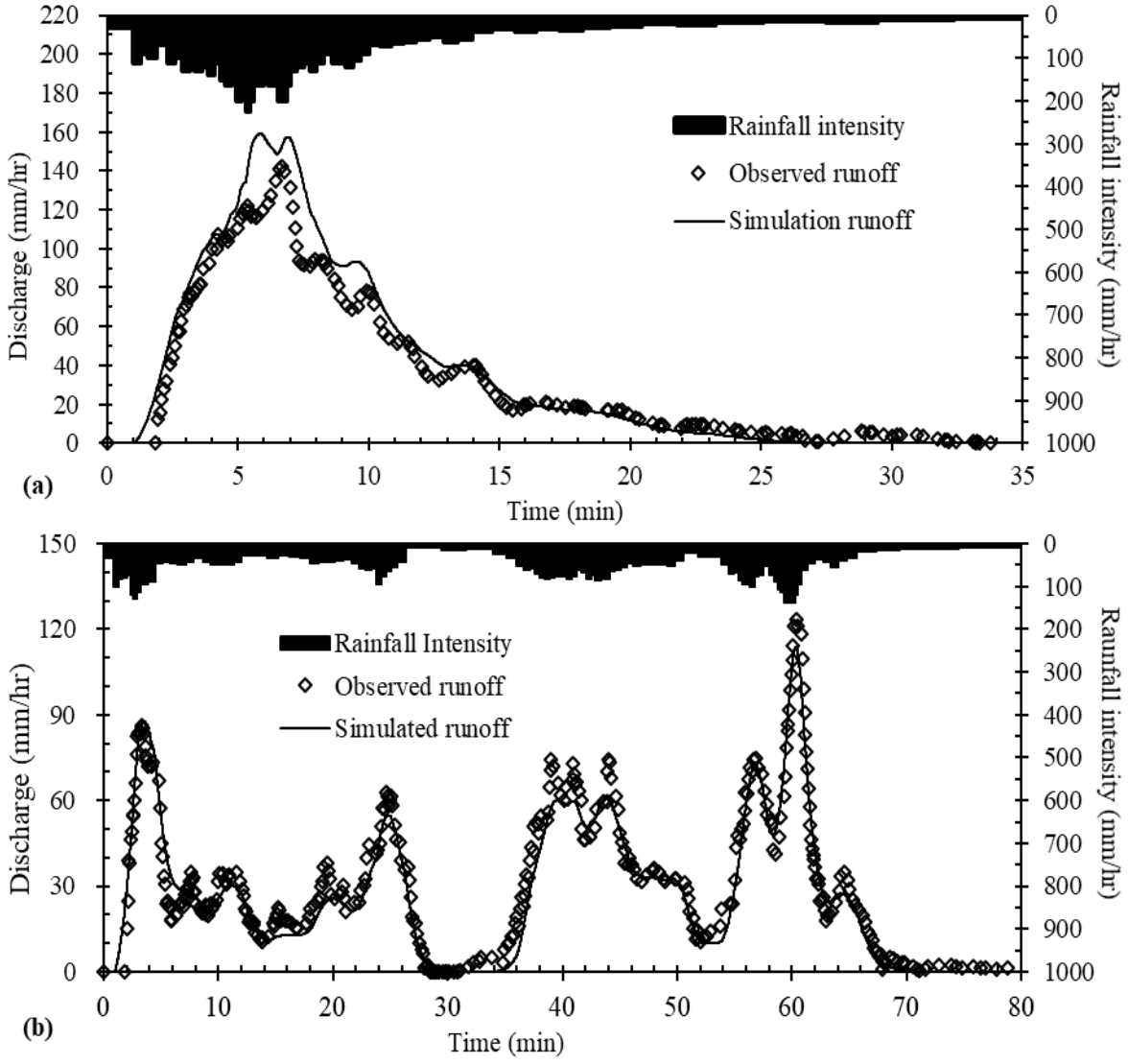

Figure 2.3. Comparison of simulated and observed hydrographs of two events on (**a**) August 24 and (**b**) September 4, 1994.

2.3.2 Time of Concentration (T_{ci}) of Impervious Surfaces

In previous studies (Izzard, 1946; KC et al., 2014; Kuichling, 1889; Su and Fang, 2003; Wong, 2005), T_c was evaluated as the time when discharge at the outlet reaches a specific percentage of the equilibrium discharge, e.g., 90%, 95% or 98% of peak discharge (Q_p). However, it is difficult to evaluate T_c for pervious surfaces using the fixed percent Q_p

because there is almost no equilibrium discharge for pervious surfaces. In this study, the travel time for 85% particles arriving at the drainage outlet (T_{r_p85}) was used to evaluate the T_c for both impervious and pervious surfaces based on the previous PTM studies (KC and Fang, 2015).

Figure 2.4 shows simulated outlet discharge and the in-domain particle percentage versus time under eight Manning's roughness coefficients but the same plot slope, length, and rainfall intensity. The 2nd order numerical scheme combinations: HLL2 for the numerical flux, ENO for the linear reconstruction, and Vanleer for the slope limiter (Bouchut, 2004) were used for the simulation because the simulated Q_p was the same as Q_p calculated by the rational method and the run time for the program is the shortest. Simulated discharges verses time by FullSWOF-PTM give S-hydrographs (Viessman and Lewis, 2003) in Figure 2.4 under the constant rainfall intensities over a long period. The outlet discharge increases and the in-domain particle percentage decreases as the constant rainfall continues, and finally both reach to the equilibriums. Based on the rational equation, the peak discharge (Q_{pr}) for all eight runs should be the same and equal to 0.864 L/s, which is the same as FullSWOF-PTM simulated Q_p (Figure 2.4).

On Figure 2.4, T_{c_q98} is the T_c defined or calculated as the travel time when the runoff reaches to the 98% percent of the equilibrium discharge Q_{pr}, and T_{r_p85} is the travel time when the in-domain particle percentage is 15%. Both T_{c_q98} and T_{r_p85} increase with the increase of the roughness (Figure 2.4) since the flow velocity is smaller with higher roughness. Figure 2.4 indicates that T_{c_q98} is somewhat smaller than T_{r_p85} for each case, which is the same as the conclusion of the previous research (KC and Fang, 2015).

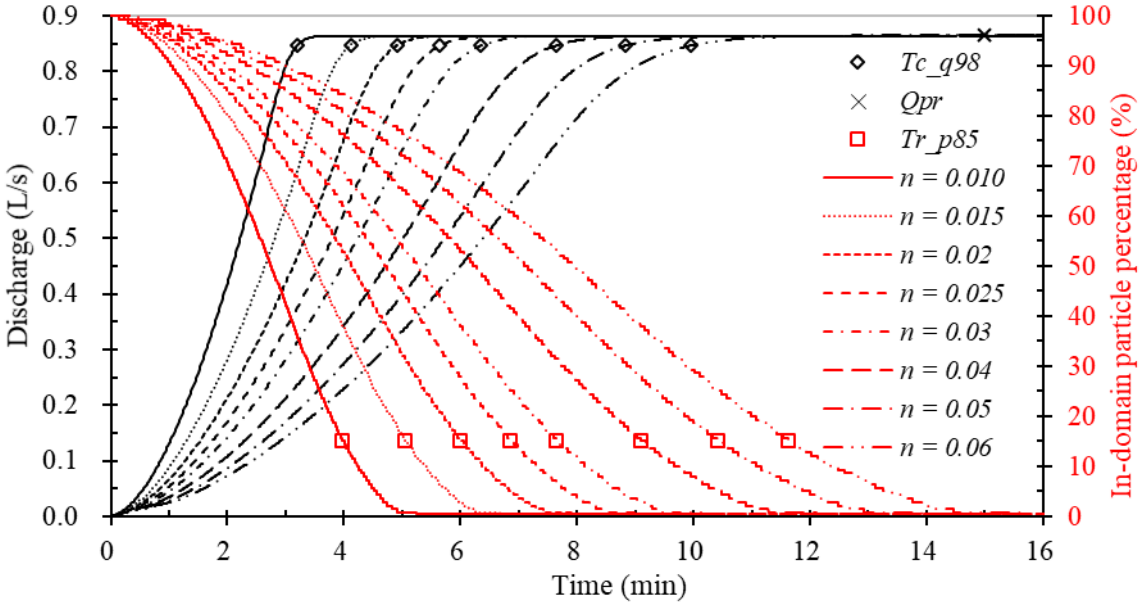

Figure 2.4. Simulated outlet discharge and in-domain particle percentage versus time under different roughness (n) coefficients for eight modeling cases with i = 88.9 mm/hr, S_0 = 0.005 and L = 35m of impervious surfaces.

A generalized power relation, Equation (2.6) was chosen to develop the regression equation for T_{ci} as a function of four input/influencing parameters (L, n, S_o, and i). The three influencing parameters L, n, and S_o that describe/characterize the overland flow surface were grouped as a combined parameter ($Ln/\sqrt{S_0}$) because the Manning's equation was used in FullSWOF-PTM as friction formula for the overland flow resistance (Akan, 1989). The T_{r_p85} obtained from FullSWOF-PTM was considered as T_{ci} or T_{ci_p85} (Figure 2.5), and T_{r_p85} values for all 446 impervious modeling cases were used to develop the T_{ci} regression equation.

$$T_{ci} = \left(\frac{Ln}{\sqrt{S_0}}\right)^{k_1} \frac{1}{i^{k_2}} \tag{2.6}$$

The exponents (k_1 and k_2) were estimated using the MLR method after the log-transformation of Equation (2.6), and the resulting regression equations of T_{ci_p85} are:

$$T_{ci} = \left(\frac{nL}{\sqrt{S_0}}\right)^{0.608} \frac{1}{i^{0.422}} \qquad (R^2 = 0.996) \tag{2.7}$$

$$T_{ci} = 9.741 \times \left(\frac{nL}{\sqrt{S_0}}\right)^{0.608} \frac{1}{i^{0.422}} \tag{2.8}$$

where L is in (m), n is in [-], S_0 is in [-], T_{ci} of Equation (2.7) is in seconds and Equation (2.8) in minutes, respectively, when i for Equation (2.7) is in m/s and for Equation (2.8) in mm/hr. FullSWOF-PTM uses i in m/s for all computations (1 m/s = 3,600,000 mm/hr). The 95% confidence intervals for k_1 and k_2 are [0.606, 0.610] and [0.421, 0.423] with p-value < 0.0001, respectively. The average difference between T_{ci} calculated using Equation (2.7) and simulated T_{ci_p85} is 0.11 min with a standard deviation of 1.45 min (Figure 2.5).

Figure 2.5 shows calculated T_{ci} from Equation (2.8) and five other equations (Henderson and Wooding, 1964; Johnstone and Cross, 1949; Kirpich, 1940; Linsley et al., 1958; Morgali and Linsley, 1965) versus simulated T_{ci_p85}. The calculated T_{ci} from all six equations (Table 2.1) linearly correlates well with the simulated T_{ci_p85} as indicated by R^2 > 0.994 and regression equations in Table 2.1. This proves Equation (2.8) developed from T_{ci_p85} predicts well T_c for impervious surfaces and the travel time for 85% particles to arrive at the outlet can be considered as T_{ci} with reasonable accuracy.

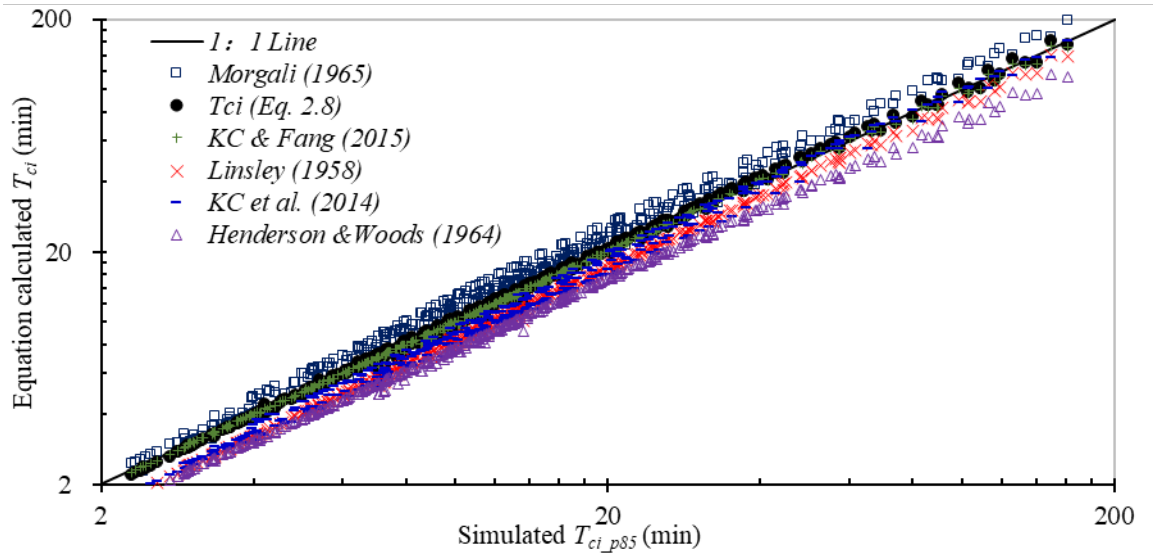

Figure 2.5. T_{ci} calculated from six equations (Table 2.1) versus simulated T_{ci_p85} for 446 modeling cases of impervious surfaces.

The RMSE value of the KC and Fang's equation (2015), also based on the travel time for 85% particles to arrive at the outlet (KC and Fang, 2015), is the smallest (1.38 min, Table 2.1) and the RMSE of equation (2.8) is just slightly larger. In overall, the Henderson & Woods and Linsley equations underestimate T_{ci_p85} while Morgali equation overestimates, and the remaining three equations predict T_{ci} well with lower RMSE for impervious surfaces.

Table 2.1. Six T_{ci} equations and statistical results when comparing with simulated T_{ci_p85} (Figure 2.5).

Source	T_{ci} Formula (min)	R^2	RMSE (min)
T_{ci} (Eq. 2.8)	$T_{ci} = 9.741 \times \frac{\left(\frac{nL}{\sqrt{S_0}}\right)^{0.608}}{i^{0.422}}$	0.996 (1.00×T_{ci_p85}) [1]	1.45
Linsley (1958)	$T_{ci} = \frac{6.82\left(\frac{nL}{\sqrt{S_0}}\right)^{0.633}}{i^{0.398}}$	0.998 (0.87×T_{ci_p85})	4.15
Henderson & Woods (1964)	$T_{ci} = \frac{6.98\left(\frac{nL}{\sqrt{S_0}}\right)^{0.60}}{i^{0.40}}$	0.997 (0.74×T_{ci_p85})	8.04
Morgali (1965)	$T_{ci} = \frac{7.05L^{0.593}n^{0.605}}{i^{0.388}S_0^{0.38}}$	0.995 (1.19×T_{ci_p85})	6.08
KC et al. (2014)	$T_{ci} = 8.67 \times \frac{L^{0.541}n^{0.649}}{i^{0.391}S_0^{0.359}}$	0.994 (0.96×T_{ci_p85})	2.33
KC & Fang (2015)	$T_{ci} = 9.25 \times \frac{L^{0.599}n^{0.609}}{i^{0.399}S_0^{0.303}}$	0.997 (0.98×T_{ci_p85})	1.38

Note: [1] – the fitted equation between each equation-calculated T_{ci} and T_{ci_p85} is given inside brackets after R^2.

2.3.3 Time of Concentration (T_{cp}) of Pervious Surfaces

The responding runoff hydrographs and in-domain particle percentages of eight saturation hydraulic conductivity values for pervious surfaces (S_0 = 0.01, L = 50 m, φ = 0.06 m, $\Delta\theta$ = 0.18) are summarized and compared in Figure 2.6 under constant rainfall

intensity (i = 105.2 mm/hr). Figure 2.6 indicates that the PTM is the only choice to evaluate T_{cp} for pervious surfaces because it is not practical to simulate for a very long period for the runoff to reach acceptable equilibrium. For a pervious surface, the rainfall in the early period will completely infiltrate when the rainfall intensity is smaller than the infiltration capacity (Diskin and Nazimov, 1996) (Figure 2.6). The time before ponding or start of surface runoff is defined as the ponding time, which depends on both the rainfall intensity and infiltration rate. When the Green-Ampt infiltration model is used, the ponding time (t_p) under constant rainfall intensity is calculated using Equation (2.9) (Chow et al., 1988).

$$t_p = \frac{\varphi \Delta\theta K}{i(i-K)} = \frac{\varphi \Delta\theta K'}{i(1-K')} \tag{2.9}$$

For eight modeling cases on Figure 2.6, K ranges from 7.06×10^{-6} to 19.4×10^{-6} m/s (25.4 – 69.8 mm/hr), which belongs to sandy loam or sand soil groups, and the ponding time from Equation (2.9) ranges from 1.96 to 12.2 min that is the same as predicted by FullSWOF-PTM. Equation (2.9) is valid when $i > K$, but if $t \leq t_p$ even when $i > K$, there is still no surface runoff, and then it is not necessary and not meaningful to determine T_{cp} for pervious surfaces. For impervious surfaces, T_{ci} always exists for any non-zero rainfall intensity (Table 2.1).

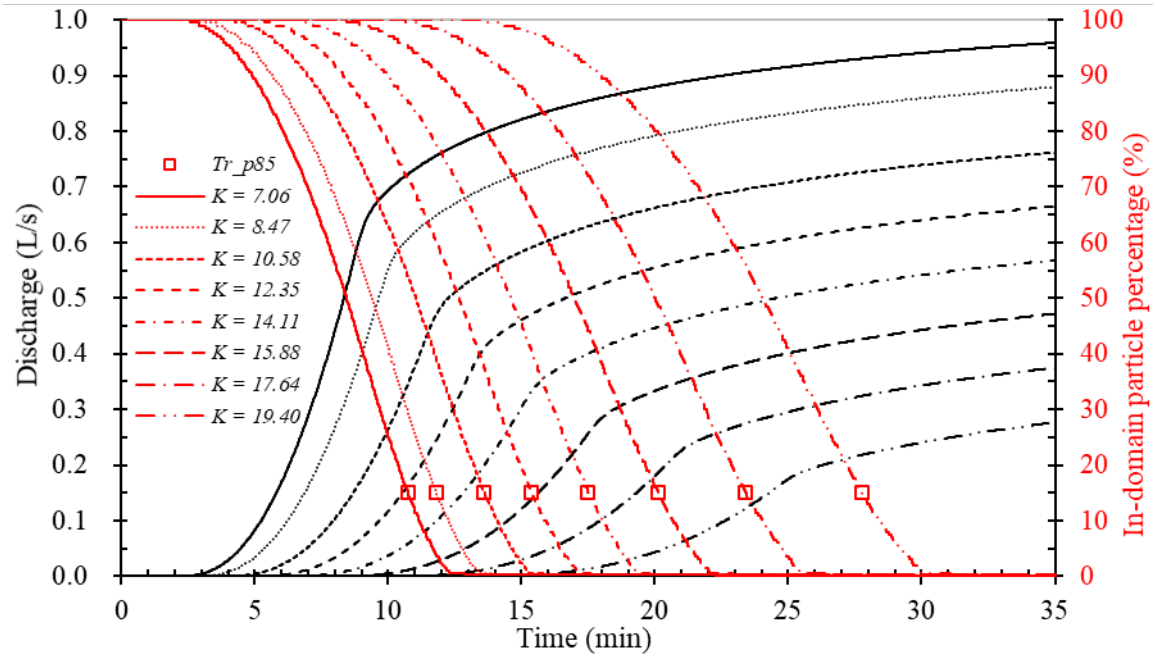

Figure 2.6. Simulated runoff hydrograph and in-domain particle percentage versus time for eight modeling cases of different saturation hydraulic conductivity (K, in 10^{-6} m/s) with S_0 =0.01, i = 105.2 mm/hr, L = 50 m, φ = 0.06 m, $\Delta\theta$ = 0.18 of pervious surfaces.

For pervious surfaces, the outlet discharge decreases with the increase of K (Figure 2.6) because of more infiltration. The outlet discharge and in-domain particle percentage were postponed more and more when K and the soil infiltration capacity increase. The in-domain particle percentage is 100% when $t \leq t_p$. The travel time for 85% particles to arrive at the outlet T_{r_p85} was calculated by FullSWOF-PTM from the beginning of the rainfall event and ranged from 10.7 to 27.8 min (open squares in Figure 2.6) for these eight cases.

Following Akan's study (1989), T_{cp} is considered as the sum of the time of concentration of an equivalent impervious surface (T_{ci}) using (i – K) as effective rainfall and additional travel time due to infiltration (T_{rs}) related to the soil infiltration properties. A generalized power relation in Equation (2.10) was used to develop a regression equation

for T_{rs} and then for T_{cp} equation of pervious surfaces based on the simulated T_{r_p85} of 750 pervious modeling cases.

$$T_{cp} = T_{r_{p85}} - t_p = T_{ci} + T_{rs} = \left(\frac{Ln}{\sqrt{S_0}}\right)^{0.608} \frac{1}{(i-K)^{0.422}} + c_1 \frac{K^{c_2} \varphi^{c_3} \Delta\theta^{c_4}}{i^{c_5}} \quad (2.10)$$

The exponents (C_1, C_2, C_3, C_4, and C_5) in Equation (2.10) were determined using the MLR regression between $y = T_{r\_p85} - t_p - T_{ci}$ and x = (K, φ, $\Delta\theta$, and i) after log-transformed. The fit results of five exponents were summarized in Table 2.2 and Equation (2.11).

Table 2.2. MLR fitted exponents C_1 to C_5 of Equation (2.10) and corresponding 95% confidence intervals.

Parameter	Value	95% Confidence interval
C_1	2.162	[0.875, 5.340]
C_2	0.535	[0.488, 0.582]
C_3	0.161	[0.030, 0.292]
C_4	0.645	[0.591, 0.699]
C_5	1.213	[1.172, 1.255]

$$T_{cp} = \left(\frac{Ln}{\sqrt{S_0}}\right)^{0.608} \frac{1}{(i-K)^{0.422}} + 2.162 \frac{K^{0.535} \varphi^{0.161} \Delta\theta^{0.645}}{i^{1.213}} \quad (2.11)$$

Where T_{cp} is in second when L is in m; n, S_0, and $\Delta\theta$ are dimensionless, i and K are in m/s, and φ in m. The regression equation for T_{cp} has a p-value < 0.0001, and the residuals between calculated T_{cp} from Equation (2.11) and $T_{r\_p85} - t_p$ range from -15.4 to 53.3 min with average residual of 1.12 min (standard deviation 6.13 min). One can see that Equation (2.11) developed from this study can be used to determine the T_c of overland flows for both impervious (setting K = 0) and pervious surfaces.

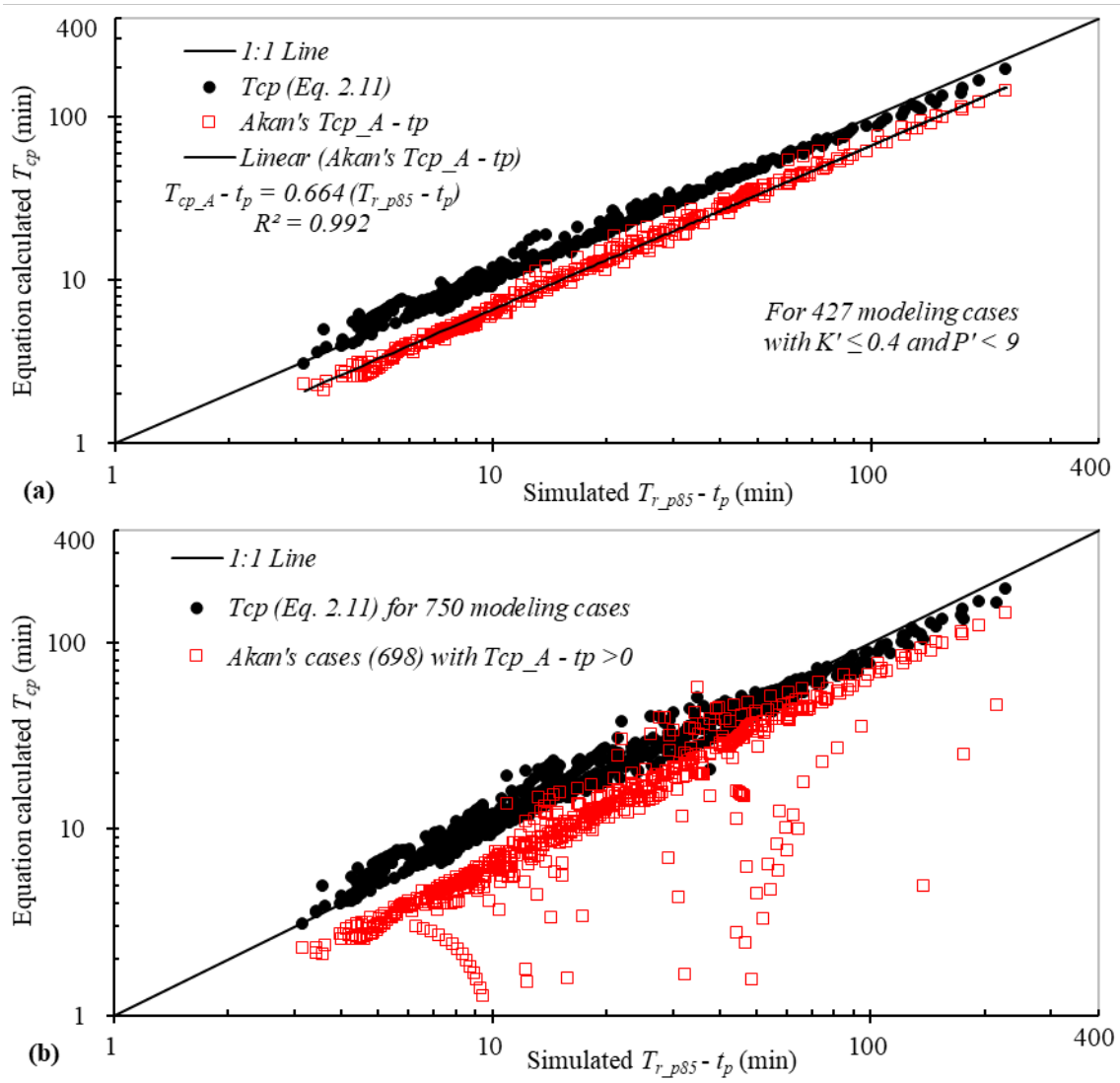

Figure 2.7. Comparison of equation calculated T_{cp} and T_{r_p85} - t_p: (**a**) 427 modeling cases with $K' \leq 0.4$ and $P' < 9$ cases, (**b**) 750 modeling cases for Equation ((2.11) and 698 modeling cases with Akan's $T_{cp} - t_p > 0$.

The comparison of Equation (2.11) and Akan's Equation (2.5) was shown in Figure 2.7: (a) for $K' \leq 0.4$ (427 modeling cases) and (b) for all 750 modeling cases since Akan (Akan, 1989) developed Equation (2.5) for $K' \leq 0.4$. Akan's time of concentration for pervious surfaces (T_{cp_A}) is counted from the beginning of rainfall event and includes the period before the ponding time; therefore, T_{cp} from Equation (2.11) and $T_{cp\_A} - t_p$ are plotted

against $T_{r\_p85} - t_p$ on Figure 8. Akan's $T_{cp\_A} - t_p$ is linearly correlated well with $T_{r\_p85} - t_p$ when the overall R^2 is 0.992, but underestimated since $T_{cp\_A} - t_p = 0.664\ (T_{r\_p85} - t_p)$ (Figure 2.7) and RMSE is 13.7 min. The RMSEs of Equation (2.11) is 4.8 min, and the overall R^2 is 0.993.

Figure 2.7(b) shows the comparison of calculated T_{cp} from Equation (2.11) for 750 modeling cases and $T_{cp\_A} - t_p$ for 698 cases with $T_{cp\_A} - t_p > 0$ against T_{r_p85} - t_p. When Akan's Equation (2.5) is applied to 323 modeling cases with $K' > 0.4$, there are 52 cases having $T_{cp\_A} - t_p < 0$ or $T_{cp\_A} < t_p$, which were not shown on the log scale plot (Figure 2.7). The R^2 of Equation (2.11) and Akan's $T_{cp\_A} - t_p$ are 0.979 for 750 cases and 0.792 for 698 cases with $T_{cp\_A} - t_p > 0$, respectively. The RMSE of Equation (2.11) and Akan's $T_{cp\_A} - t_p$ are 6.2 min and 18.0 min, respectively. Figure 2.7 and above analysis show Akan's Equation (2.5) should not be applied to beyond its limits: $K' \leq 0.4$ and $P' < 9$, where $P' = \varphi\Delta\theta/iT_{ci}$ and T_{ci} used by Akan in Equation (2.5) is the same as Henderson and Woods' T_{ci} equation (Akan, 1989). Akan introduced P' for solving non-dimensional flow and infiltration equations but did not explain any physical meaning of P' (Akan, 1985; Akan, 1986; Akan, 1989). One can see that iT_{ci} is rainfall depth over T_{ci} of the impervious surface of the same geometry and the ponding time increases with $\varphi\Delta\theta$ indicated by Equation (2.9). Akan (1989) indicated $K' \leq 0.4$ and $P' < 9$ are for most practical applications without providing any reason. For 750 modeling cases studied here, the limits of K' values are [0.001, 0.97] and of P' values are [0.18, 55.27]. Therefore, Equation (2.11) developed form this study can be used to estimate T_{cp} for pervious surfaces with reasonable accuracy and over wide ranges of input parameters, especially for small rainfall intensities in comparison to K.

2.4 Summary and Conclusions

The particle tracking method PTM module was added into the 2D overland flow simulation program based on the open-source program FullSWOF_2D that can be used to estimate the time of concentration for impervious and pervious surfaces. The FullSWOF-PTM program was tested using published rainfall, and runoff data and simulated hydrographs match well with observed data, which proves it can predict the overland flow accurately. Four hundred forty-six impervious modeling cases were developed and simulated to explore T_{ci} of overland flow on impervious surfaces. The travel time of 85% particles to arrive at the drainage outlet (T_{r_p85}) was calculated by FullSWOF-PTM for determining the time of concentration of impervious and pervious surfaces in this study. A regression equation of T_{ci}, Equation (2.7) was derived using the MLR regression method and as a power function of $\frac{Ln}{\sqrt{S_0}}$ and i. The derived impervious surface T_{ci} equation match well with T_{r_p85} and correlates well with T_{ci} from other five published equations, which further proves FullSWOF-PTM can be used to estimate T_{cp} of overland flow on pervious surfaces.

Seven hundred fifty pervious modeling cases were developed and simulated to explore the T_{cp} equation. In this study, T_{cp} is considered as T_{r_p85} of pervious surfaces determined from FullSWOF-PTM minus the ponding time t_p determined using Equation (2.9). It means T_{cp} is not counted from the beginning of the rainfall but the commencing of the runoff. Engineers and designers should calculate t_p first, e.g., using Equation (2.9), before T_{cp} for pervious surface is calculated because it is not meaningful to determine T_{cp} for pervious surfaces when the rainfall duration is less than t_p. A regression equation for T_{cp}, Equation

(2.11) was developed using simulated T_{rp_p85} and calculated t_p from 750 pervious modeling cases. Equation (2.11) includes T_{ci} for an equivalent impervious surface using $(i - K)$ as effective rainfall and additional travel time due to infiltration (T_{rs}) as a function of rainfall intensity and the soil infiltration parameters (K, φ, and $\Delta\theta$). Therefore, Equation (2.11) can be used for both impervious and pervious surfaces. The derived T_{cp} equation has higher R^2 and smaller RMSE compared to Akan's equation as well as wide ranges of input parameters.

Chapter 3. Evaluating Curb Inlet Efficiency for Urban Drainage and Road Bioretention Facilities

An updated two-dimensional flow simulation program, FullSWOF-ZG, which fully (Full) solves shallow water (SW) equations for overland flow (OF) and includes submodules modeling infiltration by zones (Z) and flow interception by grate-inlet (G), was tested with 20 locally depressed curb inlets to validate the inlet efficiency (E_{ci}), and with 80 undepressed curb inlets to validate the inlet lengths (L_T) for 100% interception. Previous curb inlet equations were based on certain theoretical approximations and limited experimental data. In this study, 1000 road-curb inlet modeling cases from the combinations of 10 longitudinal slopes (S_0, 0.1–1%), 10 cross slopes (S_x, 1.5–6%), and 10 upstream inflows (Q_{in}, 6–24 L/s) were established and modeled to determine L_T. The second 1000 modeling cases with the same 10 S_0 and 10 S_x and 10 curb inlet lengths (L_{ci}, 0.15–1.5 m) were established to determine E_{ci}. The L_T and E_{ci} regression equations were developed as a function of input parameters (S_0, S_x, and Q_{in}) and L_{ci}/L_T with the multiple linear regression method, respectively. Newly developed regression equations were applied to 10,000 inlet design cases (10 S_0, 10 S_x, 10 Q_{in}, and 10 L_{ci} combinations) and comprehensively compared with three equations in previous studies. The 100% intercepted gutter flow (Q_{g100}) equations were derived, and over-prediction of Q_{g100} from previous methods was strongly correlated to smaller S_0. Newly developed equations gave more accurate estimations of L_T and E_{ci} over a wide range of input parameters. These equations can be applied to designing urban drainage and road bioretention facilities, since they were developed using a large number of simulation runs with diverse input

parameters, but previous methods often overpredict the gutter flow of total interception when the longitudinal slope S_0 is small.

3.1 Introduction

The urban drainage system is designed and built to effectively convey the rainfall-runoff out of the urban area to prevent inundation and local flooding (Starzec et al., 2018), which can cause property damage and affect traffic and human safety. Curb inlets effectively intercept surface runoff into underground drainage pipes or bioretention facilities. As an important and typical practice, road bioretention facilities, which combine green/gray infrastructures to facilitate road runoff control through infiltration and storage, remove certain contaminants and sediments, and decrease roads' local flood inundation risk, are widely used in the pilot Sponge City construction in China (Li et al., 2016) and all over the world. Li et al. (2018a) found that the curb inlet could be the bottleneck of road bioretention facilities that impedes the runoff generated from the road flowing into the bioretention to infiltrate, detain (pond), and improve the stormwater quality. Tu and Traver (2018) found that the perforated distribution pipe could be an uncertain factor in road bioretention performance. Stoolmiller et al. (2018) surveyed curb inlets for road bioretention facilities in Philadelphia, and the curb inlet opening ranged from 0.15 m (6 inches) to 1.52 m (5 ft). Some of these inlets seem to have been designed based on the landscape and from a safety perspective, instead of hydraulic performance considering inlet interception efficiency.

There are three types of curb inlets commonly used along urban streets. The undepressed curb inlet has one cross slope for the road, gutter, and curb inlet. The continuously depressed curb inlet is placed in the gutter of a street with a steeper cross

slope than the road cross slope (Liang, 2018). The locally depressed curb inlet has adjacent depressions in the gutter before and/or after the inlet for effective flow interception—for example, type C and type D curb inlets, designed and constructed by the Texas Department of Transportation (TxDOT) (Mark Alan Hammonds and Edward Holley, 1995), have a 5 to 15 ft locally depressed curb opening, and 5 ft transition sections at the upstream and downstream of the opening (Figure 3.1). The upstream transition section changes elevation gradually from the undepressed section into fully depressed inlet section over the 1.52 m (5 ft) length, and the downstream transition section gradually decreases the local depression (Figure 3.1).

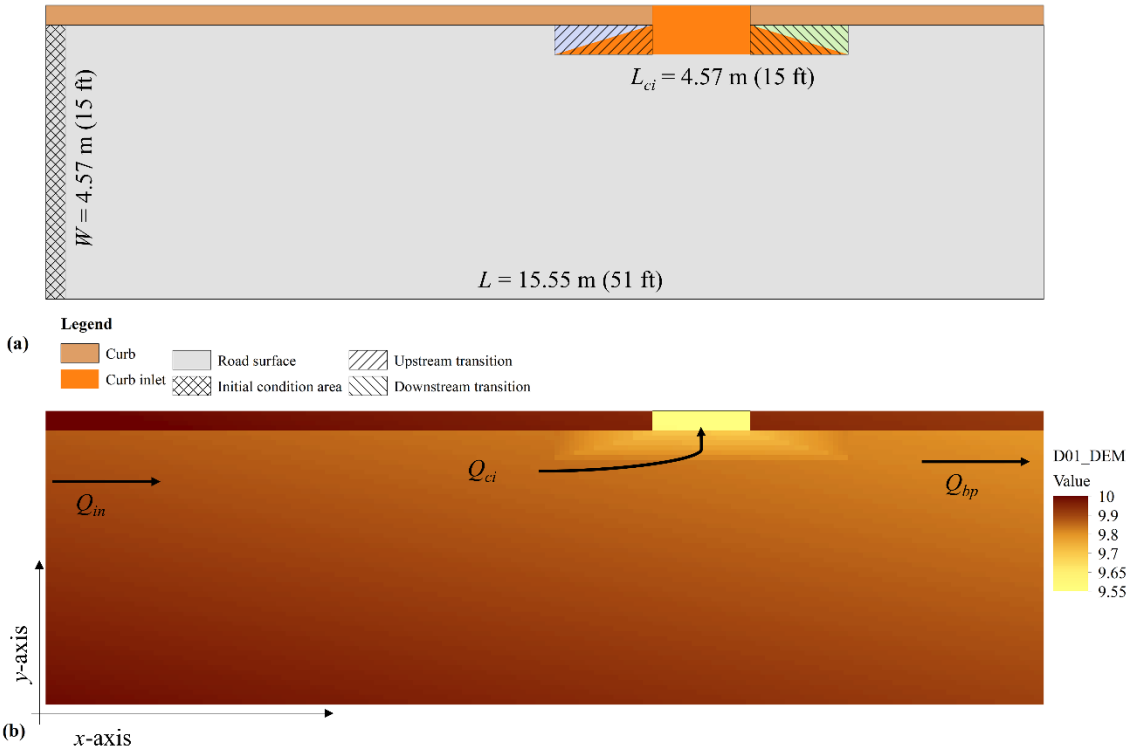

Figure 3.1. (**a**) Layout of the Type D curb inlet evaluation experiment, and (**b**) digital elevation model (DEM) of case D01 with S_0 = 0.004 and S_x = 0.0208.

The hydraulic performance of curb inlets for roadway drainage has been studied for more than 60 years, which was reviewed and summarized by Izzard (1950), Li (1954), and

presently systematically documented in the Hydraulic Engineering Circular No. 22 (HEC-22) by Brown et al. (2009). In 1979, the Federal Highway Administration (Jens, 1979) first published a technical guide for the design of urban highway drainage, and then updated it in 1984 into an HEC-12 entitled "Drainage of Highway Pavement'' (Johnson and Chang, 1984). HEC-12 summarizes a semi-theoretical method developed for estimating street hydraulic capacities and procedures for sizing street inlets. The most recent HEC-22 (Brown et al., 2009) was published and widely used in the USA and refined the design procedures stated in HEC-12.

Izzard (1950) developed equations to calculate the normal depth of gutter flow and the curb opening length (L_T) (Equation (1)) required to intercept 100% of the gutter flow. Izzard (1950) assumed that the transverse velocity of the approach flow to an inlet was zero and that the hydraulic head decreased linearly along the curb inlet. Izzard (1950) applied the usual form of Manning's equation in a local sense and calculated the total gutter flow via integrating dQ at each section and across the flow area with a uniform cross slope. Izzard (1950) compared his theoretical equation to unpublished data from experiments with less than 100% efficiency on undepressed curb inlets conducted at the University of Illinois, and determined the coefficient value in Equation (3.1):

$$L_T = 1.477 Q_{in}^{\frac{7}{16}} S_0^{\frac{9}{32}} / (n S_x)^{\frac{9}{16}} \tag{3.1}$$

where L_T is in m, Q_{in} is the upstream inflow (m^3/s), S_0 is the longitudinal slope of the road or gutter, and S_x is the cross slope (Figure 3.1), and n is Manning's roughness coefficient. Izzard (1950) developed Equation (3.2) to calculate the efficiency (E_{ci}) of a curb inlet, which is the ratio of flow intercepted by the curb inlet (Q_{ci}) and the gutter flow Q_{in} of undepressed curb inlet with the opening length of L_{ci} (m).

$$E_{ci} = \frac{Q_{ci}}{Q_{in}} = 1 - (1 - \frac{L_{ci}}{L_T})^{\frac{5}{2}} \quad (3.2)$$

For the undepressed curb inlet, Equations (3.3) and (3.4) were adapted by HEC-22 (Brown et al., 2009) to determine L_T and E_{ci}.

$$L_T = 0.817 Q_{in}^{0.42} S_0^{0.3} / (n S_x)^{0.6} \quad (3.3)$$

$$E_{ci} = 1 - \left[1 - \left(\frac{L_{ci}}{L_T}\right)\right]^{1.8} \quad (3.4)$$

Muhammad (2018) summarized previous curb inlet efficiency evaluation studies and proposed Equation (3.5) to calculate L_T and Equation (3.6) to calculate E_{ci}.

$$L_T = \frac{0.101 Q_{in}^{0.47} S_0^{0.26}}{n^{0.95} S_x^{0.75}} \quad (3.5)$$

$$E_{ci} = 1 - \left[1 - \left(\frac{L_{ci}}{L_T}\right)\right]^{\alpha} \quad (3.6)$$

Where α is not a constant, but calculated with an equation $\alpha = \frac{0.42}{S_x^{0.42}}$. When S_x ranges from 1.5% to 6%, α changes from 2.45 to 1.37.

Guo and MacKenzie (2012) stated that the HEC-22 procedure overestimates the capacity of a curb-opening inlet when the water depth is shallow, and then becomes underestimating when water depth exceeds 7 inches for 3 ft curb inlet in the sump. To determine inlet efficiency and performance, the reduced-scale physical models were used and based on Froude number scaling—that is, a 3:4 scale model for Hammonds and Holley's study (1995), 1:4 for Uyumaz's research (2002), and 1:3 for Guo and Mackenzie's tests (2012); only Schalla et al. (2017) conducted full-scale experiments for the curb inlet. The scaling effect has recently been discussed as a possible reason for significant

discrepancies in interception efficiency between field measurements and predictions of the regression equations based on scaled laboratory experiments (Comport and Thornton, 2012; Russo and Gómez, 2013).

Much more attention and focus should be paid on studying the interception efficiency of a curb inlet and its design because it is an important component for urban drainage and road bioretention facilities. Most of the currently used curb inlet E_{ci} equations were based on simple theoretical derivation with assumptions and revised coefficients or exponents determined using experimental data. In this study, the two-dimensional numerical models were first developed to represent 20 full-scale laboratory experiments of locally depressed curb inlets conducted by Hammonds and Holley (1995) and 80 experiments for undepressed curb inlets by Wesley (1961) using high-resolution digital elevation models (DEMs) for the model validation study. The overland flow on the road with curb inlets and the upstream inflow was simulated using the FullSWOF-ZG program (Li et al., 2018a), which was updated/reconfigured from an open-source two-dimensional overland flow program, FullSWOF_2D (Delestre et al., 2014). One thousand modeling cases of a road with an undepressed curb inlet with 10 S_0, 10 S_x, and 10 Q_{in} were then established and modeled to develop L_T for the 100% interception of gutter flow, and then a regression equation of L_T as a function of input parameters was developed by the multiple linear regression method. The second 1000 modeling cases of the road with 10 S_0, 10 S_x, and 10 curb inlet lengths L_{ci} were established and simulated to determine E_{ci} of different L_{ci}, and a regression equation of E_{ci} as a function of L_{ci}/L_T was also developed. The simulation results of L_T and E_{ci} were discussed and comprehensively compared with calculated/predicted results from HEC-22 (Brown et al., 2009), Izzard (1950), and

Muhamad (2018). In this study, the height of the opening of the curb inlets was not directly considered when a two-dimensional model was used. Only under severe flood situations was the height of the opening found to play a role in flow interception and inlet efficiency.

3.2 Materials and Methods

Fang et al. (2009) used a three-dimensional computational fluid dynamics (CFD) software, Flow-3D, to develop the numerical models simulating unsteady, free-surface, shallow flow through Type C and Type D (Mark Alan Hammonds and Edward Holley, 1995) curb-opening inlets. They demonstrated that an advanced CFD model could be used as a virtual laboratory to evaluate the performance of curb inlets with different geometry and inflow conditions. In this study, the two-dimensional open source FullSWOF_2D (version 1.07, Dieudonné Laboratory J.A., Polytech Nice Sophia, Nice, France) (Delestre et al., 2014) program was updated to simulate the complex flow through an inlet to determine the inlet-opening length L_T of 100% (total) interception, and the efficiency E_{ci} of an undepressed curb inlet.

The FullSWOF_2D program fully solves shallow-water equations (SWEs) (Delestre et al., 2014), depth-integrating the Navier–Stokes equations (Barré de Saint-Venant, 1871) on a structured mesh (square cells) in two-dimensional domains using the finite volume method (Unterweger et al., 2015), and is programmed using C++ to fully describe the rainfall-runoff and flow distribution progress on the surface (Gourbesville et al., 2014). As a Saint-Venant system (Barré de Saint-Venant, 1871), the SWEs model is widely used to simulate the incompressible Navier–Stokes flow occurring in rivers, channels, ocean, and land surfaces (Zhang and Cundy, 1989). It is derived with two assumptions: the water depth is small with respect to the horizontal (x, y) dimensions, and the pressure of the fluid is

hydrostatic ($\partial p/\partial z = -g$), which means the pressure field could be calculated with simple integration along the vertical (z) direction (Audusse et al., 2004). A well-balanced numerical scheme was adapted to guarantee the positivity of water height and the preservation of steady states for specific hydrological features, such as during wet-dry transitions and tiny water depth (Cordier et al., 2013). Different boundary conditions, friction laws, and numerical schemes were developed, which make the program a very powerful overland flow simulation software (Delestre et al., 2014).

The FullSWOF_2D program, which applies the uniform rainfall and infiltration parameters to the whole simulation domain, was revised by Li et al. (2018a) to include 2D plane zones (Z) with different rainfall and infiltration parameters and a 2D-1D grate-inlet (G) drainage module. Therefore, the updated FullSWOF-ZG program can simulate impervious and pervious surfaces (different infiltration parameters/capabilities in different zones) in the road bioretention domain simultaneously under rainfall events. The 2D-1D grate-inlet drainage submodule enables the program to simulate the 2D overland runoff flowing into a grate inlet, and then to a 1D underground drainage pipe using the weir equation (Leandro and Martins, 2016). In Li's study (2018a), the FullSWOF-ZG was used to evaluate the performance of a road bioretention facility and explore/understand key parameters of continuous road bioretention design. It was found that the curb inlet becomes the bottleneck of the road bioretention strip system that could impede the runoff flowing into the bioretention strip for detention and infiltration to improve the stormwater quality (Li et al., 2018a).

3.2.1 FullSWOF-ZG Validation Cases

For the reduced-scale and full-scale laboratory experiments, the curb inlet efficiency was calculated with flow intercepted by the curb inlet divided by the total upstream inflow, which did not consider the rainfall-runoff generation and concentration process. It was not meant to understand the performance of the curb inlet under a rainfall event, but to provide the information for engineering design of the curb inlet as a function of upstream inflow. Inflows with different magnitudes and spreads for curb inlets include runoff from upstream and surrounding lands and runoff produced from the roadway. Therefore, these experimental studies are valuable, and numerical model studies under the same experimental conditions were used to validate the FullSWOF-ZG model to see how well the model can predict the curb inlet efficiency. Twenty locally depressed curb inlet cases, which were tested in a laboratory by Hammonds and Holley (1995), were used to validate FullSWOF-ZG for curb inlet efficiency simulation. Eighty undepressed curb inlet cases, which were tested in a laboratory by Wesley (1961), were used to validate FullSWOF-ZG for curb inlet lengths of 100% interception.

3.2.1.1 Modeling Cases to Validate Curb Inlet Efficiency

The FullSWOF-ZG program was previously tested and verified for overland flow on pervious surfaces (Li et al., 2018a; Li et al., 2018b). In a previous study (Li et al., 2018a), the FullSWOF-ZG program was tested with 20 type C curb inlet cases. The coefficient of determination (R^2) of the linear relationship between the simulated and observed curb inlet interception efficiencies was 0.94 for type C curb inlet test cases. The differences between the simulated and observed interception efficiencies (ΔE) ranged from −3.2% to 13.2%, with an average $\pm$ standard deviation of 3.5 $\pm$ 3.5%. In this study, FullSWOF-ZG was first

tested using 20 locally depressed curb inlets (type D, Figure 3.1), which was tested in laboratory experiments by Hammonds and Holley (1995). For type D curb inlet experiments, the length and width of the simulation domain were 15.55 m (51 ft, *x*-direction) and 4.57 m (15 ft, *y*-direction), respectively. The total opening lengths of different curb inlets were either 4.57 m (15 ft) or 7.62 m (25 ft), which included a 1.52 m (5 ft) or 4.57 m (15 ft) inlet opening and 1.52 m (5 ft) upstream and downstream transition sections (Figure 1). The total width of the curb inlet depression was 0.457 m (1.5 ft), and the depressed depth was 0.10 m (0.33 ft) and 0.076 m (0.25 ft) at a depression width of 0.368 m (1.2 ft) for type C and type D curb inlets, respectively.

The simulation domain was represented by a detailed and high-resolution DEM (Figure 3.1b) with a cell size equal to 0.076 m (0.25 ft). The elevation of every computation cell was calculated using a user-developed MATLAB r2017a (MathWorks, Natick, MA, United States) (MathWorks, 2017) code with consideration of the road's longitudinal slope, cross slope, locally depressed cross slope of the curb inlet, and the slopes of the inlet's upstream and downstream transition parts. The longitudinal (*x*-direction) and cross (*y*-direction) slopes for the simulation domain are from left to right and bottom to top, respectively (Figure 3.1). Manning's law in FullSWOF-ZG was used in the simulation, and the roughness coefficient determined for the laboratory roadway was 0.018 (Mark Alan Hammonds and Edward Holley, 1995).

The imposed discharge condition in FullSWOF-ZG was chosen as the left or upstream boundary condition of the domain. The imposed discharge for the boundary cells within the spread (T) was approximately assumed as the total inflow rate (Q_{in}) divided by the number of the cells within the spread and set to be equal to 0 for other boundary cells

outside of the spread. The top and right (downstream) boundary of the simulation domain was set as a Neumann condition that allows the flow to get out of the simulation domain. At the top of the simulation domain, those cells on the curb had higher elevations to prevent the outflow. The bottom boundary of the simulation domain (Figure 3.1b) had the highest elevation along the *y*-direction, and was set as a wall boundary condition to guarantee that the flow would not pass through the bottom boundary.

3.2.1.2 Modeling Cases to Simulate/Validate Curb Inlet Length of 100% Interception

Wesley (1961) conducted a series of full-scale experiments to determine the 100% intercepted curb inlet lengths with different longitudinal and cross slopes for undepressed curb inlets. The experiment facility had a triangular cross-section with the curb side being nearly vertical, and placed on a continuous grade with no local depression on the channel bottom. The length of the curb opening was sufficient to allow for interception of all the flow from the upstream road. The experiment facility was 50 ft (15.24 m) in overall length and 6 ft (1.83 m) in width. At 32 ft (9.75 m) from the upstream end, the curb inlet opening began. This upstream length (32 ft) is sufficient for the development of a uniform flow condition. The 100% intercepted curb inlet length was then experimentally determined using the observed distribution of water depth along the curb (Wasley, 1961).

The simulation domain was represented by detailed and high-resolution DEM with a smaller cell size equal to 0.05 ft (0.015 m), similar to Figure 3.1 without local depressions. The Manning's value was 0.01, which is the same as the experiment facility. For eighty experimental cases, S_0 ranged from 0.005 to 0.05, S_x ranged from 0.01 to 0.08, and upstream inflow Q_{in} ranged from 0.18 L/s to 84.38 L/s, which were simulated to determine the 100% interception curb inlet lengths.

3.2.2 Modeling Cases to Evaluate 100% Interception Length and Curb Inlet Efficiency

After the FullSWOF-ZG model was validated to be able to accurately simulate flow over the curb inlet, 1000 modeling cases were selected and modeled to determine the curb inlet length L_T of 100% interception under different S_0, S_x, and Q_{in}. The length and width of the simulation domain for these 1000 modeling cases were 12 m (x-direction) including the 10 m road surface before the inlet and 6.7 m (y-direction, Figure 3.1) including a 3 m wide car lane stripe, 1.5 m wide bike lane strip, 2.1 m parking stripe (1.5 m + 0.6 m gutter), and 0.1 m curb width. The cell size of DEMs for all 1000 cases was 0.025 m, determined by a sensitivity analysis.

Commonly used S_0 and S_x values in stormwater drainage design were chosen from the HEC-22 (Brown et al., 2009) for 1000 modeling cases, which are the combinations of 10 longitudinal slopes S_0, 10 cross slopes S_x, and 10 upstream inflows Q_{in} (Table 3.1). Ten S_0 slopes ranged from 0.1 to 1% with an increase interval of 0.1% and ten S_x from 1.5 to 6% with an increase interval of 0.5%, respectively. Ten upstream inflows which ranged from 6 to 24 L/s with an interval increase of 2 L/s were adapted for the simulation. The case number was named using the sequence number (1 to 10) of the parameter's choice of S_0, S_x, and Q_{in}; for example, the modeling case O1X1Q1 (Table 3.1) meant the road had S_0 = 0.001 (0.1%) and S_x = 0.015 (1.5%) with Q_{in} = 6 L/s for upstream inflow. The curb length was set to be large enough to intercept 100% inflow for all 1000 modeling cases.

Table 3.1. Sequence numbers and corresponding geometry and inflow parameters of modeling cases used for FullSWOF-ZG simulations, and the results for the 20 sample cases.

Sequence No.	S_0 (%)	S_x (%)	Modeling Case Index [1]	Q_{in} (L/s)	L_T (m)	Modeling Case Index [2]	L_{ci} (L_{ci}/L_T) (m) [3]	E_{ci} (%)
1	0.1	1.5	O1X1Q1	6	3.11	O1X1L1	0.15 (0.05)	15.3
2	0.2	2.0	O2X2Q2	8	3.46	O2X2L2	0.30 (0.09)	26.4
3	0.3	2.5	O3X3Q3	10	3.79	O3X3L3	0.45 (0.12)	34.9
4	0.4	3.0	O4X4Q4	12	4.06	O4X4L4	0.60 (0.15)	41.8
5	0.5	3.5	O5X5Q5	14	4.31	O5X5L5	0.75 (0.17)	48.0
6	0.6	4.0	O6X6Q6	16	4.56	O6X6L6	0.90 (0.20)	53.8
7	0.7	4.5	O7X7Q7	18	4.76	O7X7L7	1.05 (0.22)	59.3
8	0.8	5.0	O8X8Q8	20	4.99	O8X8L8	1.20 (0.24)	64.8
9	0.9	5.5	O9X9Q9	22	5.16	O9X9L9	1.35 (0.26)	70.2
10	1.0	6.0	O10X10Q10	24	5.34	O10X10L10	1.50 (0.28)	75.7

Note: [1]—modeling case for determining curb inlet length L_T of 100% interception, [2]—modeling cases for determining inlet efficiency E_{ci} of different length L_{ci} when Q_{in} = 10 L/s, and [3]—L_{ci} in m is given outside of brackets and the ratio L_{ci}/L_T is given inside of brackets (dimensionless).

To evaluate the curb inlet efficiency E_{ci} at different inlet lengths, the second 1000 modeling cases were selected using 10 choices of L_{ci} and the same 10 choices for S_0 and S_x, which were used for the 100 modeling cases to determine L_T. Ten curb inlet lengths L_{ci} ranged from 0.15–1.5 m (6–60 inches) with an increase of 0.15 m (6 inches), which was adapted based on the curb inlet survey conducted by Stoolmiller et al. (2018). The imposed upstream inflow Q_{in} was chosen as 10 L/s for the left boundary condition of the domain for

the second 1000 modeling cases, and a part of the inflow was intercepted by the curb inlet—that is, Q_{ci} in Figure 3.1—and the remainder of the inflow was discharged downstream along the road (Q_{bp}), where the inlet length L_{ci} was less than L_T for 100% interception.

All cells' elevations were calculated using a MATLAB program when the bottom-left corner reference cell's elevation (the highest in the domain) was assumed to be 10 m (Figure 3.1b). The road surface ground elevations, therefore, varied with longitudinal and cross slopes set for each modeling case (Figure 3.1b). All cells for the 0.1 m curb were set 0.2 m higher than the road surface cells. The cell's elevations inside the curb inlet cells were calculated using the same cross slope of the road surface, which helps and allows the runoff to flow out the road surface. The total simulation duration was 120 s (1.5 min) for reaching an equilibrium condition to determine E_{ci}.

3.3 Results and Conclusions

3.3.1 FullSWOF-ZG Validation Results of Curb Inlet Efficiency

For the 20 modeling cases conducted for the type D inlet, geometry (S_0, S_x, and L_{ci}) and flow (Q_{in} and T) parameters have been listed in Table 3.2, and the same for the experimental conditions (Fang et al., 2009; Mark Alan Hammonds and Edward Holley, 1995), which cover five longitudinal slopes (0.004–0.06), two cross slopes (0.0208 and 0.0407), 17 spreads (1.05–4.27 m), and 19 upstream inflows (0.0285–0.2597 m^3/s). Table 3.2 shows that simulated intercepted flows (Q_{cis}) and inlet efficiencies (E_{cis}) matched well with the observed results (Q_{cio} and E_{cio}) from the laboratory experiments conducted by Hammonds and Holley (1995). The coefficient of determination (R^2) of the linear

relationship between simulated and observed E_{ci} is 0.99. The differences (ΔE in Table 3.2) of simulated and observed E_{ci} ranged from −2.28% to 4.21% with average ± standard

Table 3.2. Geometry and inflow parameters and simulation results of 20 Type D locally depressed curb inlet modeling cases.

Case No.	S_0 (%)	S_x (%)	L_{ci} (m)	T (m)	Q_{in} (m^3/s)	Q_{cio} (m^3/s)	E_{cio} (%)	Q_{cis} (m^3/s)	E_{cis} (%)	ΔE (%)	PD_E (%)
D01	0.4	2.08 [1]	1.52	3.05	0.0427	0.0419	98.1	0.0425	99.4	1.3	1.3
D02	0.4	2.08	1.52	4.27	0.1113	0.0768	69.0	0.0803	72.2	3.2	4.5
D03	1.0	2.08	1.52	2.32	0.0326	0.0318	97.5	0.0324	99.3	1.8	1.8
D04	1.0	2.08	1.52	4.27	0.2424	0.1004	41.4	0.1037	42.8	1.4	3.2
D05	4.0	2.08	1.52	3.07	0.1361	0.0640	47.0	0.0649	47.7	0.6	1.4
D06	6.0	2.08	1.52	4.27	0.2279	0.0735	32.3	0.0771	33.8	1.6	4.8
D07	0.4	4.17 [2]	1.52	2.4	0.0702	0.0688	98.0	0.0687	97.9	−0.1	−0.1
D08	0.4	4.17	1.52	3.33	0.1677	0.1197	71.4	0.1160	69.2	−2.2	−3.2
D09	1.0	4.17	1.52	1.99	0.0634	0.0612	96.5	0.0621	98.0	1.5	1.5
D10	1.0	4.17	1.52	2.88	0.1659	0.1092	65.8	0.1083	65.3	−0.5	−0.8
D11	2.0	4.17	1.52	1.63	0.0523	0.0511	97.7	0.0513	98.2	0.5	0.5
D12	2.0	4.17	1.52	2.64	0.1659	0.0967	58.3	0.0966	58.2	−0.1	−0.1
D13	4.0	4.17	1.52	1.25	0.0370	0.0357	96.5	0.0361	97.4	1.0	1.0
D14	6.0	4.17	1.52	1.05	0.0285	0.0279	97.9	0.0273	95.6	−2.3	−2.4
D15	4.0	2.08	4.57	4.03	0.1599	0.1137	71.1	0.1197	74.9	3.8	5.2
D16	6.0	2.08	4.57	4.27	0.1802	0.1156	64.2	0.1195	66.3	2.1	3.3
D17	0.4	4.17	4.57	3.53	0.1887	0.1874	99.3	0.1885	99.9	0.6	0.6
D18	1.0	4.17	4.57	3.41	0.2597	0.2270	87.4	0.2379	91.6	4.2	4.7
D19	2.0	4.17	4.57	2.92	0.2309	0.2024	87.7	0.2071	89.7	2.0	2.3
D20	6.0	4.17	4.57	1.91	0.1451	0.1295	89.2	0.1320	91.0	1.7	1.9

Note: [1]—cross slope 2.08% is 1 vertical versus 48 horizontal (1:48), and [2]—cross slope 4.17% is 1:24. S_0 (%) is road longitudinal slope, S_x (%) is road cross slope, L_{ci} (m) is type D curb inlet depressed part length, T (m) is upstream flow spread width, Q_{in} (m^3/s) is upstream inflow rate, Q_{cio} (m^3/s) is observed curb inlet intercepted flow rate, E_{cio} (%) is observed curb inlet intercepted efficiency, Q_{cis} (m^3/s) is simulated curb inlet intercepted flow rate, E_{cis} (%) is simulated curb inlet intercepted efficiency, ΔE (%) is difference of simulated intercepted efficiency = $E_{cis} - E_{cio}$, PD_E (%) is percent difference of simulated intercepted efficiency = $(E_{cis} - E_{cio})/[(E_{cis} + E_{cio})/2] \times 100\%$.

deviation as 1.10% ± 1.67%. The percent differences (PD_E) of simulated and observed E_{ci} ranged from −3.15% to 5.17% with average ± standard deviation as 1.57% ± 2.29%. Therefore, the FullSWOF-ZG program can accurately simulate the overland flow through the road surface, gutter, local depressions (transition), and the flow interception over Type D curb inlets, and predict the curb inlet interception efficiency well.

The simulation results in Table 3.2 were first developed using the cell size of 0.076 m (0.25 ft) for square computational grids. Three other cell sizes (0.05 m, 0.025 m, and 0.01 m) were then used for 10 modeling cases of undepressed inlets (O10X10L1–O10X10L10 in Table 3.1) to conduct the cell size sensitivity analysis on a ThinkStation Desktop computer with central processing unit (CPU) type of Intel(R) Xeon (R) E3-1241 v3 3.5 GHz. For these three cell sizes, the total number of cells in the simulation domain (12 × 6.7 m) was 32,160, 128,640, and 804,000, respectively. For the 10 cases with a cell size of 0.05 m, the simulation time ranged from 0.15 h to 0.17 h with an average simulation time equal to 0.15 h. For the 10 cases with a cell size of 0.025 m, the simulation time ranged from 1.23 h to 1.43 h with an average simulation time equal to 1.27 h. For the 10 cases with a cell size of 0.01 m, the simulation time ranged from 26.3 h to 26.4 h. The cell size of 0.025 m (~1 inch) was chosen as the simulation cell size for simulations of all other modeling cases in this study based on the balance of the model accuracy in predicting Q_{ci} and E_{ci} and the simulation time for the 10 test cases above.

3.3.2 Validation Results of 100% Intercepted Curb Inlet Length

The simulated water surface profile along the curb inlet was outputted and used by a MATLAB code to determine the 100% interception curb inlet length L_T. Figure 3.2a shows six examples of the simulated water surface profile along the curb for six selected L_T

validation cases (WS11, 23, 34, 47, 56, and 73) out of 80 experiment tests (WS1–WS80) conducted by Wesley (1961). Because the curb inlet opening starts at 9.75 m, the water depth drops sharply at the first 0.2 m of the curb inlet opening and then decreases slowly and linearly along the curb inlet. Finally, the water depth becomes very small (a thin layer of water) across the remaining inlet length. These water surface profiles along the curb inlet show similar variations with distance as reported by other research studies, such as Schalla (2017), Hodges et al. (2018), and Muhammad (2018), but are significantly different from the linear decrease assumption made and used by Izzard (1950) to develop the L_T equation.

Five depth limits (0.05 mm, 0.1 mm, 0.2 mm, 0.3 mm, and 0.5 mm) were tested to determine the end point of the 100% interception curb inlet length. The location of water depth, equal to the depth limit minus the curb inlet start location, was regarded as the 100% interception curb inlet length. The green solid vertical lines in Figure 3.2a show the location of the water depth equal to the depth limit of 0.2 mm for these six example cases. The simulated curb inlet lengths of total interception for all 80 modeling cases of Wesley's tests were determined using the five water depth limits and compared to L_T observed and determined in laboratory tests (Figure 3.2b). The final water depth limit was chosen when the root-mean-square error (RMSE) and mean absolute percentage error (MAPE) of simulated and observed curb inlet lengths of total interception were the smallest. Simulated L_T values for the 80 cases/tests ranged from 1.30 m (4.3 ft) to 5.33 m (17.5 ft).

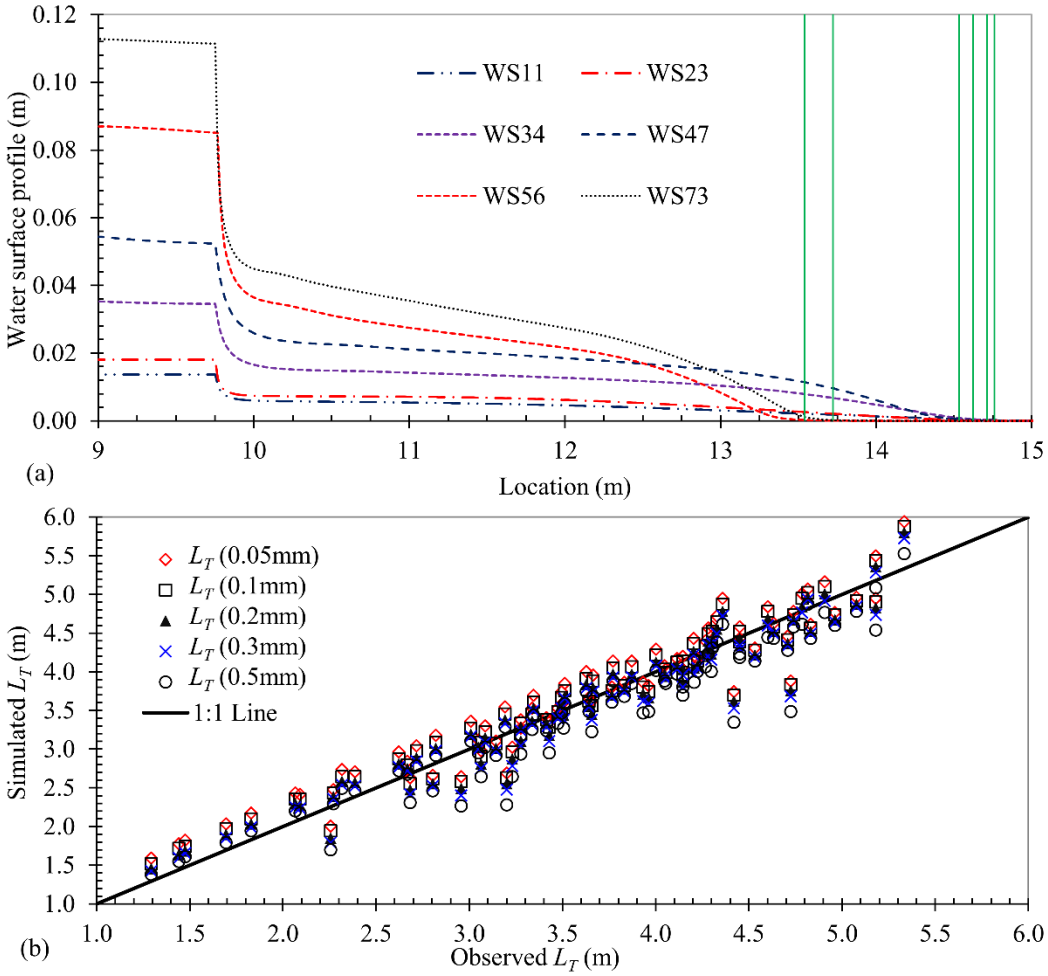

Figure 3.2. (**a**) Water surface profile along the curb inlet for six selected Wesley's tests (WS11–WS73) and (**b**) comparison of simulated using five depth thresholds (0.05–0.5 mm) and observed 100% interception curb inlet lengths for 80 laboratory tests by Wesley (1961). The solid vertical lines in (**a**) show the location of the water depth equal to the depth limit of 0.2 mm for these six example cases.

Figure 3.2b shows that the simulated L_T best matched with observed data when the depth limit for determining L_T was 0.2 mm. The RMSEs for the simulated L_T results with depth limits equal to 0.05, 0.1, 0.2, 0.3, 0.5 mm were 0.30 m, 0.28 m, 0.27 m, 0.29 m, 0.31 m, and 0.34 m, respectively. The corresponding MAPEs for the five depth limits are 7.32%,

6.46%, 6.04%, 6.08%, 6.34%, and 6.80%, respectively. Since the smallest RMSE and MAPE were for the depth limit of 0.2 mm, therefore, the water depth limit 0.2 mm was used for the one thousand modeling cases (O1X1Q1–O10X10Q10) to determine the 100% interception curb inlet lengths summarized in Section 3.3.

Figure 3.3 shows the comparison of the observed 100% interception curb inlet lengths simulated by the FullSWOF-ZG model and calculated L_T results by three existing methods for the 80 Wesley's lab tests. The RMSE values between observed and calculated L_T from HEC-22 (2009), Izzard (1950), and Muhammad (2018) are 0.56 m, 1.77 m, and 0.45 m, respectively. The corresponding MAPE values are 12.9%, 43.3%, and 7.9%, respectively. The sequence from the smallest to largest RMSE and MAPE values for simulated and calculated L_T results are Simulated < Muhammad < HEC-22 < Izzard. Izzard's equation generally overestimates L_T for all validation cases.

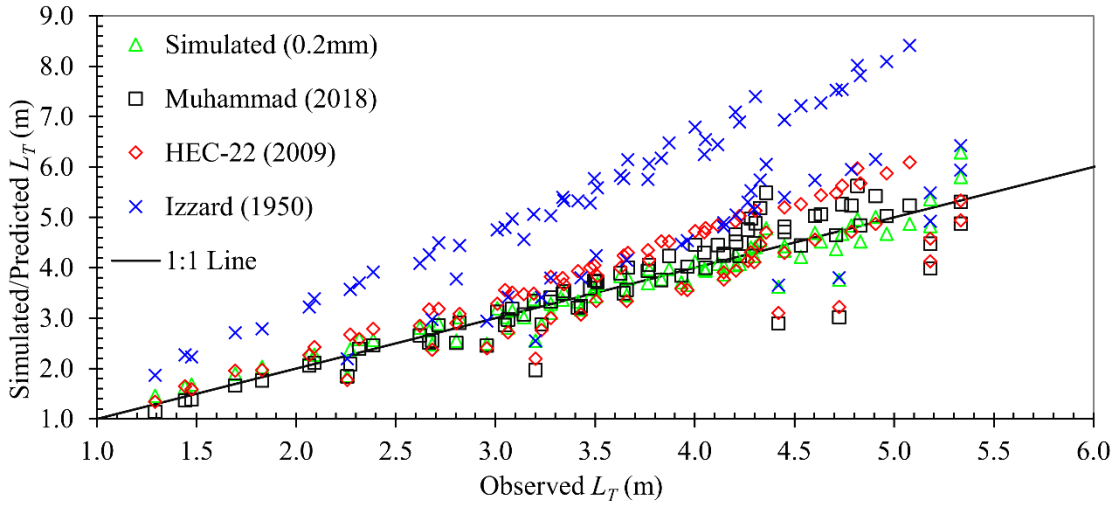

Figure 3.3. Comparison of simulated/predicted and observed 100% interception curb inlet length L_T for 80 laboratory tests by Wesley (1961).

3.3.3 Simulated Curb Inlet Lengths of 100% Interception

After L_T was determined for the 1000 modeling cases using FullSWOF-ZG, a generalized power relation, Equation (3.7) was chosen to develop the regression equation for L_T as a function of four input parameters (Q_{in}, S_0, n, and S_x). Table 3.1 also shows L_T determined for 10 example cases (OmXmQm, m = 1, 2, …, 10) using FullSWOF-ZG. In Equation (3.7) the Manning's value n and cross slope S_x were grouped as one combined variable, the same as the HEC-22 Equation (3.3).

$$L_T = kQ_{in}^{a}S_0^{b}/(nS_x)^{c} \tag{3.7}$$

where L_T is the curb inlet length in m for 100% interception; S_x and S_0 are the cross slope and longitudinal slopes of the road/street (Table 3.1), Q_{in} is the upstream inflow rate from the road/street surface to the curb inlet in m^3/s (0.006–0.024, Table 1), and n (-) is Manning's roughness of the road surface.

The variation inflation factors (VIF) among three input variables (Q_{in}, S_0, and nS_x) were calculated with MATLAB before developing the equation. The VIFs among the three variables are all equal to 1. This means the predictors are more related to the target variable L_T than they are to each other (Chatterjee and Simonoff, 2013), and the multicollinearity of three variables are not significant. The coefficient k and exponents (a, b, and c) were estimated using the multiple linear regression (MLR) method after the log transformation of Equation (3.7), and the resulting regression equation of L_T was:

$$L_T = 0.387Q_{in}^{0.372}S_0^{0.1}/(nS_x)^{0.564} \tag{3.8}$$

The 95% confidence intervals for the coefficient k and exponents a, b, and c are [0.372, 0.404], [0.368, 0.376], [0.0977, 0.103], and [0.559, 0.568] with p-value < 0.0001,

respectively. If L_T is in feet and Q_{in} is in ft^3/s for English or US customary units, the coefficient k would be 0.337. Comparing Equation (3.8) with HEC-22's L_T Equation (3.3), the exponent of S_0 in Equation (3.8) is 0.1 (1/3 of 0.3 in Equation (3.3)), and the coefficient is about a half. Muhammad's L_T Equation (3.5) made the coefficient to be much smaller (~1/8 of 0.817 in HEC-22), but other exponents are similar, in addition to having different exponents for n and S_x.

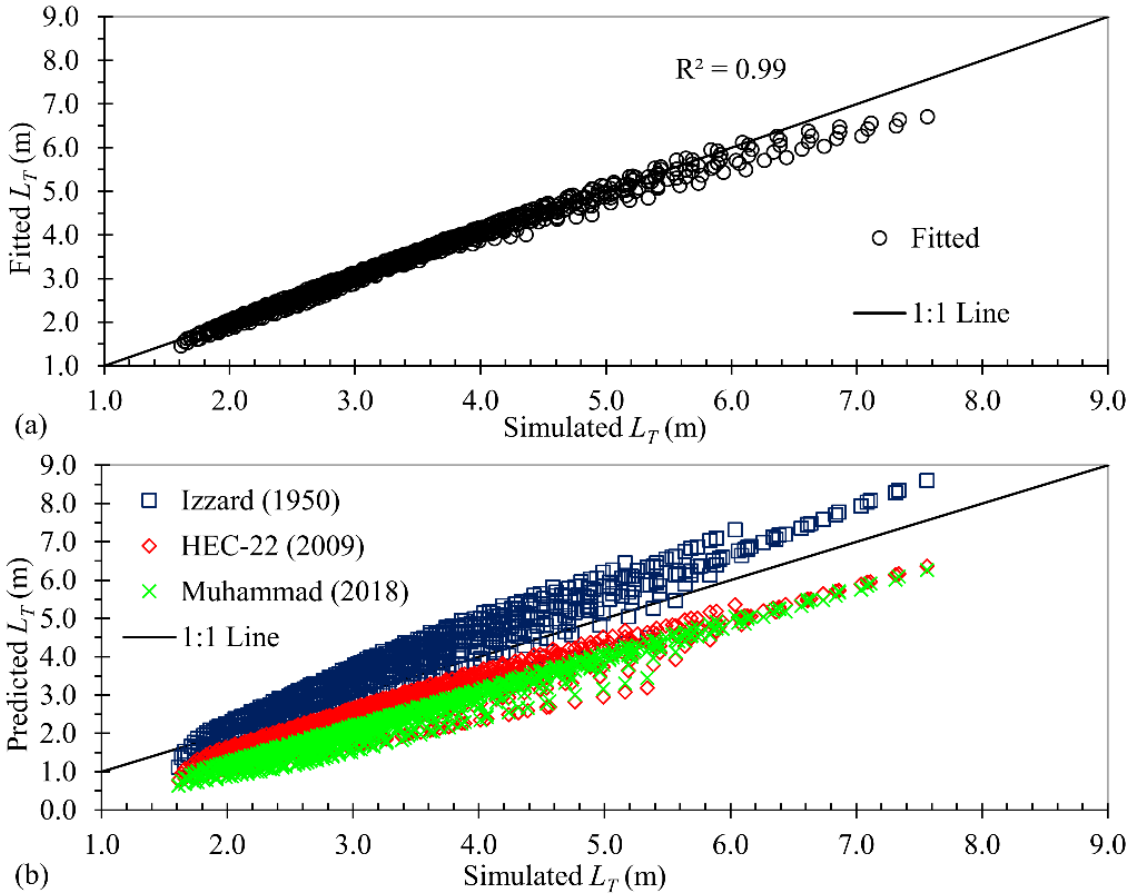

Figure 3.4. (**a**) Comparison of fitted and simulated 100% interception curb inlet lengths, L_T with Equation (8), and (**b**) predicted from Izzard (1950), HEC-22 (2009), and Muhammad (2018) versus simulated L_T for 1000 modeling cases.

Figure 3.4a shows the comparison between predicted L_T calculated using fitted Equation (3.8) (labeled as "fitted L_T" afterwards) and simulated L_T. The R^2 and RMSE

between fitted and simulated L_T are 0.99 (Figure 3.4a) and 0.13 m, respectively. The MAPE between fitted and simulated L_T is 2.34% for all 1000 cases. It shows the fitted L_T or predicted by the regression equation matched well with the simulated L_T when $L_T < 5$ m, while the difference between simulated and predicted L_T becomes larger when $L_T > 5$ m. The ratio (R_{lt}) of fitted L_T calculated using Equation (3.8) and simulated L_T was computed for all 1000 modeling cases; then, the mean R_{lt} and standard deviation for each 100 cases with the same S_0 were also calculated and plotted in Figure 3.5. When the ratio $R_{lt} = 1.0$, it means fitted L_T is exactly the same as smulated L_T. The ratio R_{lt} ranged from 0.89 to 1.06 (maximum of 11% underestimate and 6% overestimate), and the 915 fitted L_T values were within 5% from simulated L_T ($0.95 < R_{lt} \leq 1.05$) for Equation (3.8).

Figure 3.4b shows a comparison of predicted L_T results with Izzard (1950), HEC-22 (2009), and Muhammad (2018) methods to the simulated L_T results for 1000 modeling cases since no observed or measured L_T is available, and the corresponding predicted L_T in m has ranges of [1.12, 8.60], [0.78, 6.36], and [0.63, 6.27], respectively. The predicted L_T for all three methods had strongly linear correlations with simulated L_T with R^2 of 0.91–0.97. The MAPEs between predicted from HEC-22 (2009), Izzard (1950), and Muhammad (2018) and simulated L_T for all 1000 cases were 22.4%, 14.0%, and 32.3%, respectively; the corresponding RMSEs were 0.13 m, 0.22 m, and 1.01 m. The HEC-22 and Muhammad methods underestimate L_T with R_{lt} ranging from 0.48 to 0.92 (0.78 ± 0.10 for average and standard deviation) and from 0.39 to 0.84 (0.68 ± 0.09), respectively. The R_{lt} range for Izzard method was [0.70, 1.28] with an average and standard deviation of 1.08 and 0.13. For the Izzard method, 771 cases overestimated the simulated L_T.

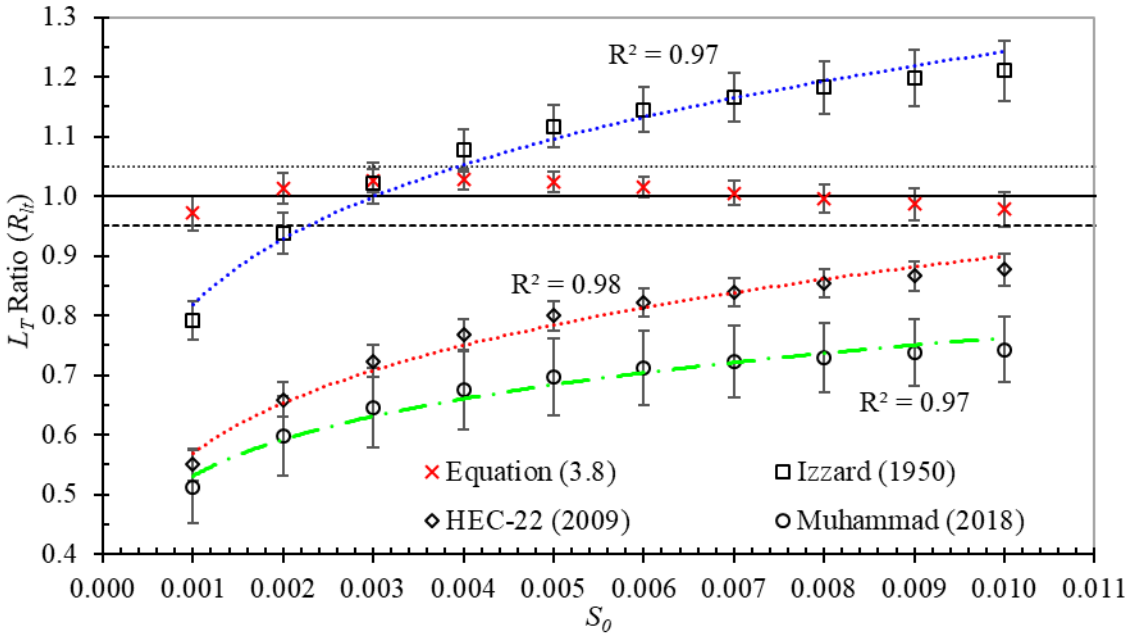

Figure 3.5. The mean ratio R_{lt} of fitted/predicted and simulated L_T as a function of longitudinal slope S_0 for 1000 modeling cases with standard deviations.

Figure 3.5 shows the average plus/minus the standard deviation of R_{lt} for Equation (3.8), Izzard (1950), HEC-22 (2009), and Muhammad (2018) with respect to different S_0 values for 1000 modeling cases. All mean R_{lt} ratios were within the range [0.95, 1.05] with small standard deviations (0.02–0.03) for fitted Equation (3.8), which indicate that the Equation (3.8) matches very well with simulated L_T for all S_0 conditions. For HEC-22 and Muhammad methods, $R_{lt} < 0.95$ for all S_0 situations and the Muhammad method has a larger standard deviation (0.05–0.07), which means the HEC-22 and Muhammad methods underestimate L_T in a greater extent under smaller S_0 situations. For the Izzard method, most of $R_{lt} > 1$ (overestimates L_T) when $S_0 \geq 0.3\%$, and it underestimates L_T when $S_0 < 0.3\%$. For three previous methods, the mean R_{lt} strongly correlates with S_0 as a power function with $R^2 > 0.97$ (Figure 3.5): R_{lt} increases with the increase of S_0.

3.3.4 100% Intercepted Gutter Flow for Drainage and Road Bioretention Design

The simulated L_T ranged from 1.61 to 7.56 m for the 1000 modeling cases (Figure 3.4a). In urban drainage design, the inlet opening lengths for various types of curb inlets standardized by municipalities and transportation agencies have only a few preset/pre-cast/manufactured lengths; for example, Texas Type C and Type D curb inlets (Mark Alan Hammonds and Edward Holley, 1995) and TxDOT precast curb inlet outside roadway (PCO) on-grade curb inlets (Hodges et al., 2018) have three opening lengths of 1.52 m (5 ft), 3.05 m (10 ft), and 4.57 m (15 ft). When the calculated curb inlet length for 100% interception is large under design gutter flow, none of the very large opening curb inlets are actually used, but continuously depressed gutter or locally depressed inlets with necessary transient lengths are typically designed and built. Therefore, Equation (3.8) from the current study, Equation (3.1) from Izzard (1950), Equation (3.3) from HEC-22 (2009), and Equation (3.5) from Muhammad (2018) were rearranged to determine the gutter flow for 100% interception (Q_{g100}) when the curb inlet length is given.

$$Q_{g100} = 12.832(nS_x)^{1.516}L_{ci}^{2.688}/S_0{}^{0.269} \tag{3.9}$$

$$Q_{g100-Izzard} = 0.410(nS_x)^{\frac{9}{7}}L_{ci}^{\frac{16}{7}}/\ S_0{}^{\frac{9}{14}} \tag{3.10}$$

$$Q_{g100-HEC-22} = 1.618(nS_x)^{1.429}L_{ci}^{2.381}/S_0{}^{0.714} \tag{3.11}$$

$$Q_{g100-Muhammad} = 131.360n^{2.021}S_x^{1.596}L_{ci}^{2.128}/S_0{}^{0.553} \tag{3.12}$$

All the above equations are for the International System of Units (SI) where L_{ci} is in m and Q_{g100} is m^3/s. Determining Q_{g100} helps us to reevaluate these L_T equations. For urban drainage design, design discharge for the gutter was calculated first based on the catchment

area, runoff coefficients of land use, and design rainfall intensity; then, the distance between two curb inlets and the curb inlet opening were calculated and selected/specified for the design.

Figure 3.6 shows the comparison of predicted Q_{g100} from Equations (3.10)–(3.12) and from Equation (3.9) for undepressed curb inlets with L_{ci} = 5 ft (1.524 m). Fourteen S_0 values were used for Figure 3.6 and from 0.003 (0.3%) to 0.04 (4%), and two small S_0 (0.001 and 0.002) in Table 3.1 were not used (HEC-22 recommends S_0 > 0.3%), and six larger S_0 (0.015, 0.03, 0.025, 0.03, 0.035, and 0.04) were added to represent the steep-slope roads for urban drainage and road bioretention curb inlet design. The 14 S_0 and 10 S_x (Table 3.1, 1.5–6%) formed 140 slope combinations that were used to compare/evaluate the above Q_{g100} equations in Figure 6. Even the overall R^2 for linear correlations of Q_{g100} predicted from three previous studies, and the newly developed Equation (3.9) are greater than 0.80, where Q_{g100} predicted by HEC-22 (2009) and Muhammad (2018) is much larger than Q_{g100} predicted by Equation (3.9). Muhammad's equation has the largest mean absolute percent deviation (MAPD), equal to 180.5%, which always overestimates Q_{g100} (Figure 3.6), in comparison to Q_{g100} from the current study. The MAPD for Izzard (1950) and HEC-22 (2009) are 25.8% and 69.1%, respectively.

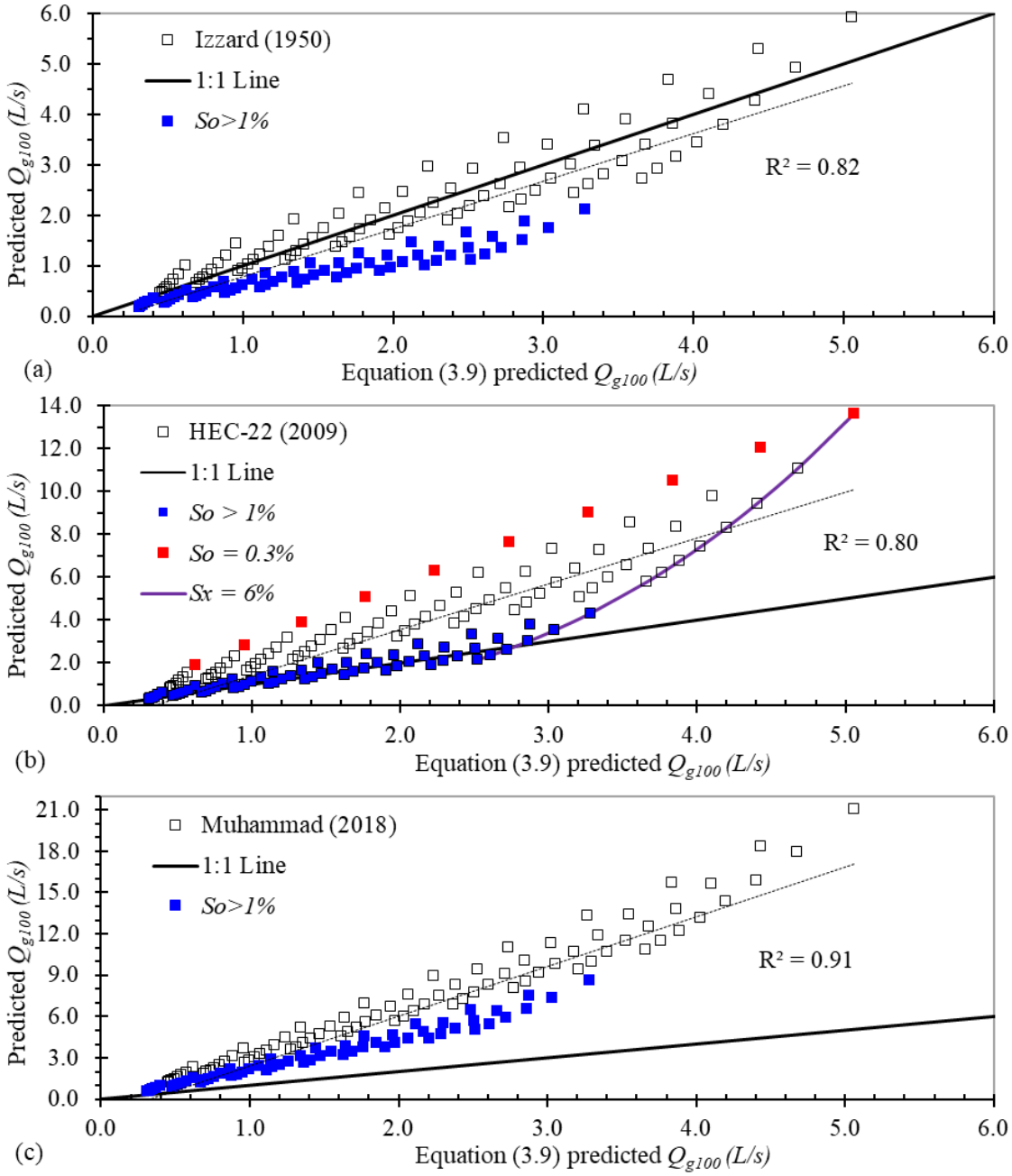

Figure 3.6. Comparison of predicted 100% interception gutter flow Q_{g100} of L_{ci} = 5 ft (1.524 m) using Equations (10)–(12) from four methods, (**a**) comparison of Izzard (1950) and Equation (9), (**b**) comparison of HEC-22 (2009) and Equation (9), and (**c**) comparison of Muhammad (2018) and Equation (3.9).

Hodges et al. (2018) compared Q_{g100} predicted using HEC-22 equation and their experimental measurements. When S_x was fixed at 6%, and S_0 changed from 4% to 0.1%, the Q_{g100} predicted using the HEC-22 equation increased about 6 times, but experimental measurements only increased less than 1.6 times. The purple line on Figure 3.6b shows the comparison of HEC-22 and Equation (3.9) predicted Q_{g100} results when S_x = 0.06 (6%). When S_0 decreased from 4% to 0.3% at S_x = 6%, Q_{g100} calculated using HEC-22 increased 6.4 times but Q_{g100} from Equation (3.9) only increased two times, which is similar to results from the physical model by Hodges et al. (2018). The smaller exponent 0.269 for S_0 in Equation (3.9) for the current study seems to give a better prediction on Q_{g100} compared to HEC-22 Equation (3.11).

In Figure 3.6b, 10 red filled squares gave Q_{g100} predicted from HEC-22 for S_0 = 0.3%, and S_x increased from 1.5% to 6%, and Q_{g100} increased from 1.8 L/s to 13.6 L/s that was, on average, 2.83 times larger than Q_{g100} (0.62–5.1 L/s) from Equation (3.9). At S_0 = 0.3%, the ratio of Q_{g100} predicted from HEC-22 to Equation (3.9) ranged from 2.69 to 3.03 with a standard deviation from the mean of 0.11, which graphically shows as a perfect linear relation of these red filled squares on Figure 3.6b. This strong linear correlation of Q_{g100} predicted from three previous studies versus Equation (3.9) exists for all other S_0 when S_x is changed. The ratio of Q_{g100} predicted from HEC-22 (2009) versus Equation (3.9) ranges from 0.85 to 3.03, and has a strong correlation with the longitudinal slope S_0: a power function $Q_{g100\text{-}HEC\text{-}22}/Q_{g100\text{-}Equation\text{-}9} = 0.213\ S_0^{-0.445}$ (R^2 = 0.99). Actually, the power function can be approximately derived by dividing Equation (3.11) to Equation (3.9). The power function clearly indicates that over-prediction occurs in smaller S_0 because of the negative exponent −0.445; for example, S_0 = 0.3%, as shown by the red filled squares. The filled

blue squares on Figure 3.6 show results for 60 cases with S_0 > 1% and S_x from 1.5% to 4%. From the power function, when S_0 is larger, the ratio of Q_{g100} is smaller, as is also clearly shown in Figure 3.6 by the filled blue squares for all three methods. Figure 3.6b shows that the predicted Q_{g100} from HEC-22 matched very well with the ones predicted from Equation (3.9) when S_0 > 1%. This means both HEC-22 and the newly developed Equation (3.9) do a very good job to predict Q_{g100} (or L_T using Equation 3.8) when S_0 > 1%. HEC-22′s Equation (3.3) for L_T and rearranged Equation (3.11) for Q_{g100} have exponents for slopes S_0 and S_x that were adjusted from Izzard's Equation (3.1) using limited available experiments, but HEC-22 did not document clearly what specific experimental data were used, which could be for experiments S_0 > 1%. The over-prediction of HEC-22 on Q_{g100} actually only occurs at lower longitudinal slopes; this could be because the HEC-22 equation was not adjusted with experimental data of small S_0. The ratio of Q_{g100} predicted from HEC-22 (2009) versus Equation (3.9) also seems to correlate with the ratio S_x/S_0 and becomes larger (over-prediction) when the ratio S_x/S_0 increases. The power function of the Q_{g100} ratio versus the ratio S_x/S_0 has a determination coefficient of 0.69, which is much weaker than the correlation with S_0 only (R^2 = 0.99).

Hodges et al. (2018) also show that, when the curb length L_{ci} = 10 ft, S_x was fixed at 6%, and S_0 changed from 4% to 0.1%, Q_{g100} calculated using HEC-22 equation over-predicts by an average factor of 1.51 when compared to measured Q_{g100} from their physical model. The ratio of Q_{g100} predicted from HEC-22 (2009) versus measurements actually ranges from 0.81 to 3.0, and the ratio of Q_{g100} predicted from HEC-22 versus Equation (3.9) also ranges from 0.85 to 2.37 (Figure 3.6), and these two results are very similar.

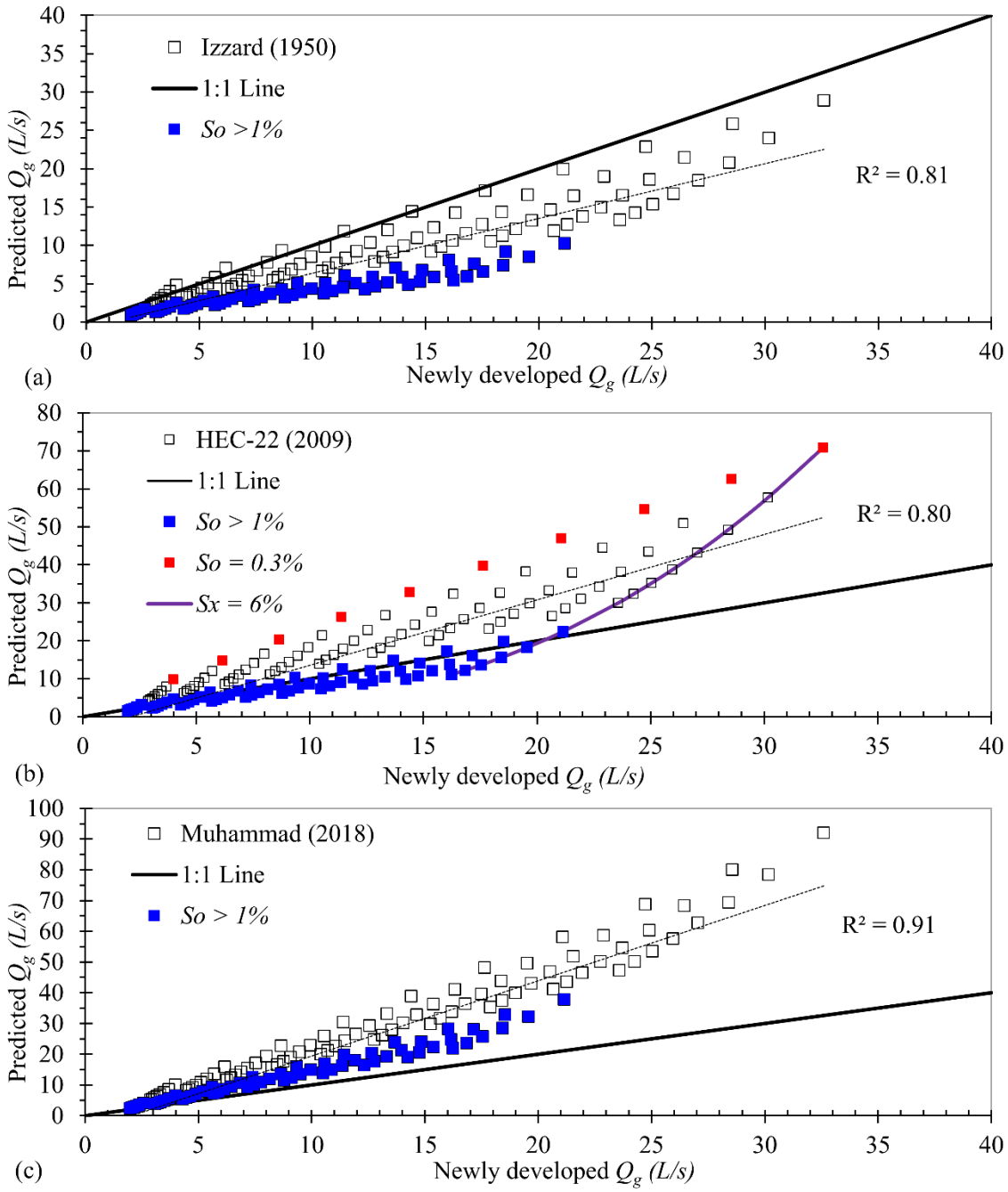

Figure 3.7. Comparison of predicted 100% interception gutter flow Q_{g100} of L_{ci} = 10 ft (3.048 m) using Equations (3.10)–(3.12) from four methods.

The comparison of predicted 100% intercepted gutter flow with Equation (3.10)–(3.12) to Equation (3.9) for curb length L_{ci} = 10 ft (3.048 m) and L_{ci} = 15 ft (4.572 m) also

gives similar results discussed above for L_{ci} = 5 ft (1.524 m) cases as shown in Figure 3.7 and 3.8.

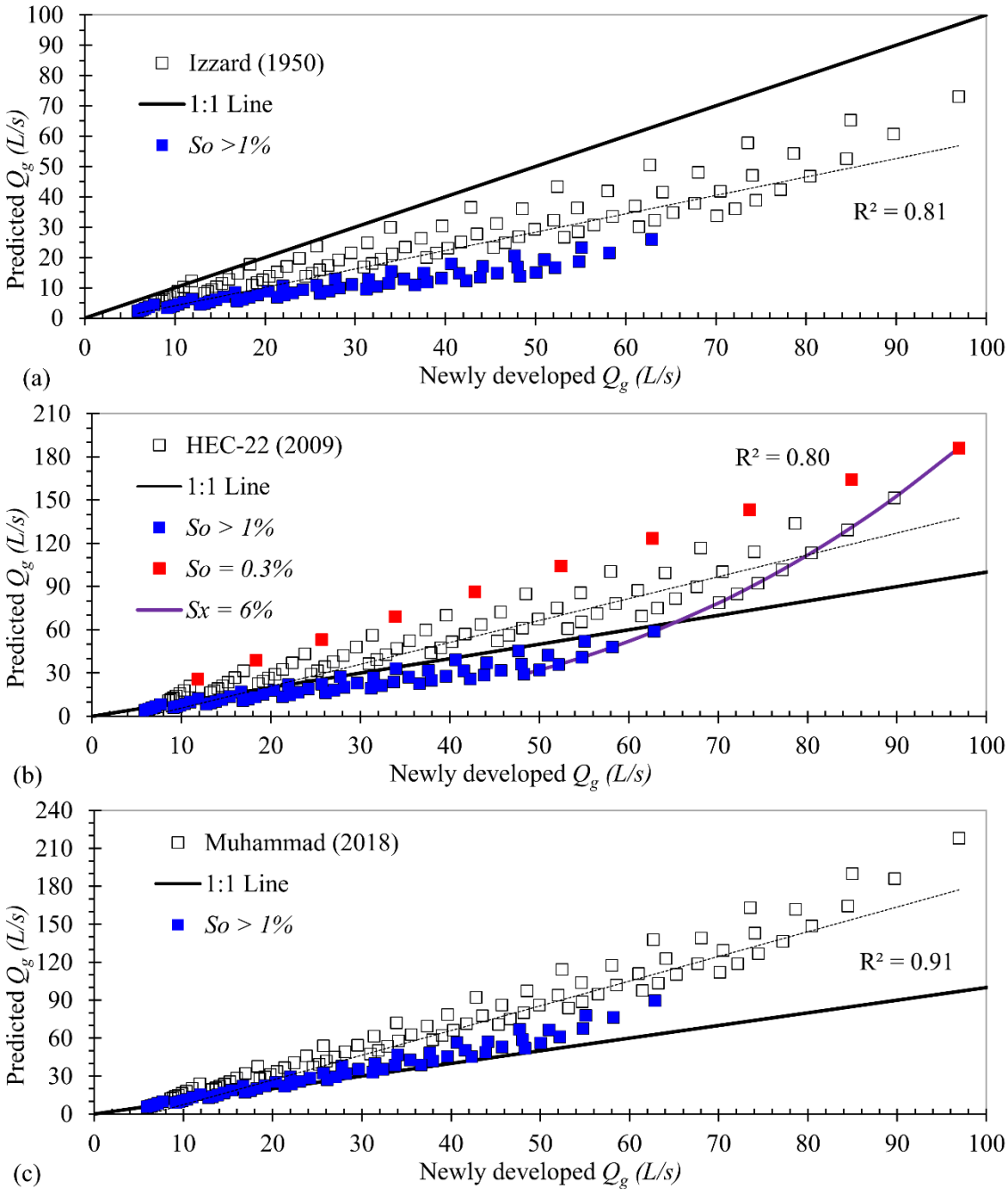

Figure 3.8. Comparison of predicted 100% interception gutter flow Q_{g100} of L_{ci} = 15 ft (4.572 m) using Equations (3.10)–(3.12) from four methods.

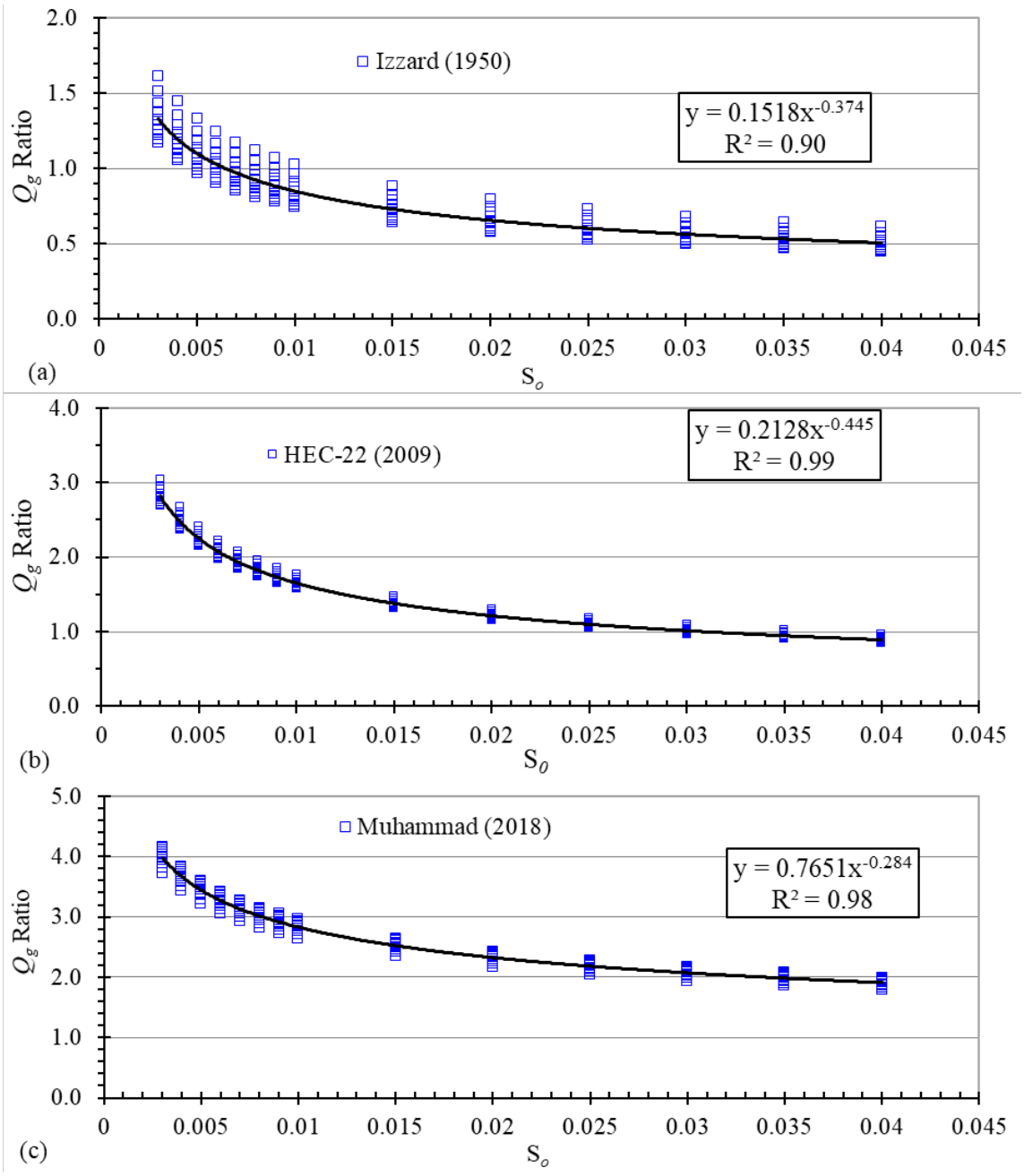

Figure 3.9. The ratio of predicted Q_g by Equations (3.10)–(3.12) to calculated Q_g by Equation (3.9) versus longitudinal slope.

Figure 3.9 shows the ratio of predicted Q_{g100} by Equations (3.10)–(3.12) to calculated Q_{g100} by Equation (3.9) for undepressed curb inlets with L_{ci} = 5 ft (1.524 m). These values of S_0 ranges from 0.003 to 0.04. Even the overall R^2 for power correlations of

Q_{g100} predicted from between three previous studies, and newly developed Equation (3.9) are greater than 0.90, Q_{g100} predicted by HEC-22 (2009) and Muhammad (2018) is always larger than Q_{g100} predicted by Equation (3.9). The Izzard (1950) overestimate Q_{g100} for part of cases with $S_0 > 0.01$ and underestimate Q_{g100} for all cases with $S_0 > 0.015$. Figure 3.9 shows HEC-22 (2009) match well with the newly developed equation (3.9) for large longitudinal slopes ($S_0 > 0.015$).

3.3.5 Simulated Curb Inlet Efficiency and Evaluation Equation

Table 3.1 shows E_{ci} determined for 10 example cases (O*m*X*m*L*m*, m = 1, 2, …, 10), which range from 15.3–75.7%. E_{ci} was calculated as the curb inlet outflow divided by the upstream inflow (Figure 3.1) when the flow through the curb inlet reaches the equilibrium—in other words, the E_{ci} change is less than 0.0005. For the second set of 1000 modeling cases (O1X1L1 to O10X10L1) of 10 different L_{ci} values (Table 3.1), the mean and standard deviations of simulated E_{ci} at the same L_{ci} were calculated. The mean E_{ci} increased from 12.8% to 84.2%, and the corresponding standard deviation increased from 5.2% to 11.8% when L_{ci} increased from 0.15 m to 1.50 m. This means inlets in the Philadelphia area (the survey conducted by Stoolmiller et al. (2018)) could intercept different amounts of stormwater runoff to road bioretention facilities, and some of them were under-designed and had flooding risks on the road.

The format of Equation (3.6) was used to develop a new relationship between E_{ci} and L_{ci}/L_T using 1000 simulated E_{ci} for 10 different L_{ci} when Q_{in} was a constant of 10 L/s. Even E_{ci} has a strong correlation with L_{ci} (R^2 = 0.86 for a power function), but L_{ci}/L_T is used in Equation (3.13) so that it can be applied to other flow rates Q_{in} from upstream road or

watershed, since L_T (Equation (3.8)) links with and has the impact of the input parameters S_0, S_x, Q_{in}, and n.

$$E_{ci} = 1 - \left[1 - \left(\frac{L_{ci}}{L_T}\right)\right]^{2.42} \tag{3.13}$$

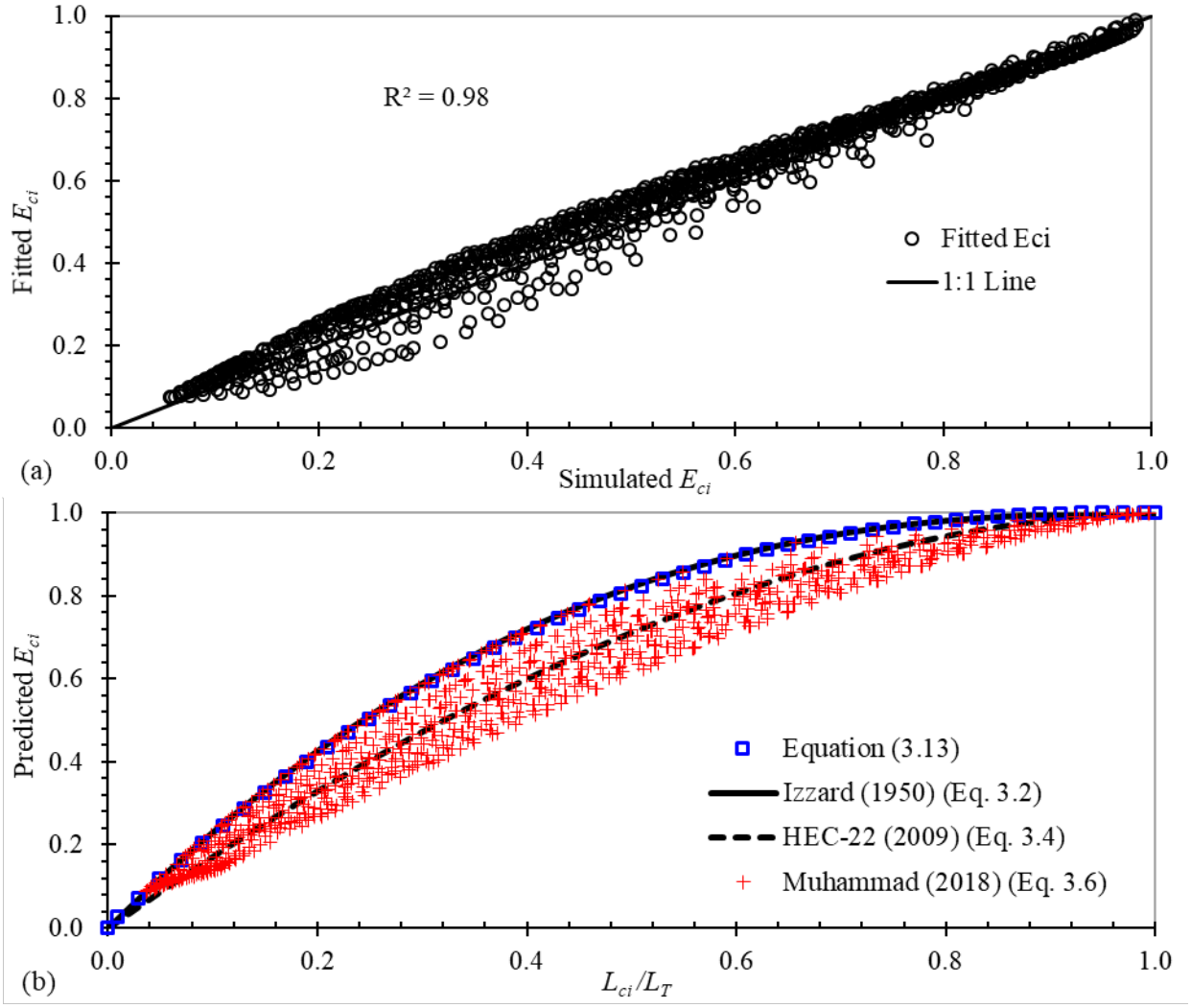

Figure 3.10. Comparison of fitted or predicted and simulated curb inlet interception efficiency E_{ci}, (**a**) comparison of fitted and simulated E_{ci}, (**b**) the relationship between predicted E_{ci} of L_{ci}/ L_T.

The exponent α was determined based on the simulated E_{ci} results of 1000 cases with the MLR method. The 95% confidence intervals for the exponents α is [2.408, 2.4358] with p-value < 0.0001. Figure 3.10a shows how the comparison of fitted and simulated E_{ci}; and fitted E_{ci} matches well with the simulated E_{ci} with R^2 = 0.98. The root mean square error (RMSE) between fitted and simulated E_{ci} is 3.93%. Figure 3.10b shows E_{ci} versus L_{ci}/L_T from the current study (fitted Equation 3.13), Izzard (1950), HEC-22 (2009), and Muhammad (2018). Fitted Equation (3.13) is almost the same as Izzard's equation (3.2) since α = 2.5, but the HEC-22 equation gives lower E_{ci}. E_{ci} predicted from Muhammad's equation has a different distribution (Figure 3.10b): different E_{ci} for the same L_{ci}/L_T when S_x is different, since the exponent α is not a constant but a function of S_x.

Figure 3.11 shows the comparison between predicted E_{ci} from Izzard (1950), HEC-22 (2009), and Muhammad (2018) method and fitted E_{ci} from newly developed Equations (3.8) and (3.13) for 10,000 design cases that are all combinations for 10 S_0, 10 S_x, 10 Q_{in}, and 10 L_{ci} listed in Table 3.1. The corresponding L_T equation for each method was applied first before L_{ci}/L_T, and then E_{ci} were calculated. When applying E_{ci} equations, E_{ci} was assumed to be 100% when L_{ci} is greater than L_T or L_{ci}/L_T > 1. Among all 10,000 cases, there are 21, 228, and 523 cases with L_{ci}/L_T > 1 for Izzard, HEC-22, and the Muhammad method when the predicted L_T is smaller than L_{ci}. The R^2, RMSE, and MAPD between predicted E_{ci} for Izzard (1950) method and newly developed equations (Equations (3.8) and (3.13)) are 0.96, 4.8%, and 8.8%, respectively. The R^2, RMSE, and MAPD of predicted E_{ci} between the HEC-22 (2009) method and newly developed equations are 0.96, 5.9%, and 9.4%, respectively. The R^2, RMSE, and MAPD of predicted E_{ci} between Muhammad's (2018) method and newly developed equations are 0.92, 8.1%, and 12.9%, respectively.

This indicates that for the 10,000 undepressed curb inlet cases from all S_0, S_x, Q_{in}, and L_{ci} combinations, when L_T and E_{ci} equations for each method are applied together to determine the inlet efficiency, the Izzard (1950), HEC-22 (2009), and Muhammad (2018) methods produced similar results, in comparison to E_{ci} from newly developed equations for L_T and E_{ci}.

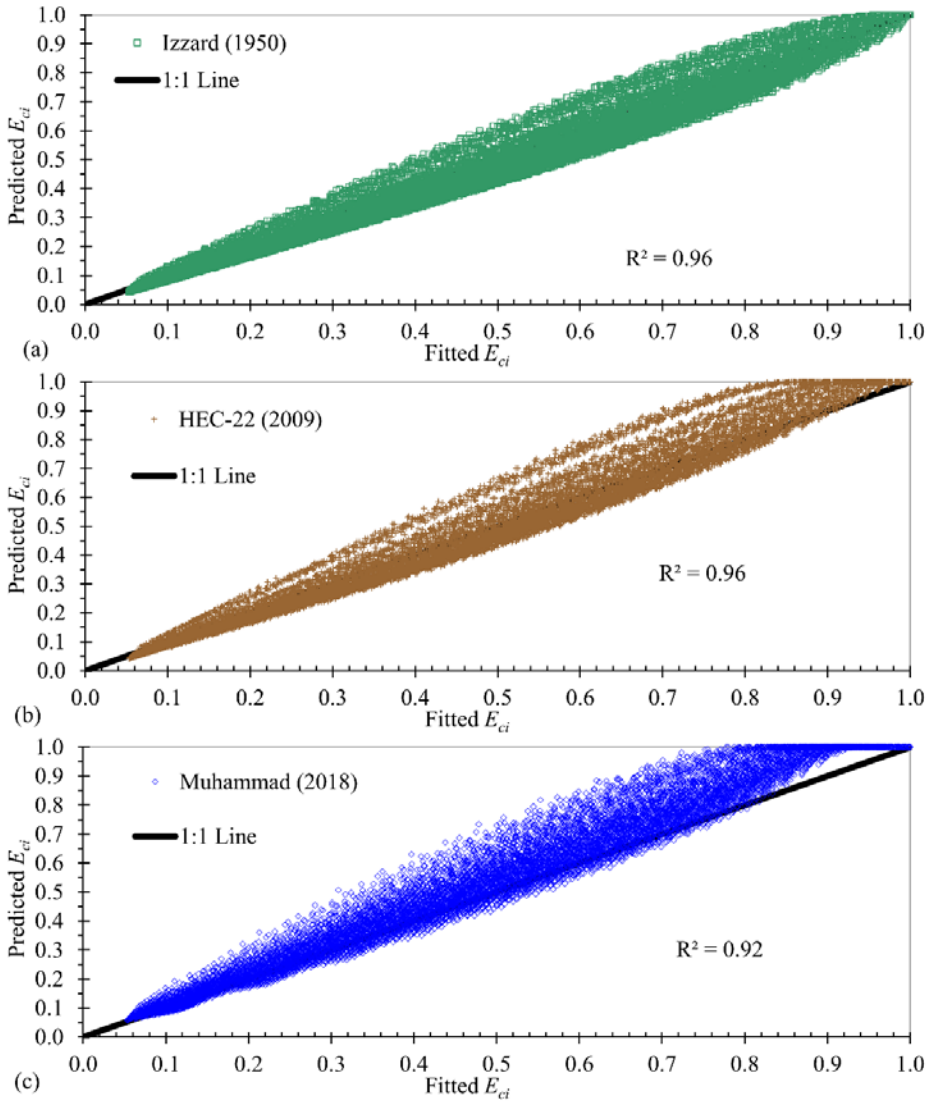

Figure 3.11. Predicted E_{ci} from Izzard (1950), HEC-22 (2009), and Muhammad (2018) versus fitted E_{ci} for 10,000 design cases for all 10 S_0, S_x, Q_{in}, and L_{ci} combinations in Table

3.1, (**a**) comparison of Izzard (1950) and fitted results, (**b**) comparison of HEC-22 (2009) and fitted results, (**c**) comparison of Muhammad (2018) and fitted results.

The ratio (R_{ci}) of predicted and fitted E_{ci} was computed and summarized to compare these four methods. For the Izzard (1950) method, the ratio R_{ci} ranged from 0.81 to 1.32 (maximum of 19% underestimate and 32% overestimate in comparison to fitted E_{ci}), and 2921 cases out of 10,000 cases were within 5% from simulated E_{ci} ($0.95 \leq R_{ci} \leq 1.05$). For the HEC-22 (2009) method, the ratio R_{ci} ranged from 0.79 to 1.39 (maximum of 21% underestimate and 39% overestimate), and 3251 cases were within 5% from simulated E_{ci} ($0.95 \leq R_{ci} \leq 1.05$). For Muhammad (2018) equation, the ratio R_{ci} ranged from 0.80 to 1.74 (maximum of 20% underestimate and 74% overestimate), and 2516 cases were within 5% from simulated E_{ci} ($0.95 \leq R_{ci} \leq 1.05$). There were 3160, 4753, and 8246 cases out of 10,000 cases overestimated E_{ci} ($R_{ci} > 1.0$) for the Izzard (1950), HEC-22 (2009), and Muhammad (2018) methods in comparison to E_{ci} from Equation (3.13). The HEC-22 underestimated L_T for most of the cases (Figure 3.4) and then made L_{ci}/L_T larger. There were still 4757 cases overestimating E_{ci} even though the L_{ci}/L_T exponent for HEC-22's E_{ci} Equation (3.4) was smaller than the exponent in the proposed Equation (3.13) and Izzard's Equation (3.2). Figure 3.8 shows that the Izzard's method and newly developed equations gave the most similar E_{ci} predictions and that the HEC-22 method gave the next most similar predictions on E_{ci}.

3.4 Summary and Conclusions

In this study, the updated FullSWOF-ZG program based on the open-source overland flow simulation program FullSWOF_2D was tested with 20 different locally depressed Texas type D curb inlet cases to simulate inlet efficiency. The differences between simulated and observed E_{ci} ranged from −2.28% to 4.21% with the average ± standard deviation being 1.10% ± 1.67%. The FullSWOF-ZG program was also validated using 80 laboratory tests to simulate the curb inlet length of 100% interception with an RMSE equal to 0.27 m and MAPE equal to 6.04%. These validation runs indicated that the FullSWOF-ZG program can accurately simulate the overland flow through the curb inlets with the high agreement and small error with observed ones so that it can be used to determine L_T and E_{ci}. One thousand undepressed curb inlet modeling cases of the road with 10 S_0, 10 S_x, and 10 Q_{in} were established and modeled to determine L_T, and then a new estimation equation of L_T was developed by the regression with the input parameters. The second set of 1000 road modeling cases of undepressed curb inlets with 10 S_0, 10 S_x, and 10 L_{ci} and a constant Q_{in} (10 L/s) were established and modeled to determine E_{ci}, and then a new estimation equation of E_{ci} was developed as a function of L_{ci}/L_T. The newly developed L_T equation was compared with three previous methods, including Izzard (1950), HEC-22 (2009), and Muhammad (2018) for predicting L_T for 1000 undepressed curb inlet cases. Finally, L_T and E_{ci} equations for four methods were applied together to predict E_{ci} for 10,000 curb-inlet cases of all ten S_0, S_x, Q_{in}, and L_{ci} combinations listed in Table 3.1. Predicted E_{ci} values for all 10,000 cases from Izzard (1950), HEC-22 (2009), and Muhammad (2018) method had RMSE < 8.5% and MAPD < 13% in comparison with ones from the newly developed L_T and E_{ci} equations in this study. The newly developed

equations gave more accurate estimations of L_T and E_{ci} over a wide range of input parameters. These equations can be applied to design urban drainage and road bioretention facilities since they were developed using a large number of simulation runs with diverse input parameters, but previous methods often overpredict the gutter flow Q_{g100} of total interception when longitudinal slope S_0 is small. Also, simulation runs were done after the FullSWOF-ZG program for overland flow simulation was comprehensively validated with 100 laboratory tests. In future studies, the equations used to evaluate the efficiency of locally depressed and continuously depressed curb inlets can be developed using simulation results from the FullSWOF-ZG program. The hydraulic-performance-based equations for different types of curb inlets should be promoted for the design of road bioretention facilities, instead of only considering landscape and safety perspective.

Chapter 4. Design and Evaluation of the Road-Bioretention Strips from Hydraulic Perspective – Case Studies

The two-dimensional overland flow simulation program, FullSWOF_2D, was revised to include submodules of determining infiltration by zones (Z) and grate-inlet (G) drainage from a 2D surface to a 1D pipe flow. The updated program, FullSWOF-ZG, was used to evaluate the performance of a road-bioretention strip (RBS) system and explore/understand key parameters of continuous RBS design. The program was validated using eight pervious surfaces under simulated rainfall events and tested with 20 experimental cases of a locally depressed curb inlet. The mean difference of simulated interception efficiencies (36.6%–86.0%) and observed interception efficiencies (34.8%–84.0%) of the curb inlet was 3.5%, which proves the program predicts the curb-inlet interception efficiency accurately. The 20 road-only and 20 RBS modeling cases were designed and modeled using the FullSWOF-ZG program. These case studies have different road lengths, curb inlet lengths, longitudinal slopes, cross slopes, bioretention-overflow inlet heights, and bioretention soil infiltration parameters. Only 34.6%–48.4% of the total runoff volume is intercepted by the RBS's curb inlet under heavy rainfall (250 mm/h), and the remaining part of the runoff flows downstream along the road, which may cause local inundation and become a safety hazard. The curb inlet becomes the bottleneck of the RBS system that could impede the runoff flowing into the bioretention strip for detention and infiltration to improve the stormwater quality.

4.1 Introduction

Over the past 40 years to 2016, China's urban population rose from 17.6% in 1977 to 57.4% of its total population, which led to rapid urbanization, and this trend will keep increasing by 1% per year to reach approximately 60% by 2020 (China, 2017). Consequently, different city syndromes, such as water shortage, water pollution, flood inundation, and ecologic deterioration, have happened frequently over the past decades, causing huge economic loss and becoming large obstacles to sustainable development in China (China, 2017; Li et al., 2017) as well as in other parts of the world (Cheshmehzangi, 2016; Moglen, 2009; Todeschini, 2016). The national New-type Urbanization Plan (2014–2020) (China, 2014) was launched in March 2014 by the Chinese central government and emphasized environmental-friendly and sustainable urbanization approaches as an important component of the blueprint(Cheshmehzangi, 2016). To endorse the sustainable urbanization plan, the Sponge City (SPC) paradigm based on green/gray stormwater management infrastructure integration was announced in 2013 as a relief countermeasure to city syndromes in China (Jia et al., 2016; Li et al., 2016; Yu and Jia, 2016).

An important component of the low impact development (LID), bioretention best management practice (BMP) in Prince George's County, Maryland (George's, 1993) is a stormwater quantity and quality control practice that facilitates decreasing surface runoff, increasing groundwater recharge, and treating various pollutants through a variety of processes (Davis et al., 2009; Dietz, 2007; George's, 2002). Many bioretention cells were used in LID practices and studied by many researchers in the past. These bioretention cells receive the runoff from different small drainage areas, such as parking lots and a few urban buildings. Bioretention BMP has been applied to diverse sites, including residential

gardens (Dietz and Clausen, 2006), parking lots (Davis, 2008; Hunt et al., 2006; Passeport et al., 2009), and along urban roads and highways (Chapman and Horner, 2010; Hatt et al., 2009; Li et al., 2011; Lucke and Nichols, 2015; Trowsdale and Simcock, 2011). Typical bioretention design includes a vegetation layer (ponding area), a soil layer (organic or mulch layer plus planting soil), a storage layer filled with gravels, an overflow inlet, and an optional underdrain (perforated pipe) (Figure 4.1).

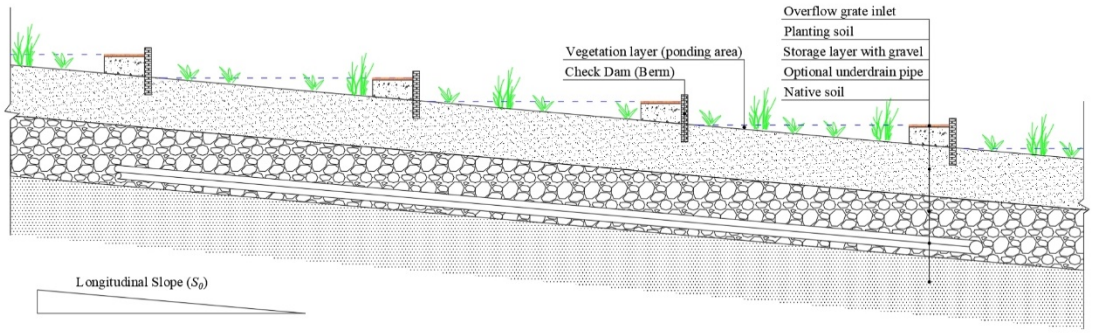

Figure 4.1. Schematic diagram of a continuous road-bioretention strip.

When saturated hydraulic conductivity is less than 13 mm/h, an underdrain system for infiltrated water is required, which flows to the outfall point (Davis et al., 2009). As an important and typical practice, a continuous road-bioretention strip (RBS) (Figures4.1 and 4.2), which combines green/gray infrastructures to facilitate road runoff control through infiltration and storage as well as decreasing road local flood inundation risk, is widely used in the pilot SPC construction (Li et al., 2016). A continuous RBS is built along an urban road or street over a relatively long distance and could be separated into several cells/units by check dams (berms) when the longitudinal slope is large enough. The slope and distance between two check dams control the ponding depth and length in the RBS.

When the slope is small, the RBS could be one single elongated cell containing tree planters (Figure 4.2).

Figure 4.2 shows four RBS projects in four SPC pilot cities, indicating that road-bioretention systems are widely built in China. Figure 4.2a is a continuous RBS built in the Beijing Economic-Technological Development Area. The vegetation in the bioretention strip is very dense, and its vegetation volume is a large fraction of the bioretention ponding volume. The concern is that dense vegetation may affect the ponding process of runoff. Figure 4.2b, c present two projects built in Shenzhen, Guangdong province and Jinan, Shandong province, respectively. The bioretention strips with tree planters were constructed on the right-of-way. Figure 4.2d presents a road-bioretention project in Ningbo, Zhejiang province; its bioretention curb inlet was designed mainly from the landscape perspective rather than for the flow intercepting function purpose. Different from right-of-way bioretention cells constructed in the USA, road-bioretention projects in SPC pilot cities are always very long along the roadside and are combined with tree planters (Li et al., 2016). Different types of curb inlets (outlined by red rectangles in Figure 4.2) have been used in different projects while no guidance for designing curb inlets of the RBS systems is available. These RBS curb inlets were designed from the landscape and safety perspective and based on experience rather than research findings on RBS' curb inlet interception efficiencies. Continuous RBS performance on intercepting road runoff and reducing local flooding under different rainfall events or upstream inflows is still unclear. Key design parameters of continuous RBS also need to be explored and determined.

Figure 4.2. Continuous road-bioretention strip in (**a**) Beijing (curb inlet length L_{ci} = 0.5 m) taken by Yongwei Gong, (**b**) Shenzhen (L_{ci} = 0.4 m) taken by Yongwei Gong, (**c**) Jinan (L_{ci} = 0.4 m) taken by Xiaoning Li, and (**d**) Ningbo (L_{ci} = 0.3 m) taken by Jianlong Wang. Red boxes show curb inlets and yellow boxes show overflow grate inlets in the bioretention cells.

Normally, each RBS cell has an overflow grate inlet at the downstream end and near the berm, and the overflow height (h_b), as an important design parameter, is the grate inlet height above the ground surface of the RBS (Figure 4.1). When the rainfall starts, runoff generated from the road flows into the RBS through curb inlets and infiltrates into the soil first. Then, after the soil is saturated, surface ponding occurs inside the RBS. When the ponding depth is greater than the overflow height, the runoff begins to flow into the grate inlet and then to the underground stormwater sewage system. When the infiltrated runoff reaches the storage layer of the RBS, it can drain through the perforated pipe.

Most previous studies indicate that bioretention BMPs have good hydrologic performance and pollutant removal efficiency in treating urban road runoff based on experimental and monitored data (Li et al., 2014). There was limited guidance and study on RBS design in China (Development, 2016; NACTO, 2017). In the study conducted by Manganka et al. (2015), the influence of rainfall characteristics, and inflow and outflow discharge on bioretention pollutant treatment performance was explored using conceptual model simulation data. Manganka et al. (2015) found that the antecedent dry period is the most important factor affecting bioretention pollutant treatment efficiency while the study did not link the bioretention performance to actual design parameters directly. To evaluate and design RBS, the influence of design parameters, including the catchment area, longitudinal slope, road/street cross slope, curb inlet length, bioretention overflow height, and infiltration capacity, on RBS performance still needs to be explored.

Much more attention and focus should be paid to studying the curb inlet interception efficiency and its design because the curb inlet is an important hydraulic infrastructure for RBS. The curb inlet allows surface runoff on the road to get into bioretention cells and influences the road-bioretention strip's performance directly (NACTO, 2017). Some previous studies have explored the curb inlet interception efficiency evaluation (Comport and Thornton, 2012), efficiency limitation (Schalla et al., 2017), and influence factors (Guo, 2006) in urban drainage while not much research was found on curb inlets in RBS. An evidence-based curb inlet design guide for RBS is of great importance and urgency because current practices do not address RBS' hydraulic performance needs (Development, 2016). It is important to design a continuous RBS with a high curb-inlet interception

efficiency and grate-inlet capacity to reduce the runoff on roads, ensure traffic safety, and relieve local flood inundation.

To understand the influence of design parameters for RBS, a performance evaluation of RBS is particularly important (Jia et al., 2017). The main purpose of the study is to understand how the runoff generated from the upstream road is intercepted by the curb inlet and the grate inlet on the road and how the flow interception further influences the hydrological performance of the RBS system. In this study, the submodules for determining infiltration by zones (pervious and impervious zones in the simulation domain, Figure 4.2) and grate-inlet drainage from the 2D surface to the 1D pipe were added to the open source FullSWOF_2D (version 1.07, Lab. J. A. Dieudonné & EPU Nice Sophia, Nice, France) (Delestre et al., 2014) program to explore the continuous RBS performance and design concerns; the updated program was called FullSWOF-ZG. FullSWOF_2D means full shallow-water equations (SWEs) for overland flow in two-dimensional (2D) analysis which is programmed using C++ to fully describe the rainfall-runoff and flow distribution progress on the surface in two-dimensional domains (Gourbesville et al., 2014). Therefore, the FullSWOF-ZG program can simulate impervious and pervious surfaces (different infiltration parameters/capabilities in different zones) in the RBS domain simultaneously under rainfall events. The 2D-1D grate-inlet drainage submodule enables the program to simulate the 2D overland runoff flowing into a grate inlet then to a 1D underground drainage pipe using the weir equation (Leandro and Martins, 2016).

4.2 Materials and Methods

4.2.1 Road-Bioretention Strip (RBS) Design

The continuous RBS is mainly designed to remove runoff from the road, reduce local flood inundation, and improve runoff quality through bioretention. Curb inlet interception efficiency, bioretention ponding volume, bioretention infiltration capacity, and road grate inlet capacity should be taken into consideration when designing a continuous RBS.

4.2.1.1 Curb Inlet Interception Efficiency Calculation

There are three types of curb inlets commonly used in the USA. The undepressed curb inlet, which has one cross slope for the road and gutter so that the curb inlet has the same elevation as the nearby road surface (Figure 4.2), is also widely used in China (Development, 2016). The continuously depressed curb inlet is placed in gutters of streets with a composite cross slope (Liang, 2018). The locally depressed curb inlet has an adjacent depression in the gutter near the inlet for effective flow interception, such as type C (Figure 4.3) and type D curb inlets designed and constructed by the Texas Department of Transportation (Mark Alan Hammonds and Edward Holley, 1995).

Current curb inlet designs in the USA are based on Hydraulic Engineering Circular No. 22 (HEC-22) from the Federal Highway Administration (Brown et al., 2009) and the Urban Street Stormwater Guide from the National Association of City Transportation Officials (NACTO, 2017). Design procedures of commonly-used inlet types are presented in HEC-22, and other specific design guidance is provided in different studies (Comport and Thornton, 2012; Mark Alan Hammonds and Edward Holley, 1995). The interception

efficiency (E_{ci}) of undepressed curb inlets is calculated using the following Equations (4.1)–(4.3) adopted from HEC-22:

$$Q = \left(\frac{0.376}{n}\right) S_x^{1.67} S_0^{0.5} T^{2.67} \tag{4.1}$$

$$L_T = 0.817 Q^{0.42} S_0^{0.3} \left[\frac{1}{n S_x}\right]^{0.6} \tag{4.2}$$

$$E_{ci} = 1 - \left[1 - \left(\frac{L_{ci}}{L_T}\right)\right]^{1.8} \tag{4.3}$$

where L_T (m) is the theoretical curb-inlet length required to intercept 100% of the flow; E_{ci} *(%)* is the inlet interception efficiency; L_{ci} (m) is the curb inlet length; S_x and S_0 are the cross slope and longitudinal slope of the road/street, Q is the flow rate on the road/street surface; T is the spread width of the flow on the road/street surface; and n (-) is Manning's roughness of the road surface.

4.2.1.2 Bioretention Ponding Volume and Infiltration Capacity

Overflow height/ponding depth provides a temporary storage space for stormwater runoff before it filters downward through the bioretention facility. The temporary ponding depth for bioretention facilities ranges from 5 cm (for mitigating sidewalk runoff alone, or in fast-draining soils) to up to 30 cm (for mitigating roadway runoff, or in slower-draining soils) (NACTO, 2017). The Delaware Green Technologies Design Manual and Model provides design guidance for bioretention systems, and allows a maximum ponding depth of 45 cm (Control, 2005). Allen et al. (Davis et al., 2009) declared the overall principles of the bioretention ponding volume and infiltration capacity design in their study. The

ponding volume is designed by the corresponding catchment area and the design's rainfall depth.

The initial bioretention design specifications suggested the use of natural soils with high permeability (George's, 1993). Three soil textural classifications were specified, which include: Loamy sand, sandy loam, and loam. The Green-Ampt model was adopted to simulate the bioretention infiltration process in this study. The infiltration parameters included the saturated hydraulic conductivity (K), moisture deficit ($\Delta\theta$), and suction head (φ). RBS with three different soils were studied here: Loamy sand (K = 51 mm/h, $\Delta\theta$ = 0.410, φ = 0.09 m), sandy loam (K = 25 mm/h, $\Delta\theta$ = 0.435, φ = 0.218 m), and loam (K = 13 mm/h, $\Delta\theta$ = 0.451, φ = 0.478 m); and their infiltration parameter values were adopted based on the soil type (Davis et al., 2009). The thickness of the soil layer was 0.45 m according to the bioretention design cases (Hatt et al., 2009).

4.2.2 FullSWOF-ZD Program and Model Test

In this study, the open-source FullSWOF_2D program was revised and improved, and the updated program is called FullSWOF-ZG. The simplified SWEs model, as a Saint-Venant system (Barré de Saint-Venant, 1871), is widely used to simulate the incompressible Navier–Stokes flow occurring in rivers, channels, oceans, and land surfaces (Zhang and Cundy, 1989). The 2D SWEs for the FullSWOF_2D program, including the continuity equation and two momentum equations in the x and y directions, are stated as the following equations for each computational cell (center coordinates x and y):

$$\frac{\partial h}{\partial t} + \frac{\partial hu}{\partial x} + \frac{\partial hv}{\partial y} = R_i(x, y) - f(x, y) \tag{4.4}$$

$$\frac{\partial hu}{\partial t} + \frac{\partial}{\partial x}\left(hu^2 + \frac{gh^2}{2}\right) + \frac{\partial}{\partial y}(huv) = -gh\left(\frac{\partial z}{\partial x} + S_{fx}\right) \tag{4.5}$$

$$\frac{\partial hv}{\partial t} + \frac{\partial}{\partial x}(huv) + \frac{\partial}{\partial y}\left(hv^2 + \frac{gh^2}{2}\right) = -gh\left(\frac{\partial z}{\partial y} + S_{fy}\right) \tag{4.6}$$

where $R_i(x, y)$ (m/s) is the cell's rainfall intensity; $f(x, y)$ (m/s) is the cell's infiltration rate; h (m) is the cell's water depth; z (m) is the cell topography elevation as a function of the cell location or x and y coordinates; u (m/s) and v (m/s) are the cell's depth-averaged velocities in the x and y directions, respectively; S_{fx} and S_{fy} are the cell's friction slopes in the x and y directions, respectively; g (m/s^2) is the gravity acceleration; and t (s) is time.

The FullSWOF_2D program fully solves SWEs on a structured mesh (square cells) in two dimensions using the finite volume method that ensures mass conservation compared to the finite difference method (Unterweger et al., 2015). A well-balanced numerical scheme was adopted to guarantee the positivity of water depth and the preservation of steady states for specific hydrological features such as during wet-dry transitions and tiny water depths (Cordier et al., 2013; Delestre et al., 2014). Different boundary conditions, friction laws, and numerical schemes were developed that make the program a very powerful overland flow simulation software. A modified bi-layer (crust- and soil-layer) Green–Ampt infiltration model (Esteves et al., 2000) to calculate $f(x, y)$ for Equation (4.4) was coded in the FullSWOF_2D (Unterweger et al., 2015), which enables the program to simulate the overland flow on impervious and pervious surfaces simultaneously.

The updated FullSWOF-ZG program includes the rainfall input and the infiltration determination by zone and a new 2D-1D drainage inlet submodule. Therefore, the program

can simulate impervious road (Figures 4.3 and 4.4) and pervious bioretention surfaces (Figure 4.4) with different infiltration capabilities simultaneously. The simulation domain can have several grate inlets (Figure 4.4); therefore, the 2D overland flow can drain into these 2D grate inlets (rectangles) to become a 1D flow in underground drainage pipes. Currently, the FullSWOF-ZG program does not further simulate the 1D flow in the drainage pipes, assuming the pipe capability is large enough to accept all inflow from inlets (Brown et al., 2009). The simulation domain has curb inlets connecting the road (impervious surface) and the RBS (Figures 4.2 and 4.4). Normally, the runoff on the road flows through the curb inlet(s) into the RBS. Only under extreme conditions would the runoff in the RBS be able to flow back to the road, but the extreme conditions were not simulated in this study.

The grate-inlet flow-intercepting capacity (Q_{gr}, m^3/s) from the 2D overland flow to the 1D drainage pipe flow is calculated using the weir Equation (4.7) (Leandro and Martins, 2016) applied to the k cells within the grate inlet:

$$Q_{gr} = \sum_{i=1}^{k} k_w \sqrt{2g} L_w h_{2D(i)}^{\frac{3}{2}} \tag{4.7}$$

where k_w (-) is the discharge coefficient of the weir flow = 0.368 (Akan, 2006); g (m/s^2) is the gravity acceleration; L_w (m) is the flow length (=cell size); $h_{2D(i)}$ (m) is the overland-flow water depth for the i^{th} cell; and k is the total number of the cells within the grate inlet. Each grate inlet in the simulation domain is considered to have an elevation difference (e.g., 5 cm lower) from the surrounding road cells.

Figure 4.3. (**a**) Layout of type C curb inlet evaluation experiment (top view), and (**b**) DEM of case C01 with a longitudinal slope, S_0 = 0.004, and cross slope, S_x = 0.0208.

The FullSWOF_2D program was previously tested and verified for overland flow on pervious surfaces (Li et al., 2018b). In this study, FullSWOF-ZG was tested separately using two kinds of modeling cases: eight pervious surfaces under indoor simulated rainfall events and twenty curb inlets with local depression and inflow from upstream. The inlet geometry was represented by the detailed high-resolution digital elevation model (DEM). These testing cases are described below in detail separately.

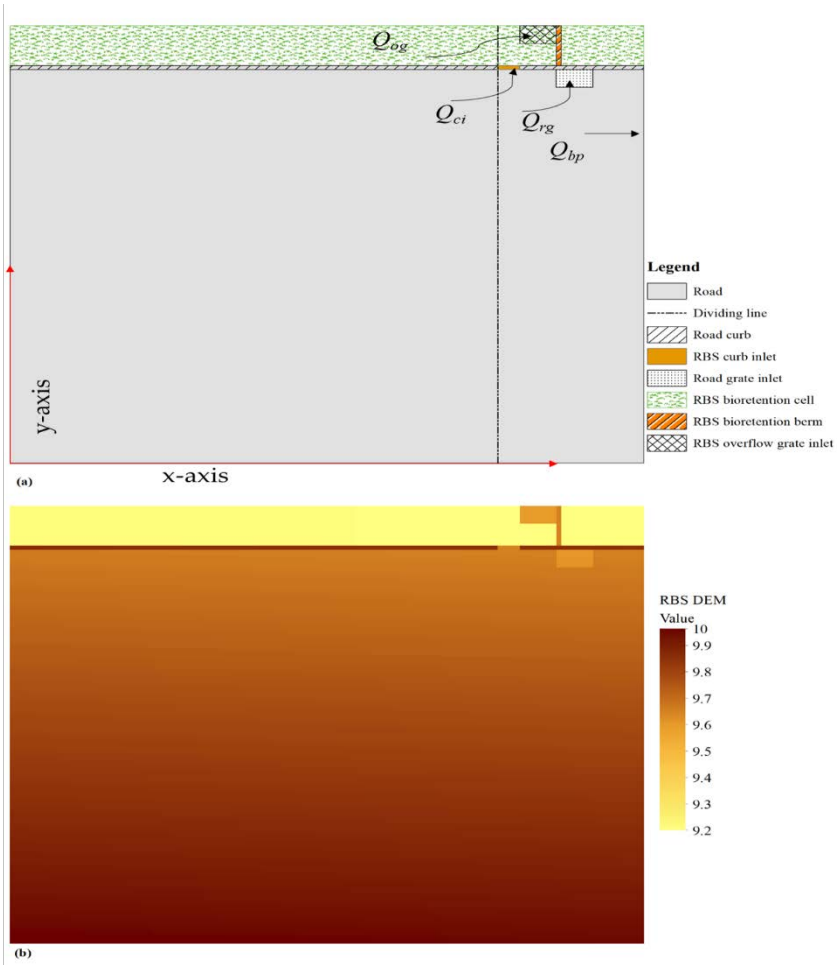

Figure 4.4. (**a**) Plan view and (**b**) DEM for RBS04 (Table 4.1) with a longitudinal slope, S_0 = 0.001, and cross slope, S_x = 0.030.

4.2.2.1 Pervious Surface Modeling Cases

FullSWOF-ZG was validated using eight pervious surfaces under indoor simulated rainfall events as testing cases to demonstrate that it can be used to accurately simulate overland flow on pervious surfaces. The experiment was conducted at Texas A&M University to investigate the travel time and runoff characteristics of overland flow on pervious clay surfaces. The data from indoor tests consist of the discharge rate and surface runoff depth under a varying rainfall intensity and slope of the surface.

The tests were conducted on a steel-framed bed 1.83 m (6 ft) wide, 9.14 m (30 ft) long, and 0.36 m (14 in) deep. The test bed was filled with clay and compacted with a lawn roller and left outdoors for over a month for natural compaction. The experiments were conducted using a rainfall simulator with a maximum capacity of up to 114.3 mm/h (4.5 in/h). Two samplers equipped with bubbler flow modules were used to collect discharge depths and surface runoff depths near the outlet with 2.54×10^{-6} m (0.0001 in) resolution every minute. The discharge depth was measured with a 22.5° V-notch weir box. The rainfall intensity was monitored using an inline flowmeter connected to the rainfall simulator. The tipping bucket rain gauge was also used to double check the rainfall depth. The rainfall was stopped at 10 min after the peak discharge was attained and the discharge measurement was done until the runoff ceased. The slope of the test bed was 0.02%, 0.1%, 0.2%, 0.5%, and 1.04%. Different slopes for the overland flow were achieved by raising or lowering the steel-framed bed. Six rainfall events were tested for each slope, with a total of 30 events for the experiment.

Eight of the 30 rainfall events were chosen as the test cases in this study. Four test cases had a slope of 0.1%, three cases of 0.2%, and one case of 0.5%. The cell size in the x- and y-directions of the simulation domain was 0.15 m (0.5 ft). The Manning's friction formula with $n = 0.02$ was selected among three friction formulas of FullSWOF-ZG. The Green-Ampt model was used to simulate the infiltration process of the experiment. The saturated hydraulic conductivity (K = 1.524 mm/h), moisture deficit ($\Delta\theta$ = 0.15), and suction head (φ = 0.208 m) parameters' values were adopted in the simulation based on the field survey.

The goodness of fit for the simulated hydrograph was evaluated using the Nash-Sutcliffe efficiency (NSE) coefficient (Nash and Sutcliffe, 1970):

$$NSE = 1 - \frac{\sum_{i=1}^{m}(Q_{oi} - Q_{si})^2}{\sum_{i=1}^{m}(Q_{oi} - \bar{Q})^2} \tag{4.8}$$

where Q_{oi} (m^3/s) is the *i*th observed runoff rate, Q_{si} (m^3/s) is the corresponding simulated runoff rate, $\bar{Q}$ (m^3/s) is the mean observed runoff rate, and m (-) is the total number of observed runoff rates. The NSE values for eight rainfall events were calculated to evaluate the FullSWOF-ZG performance.

4.2.2.2 Curb Inlet Modeling Cases

Hammonds and Holley (1995) performed a series of laboratory experiments of Texas type C and type D locally depressed curb inlets to quantify the interception efficiencies of these inlets under different longitudinal slopes, cross slopes, and upstream inflows. Only the type C curb inlet geometry (Figure 4.3) and monitored data were used in this study to evaluate the FullSWOF-ZG model.

According to the dimensions of the experimental facility, the length and width of the simulation domain were 15.55 m (51 ft, *x*-direction) and 4.57 m (15 ft, *y*-direction), respectively, and the curb inlet was 4.57 m (15 ft) long in total. The type C inlet included a 1.52 m (5 ft) opening and 1.52 m (5 ft) upstream and downstream transition sections that change elevation or depression gradually from the undepressed section into the fully depressed inlet section over the 1.52 m (5 ft) length. The total width of the curb inlet depression was 0.457 m (1.5 ft) with a depressed depth of 0.010 m (0.33 ft) and a depression width of 0.368 m (1.2 ft) for the type C inlet (Fang et al., 2009; Guo, 2006).

The simulation domain was represented by a detailed and high-resolution DEM (Figure 4.3b) with a cell size equal to 0.076 m (0.25 ft). The elevation of every computation cell was calculated by considering the longitudinal slope, cross slope, local depressed slope of the curb inlet, and slopes of the inlet's upstream and downstream transition parts.

The Manning's law among the three friction choices (Manning's law, Darcy-Weisbach law, and Laminar law) in FullSWOF-ZG was used in the simulation, and the roughness coefficient determined for the laboratory roadway was 0.018, as reported by Hammonds and Holley (1995). The longitudinal (x-direction) and cross (y-direction) slopes for the simulation domain were from left to right and bottom to top, respectively (Figure 4.3).

The imposed discharge condition among five available boundary condition choices (imposed water height, wall condition, Neumann condition, periodic condition, and imposed discharge) in FullSWOF-ZG was chosen as the left or upstream boundary condition of the domain. The imposed discharge for the boundary cells within the spread (T) was approximately assumed as the total inflow rate (Q_i) divided by the number of the cells within the spread and was equal to 0 for other boundary cells outside of the spread. The top and right (downstream) boundary of the simulation domain were set as a Neumann condition that allows the flow to get out of the simulation domain. At the top of the simulation domain, those cells outside the curb inlet had higher elevations to prevent the outflow. The bottom boundary of the simulation domain (Figure 4.3b) had the highest elevation along the y-direction and was set as a wall boundary condition to guarantee that the flow would not pass through the bottom boundary.

4.2.3 Road-Bioretention Modeling Cases

Figure 4.4, as an example, shows the plan view and high-resolution DEM for the modeling case RBS04 (Table 4.1) with an undepressed curb inlet. Figure 4.4a includes the different parts of the RBS system: The road with longitudinal and cross slopes, the RBS, a curb inlet, a grate inlet on the road, an overflow grate inlet and a berm at the end of the RBS, and the curb separating the road and RBS. The RBS performance of ponding and infiltrating the runoff is affected by the longitudinal slope (S_0), cross slope (S_x), curb inlet interception efficiency (E_{ci}), bioretention depth (D_b), overflow height (h_b), and the RBS's soil infiltration parameters, such as the saturated hydraulic conductivity (K), suction head (φ), and moisture deficit ($\Delta\theta$). Different modeling cases were established to explore the influence of these design parameters on the RBS performance. Even when the RBS was flat in the y-direction with a lower elevation (i.e., bioretention depth, D_b) than the road surface, the RBS had the same length and longitudinal slope, S_0, in the x-direction as the road did (Figure 4.4).

There was a grate inlet at the end of the RBS where the grate inlet opening was h_b above the RBS ground surface. The elevation difference between the grate inlet opening and the RBS ground surface is called the overflow height, h_b, ranging from 0.25 m (10 in) to 0.45 m (18 in) in this study (Table 4.1). In the USA, the initial concept of bioretention has a shallow ponding depth of 0.15 m (6 in), but recent green infrastructure design manuals allow for 0.30 m (12 in) to 0.45 m (18 in) of ponding depth (Davis et al., 2009). Only when the water depths near the grate inlet are greater than h_b, will the runoff in RBS flow into the grate inlet then to the underground drainage pipe system. There is a berm at the end of the RBS (Figures 4.1 and 4.4) to pond the runoff inside the RBS, which facilitates

infiltration downward and possible overflow into the grate inlet. The berm height was set as the same as the bioretention depth, D_b, to prevent the longitudinal outflow from the RBS since $D_b > h_b$.

The simulation domain is divided into two zones by an imaginary dividing line (Figure 4.4a): The upstream or left of the line has uniform rainfall, and the downstream or right of the line has no rainfall. A part of the runoff generated on the road surface is intercepted by the curb inlet (Q_{ci} in Figure 4.4), then, a part of the bypass runoff from the inlet is captured by the grate inlet on the road (Q_{rg}) and leaves the simulated road surface through the grate inlet. Finally, the remainder of the runoff is discharged downstream along the road (Q_{bp}). The runoff into the bioretention infiltrates downward or overflows through the bioretention grate inlet (Q_{og}) when the ponding depth is greater than h_b.

The bioretention ponding volume (V_{pc}) was calculated for each modeling case in this study when the overflow occurred and did not consider the vegetation volume fraction of the bioretention facility. The impact of the longitudinal slope was included when calculating V_{pc} using the following Equation (4.9). The V_{pc} is calculated with two situations: (1) The ponding length is larger than the upstream catchment length, L ($L \times S_0 < h_b$); and (2) the ponding length is equal to or smaller than the upstream catchment length ($L \times S_0 \geq h_b$):

$$V_{pc} = \begin{cases} \left(L \times h_b - \dfrac{L^2 \times S_0}{2}\right) \times w_b - h_b \times A_{gr} & L \times S_0 < h_b \\ \dfrac{h_b}{S_0} \times \dfrac{h_b}{2} \times w_b - h_b \times A_{gr} & L \times S_0 \geq h_b \end{cases} \tag{4.9}$$

where V_{pc} (m^3) is the calculated ponding volume based on the RBS geometry; w_b (m) is the RBS width (1 m); L (m) is the RBS length, which is the same as the road length; S_0 is the

RBS's longitudinal slope; h_b (m) is the RBS overflow height; and A_{gr} (m^2) is the overflow grate inlet area.

Twenty cases of the RBS systems were modeled in this study by having four contributing-watershed lengths (10–40 m, 32.8–131.2 ft) and five longitudinal slopes (0.001–0.01) (Table 4.1). When the road length and longitudinal slope were increased, the cross slope and the curb-inlet length, L_{ci}, were also increased as real design situations for the curb inlet to intercept a similar amount of the runoff. When the contributing watershed was enlarged by increasing L, a longer L_{ci} allowed more runoff to flow into the RBS. Other corresponding RBS's parameter values were changed correspondingly as shown/summarized in Table 4.1. The RBS system has eight key modeling parameters, and to fully understand the RBS system performance and the influence from each parameter, a large number of modeling cases is required, which was not studied here. For all 20 cases (Table 4.1), the roadway width was 10 m (y-direction, Figure 4.4) for a two-lane road, including necessary space for shoulders and gutters (Chen, 2004). The curb width, which was the same as the curb-inlet width, was 0.1 m (4 in) to separate the road and the RBS. The RBS width was 1.0 m (40 in), and the maximum ponding depth or the bioretention depth, D_b, was set as 0.05 m above the grate-inlet overflow height, h_b, i.e., $D_b = h_b + 0.05$ m for all 20 modeling cases. The road grate inlet was a rectangle of 0.75 m (30 in, along with the x-direction) by 0.45 m (18 in) and was made to be 0.05 m (2 in) lower than the surrounding road-surface cells for the model simulation here. The grate inlet in the RBS was the same size for all modeling cases.

For the modeling case, RBS04 (Figure 4.4), the simulation domain length was 13 m (43 ft, x-direction), including 10 m (33 ft) of road surface before the inlet and a width of

10 m (33 ft), which was the curb-inlet runoff contributing watershed that received the rainfall (Figure 4.4). The computational cell/grid size for the simulation domain was 0.05 m (3 in) both in the *x*- and *y*- directions with a total of 57,200 cells for the case, RBS04. There was a total of 135 cells in each grate inlet [(0.75/0.05) × (0.45/0.05)] or k = 135 in Equation (4.7), and the curb inlet (L_{ci} = 0.45 m) was 18 cells [(0.45/0.05) × (0.1/0.05)] in the simulation domain of RBS04.

To compare the effect of different design parameters of the RBS systems, there were another 20 modeling cases (Rd01–Rd20) that had the same road surface without a curb inlet and RBS. Thus, all Rd modeling cases were the road only in the simulation domain. Each Rd modeling case was the same length (L), and longitudinal and cross slopes (S_0 and S_x) for the road surface as the corresponding RBS modeling case (Table 4.1).

All cell's elevations were calculated when the bottom left corner reference cell's elevation (the highest in the domain) was assumed to be 10 m as shown in Figure 4.4b. The road surface and bioretention ground elevations, therefore, vary with the longitudinal and cross slopes set for each modeling case (Table 4.1). All cells for the 0.1 m curb were set 0.2 m higher than the road surface cells. The cell's elevations inside the curb inlet cells were calculated using the same cross slope of the road surface, which helps and allows the runoff to flow into the RBS. The uniform rainfall intensity was 6.94×10^{-5} m/s (250 mm/h, 10 in/h) and lasted 1200 s (20 min) to generate enough runoff reach the ponding volume, but the total simulation period was 2400 s. A portion (virtual road-surface in Figure 4.4a) of the simulation domain just downstream of the curb inlet was simulated without rainfall because the focus of the study was to investigate the impact of the runoff generated upstream of the curb inlet.

Table 4.1. Parameter values of 20 modeling cases of the road-bioretention strip (RBS) systems with an undepressed curb inlet and grate inlets (Figure 4.4a).

Case No.	L (m)	S_0 (-)	S_x (-)	L_{ci} (m)	D_b (m)	K (mm/h)	φ (m)	$\Delta\theta$ (-)	V_{pc} (m^3)
RBS01	40	0.001	0.010	1.20	0.25	51	0.090	0.410	7.44
RBS02	30	0.001	0.015	0.90	0.30	25	0.218	0.435	7.33
RBS03	20	0.001	0.020	0.60	0.35	13	0.478	0.451	6.08
RBS04	10	0.001	0.030	0.45	0.45	51	0.090	0.410	4.28
RBS05	40	0.003	0.015	1.20	0.25	51	0.090	0.410	5.68
RBS06	30	0.003	0.020	0.90	0.30	25	0.218	0.435	6.33
RBS07	20	0.003	0.030	0.60	0.35	13	0.478	0.451	5.62
RBS08	10	0.003	0.040	0.45	0.45	51	0.090	0.410	4.16
RBS09 [1]	40	0.005	0.020	1.20	0.25	51	0.090	0.410	3.93
RBS10	30	0.005	0.030	0.90	0.30	25	0.218	0.435	5.32
RBS11	20	0.005	0.040	0.60	0.35	13	0.478	0.451	5.16
RBS12	10	0.005	0.045	0.45	0.45	51	0.090	0.410	4.03
RBS13 [1]	40	0.007	0.030	1.20	0.25	51	0.090	0.410	2.79
RBS14	30	0.007	0.040	0.90	0.30	25	0.218	0.435	4.32
RBS15	20	0.007	0.045	0.60	0.35	13	0.478	0.451	4.71
RBS16	10	0.007	0.055	0.45	0.45	51	0.090	0.410	3.91
RBS17 [1]	40	0.010	0.040	1.20	0.25	51	0.090	0.410	1.93
RBS18 [1]	30	0.010	0.045	0.90	0.30	25	0.218	0.435	3.04
RBS19	20	0.010	0.055	0.60	0.35	13	0.478	0.451	4.02
RBS20	10	0.010	0.065	0.45	0.45	51	0.090	0.410	3.72

Note: [1]—for the modeling case, $L \times S_0 \geq h_b$ Equation (4.9). L (m) is the length of the road and the RBS upstream of the curb inlet (Figure 4.4), L_{ci} (m) is the opening length of the curb inlet, h_b (m) is the overflow height of the grate inlet inside the RBS, and the bioretention depth, $D_b = h_b + 0.05$ m, K (mm/h) is the saturated hydraulic conductivity, φ (m) is the soil suction head, and $\Delta\theta$ is the soil moisture deficit, V_{pc} (m^3) is the calculated bioretention ponding volume when overflow occurs.

4.3 Results and Discussion

4.3.1 FullSWOF-ZG Testing Results

In a previous study (Li et al., 2018b), FullSWOF_2D was updated and tested with published rainfall-runoff data on pervious surfaces adopted from Esteves's study (Esteves et al., 2000). It showed that the updated program provided consistent simulation results with observed data during the whole rainfall period. The details of the testing results for FullSWOF-ZG for pervious surfaces with data collected in Texas A&M University and type C curb inlet cases with data from the published report are introduced below.

4.3.1.1 Results for Pervious Surfaces

The comparison of observed and simulated discharge hydrographs of one pervious surface under four rainfall events is shown in Figure 4.5. The simulated hydrographs closely follow with the observed hydrographs for the sample results. The discharge NSE values ranged from 0.79 to 0.93 (Table 4.2, average $\pm$ standard deviation as 0.86 $\pm$ 0.05) for three pervious surfaces (slopes) under eight rainfall events. Table 4.2 also presents the comparison results of the simulated and observed runoff volume and peak discharges. The percent differences of the simulated runoff volume and peak discharges were 2.8 $\pm$ 13.3% (average $\pm$ standard deviation) and 13.8 $\pm$ 12.8%, respectively. Figure 4.5a is the case with the highest runoff-volume percent difference, and Figure 4.5c is the case with the second highest peak-discharge percent difference. The indoor testing bed was 0.36 m deep, which was much larger than the cumulative infiltration depth during the experiment. The indoor testing bed was deep and provided enough soil space for the infiltrated runoff. The results for all eight rainfall events (Table 4.2 and Figure 4.5) show that the FullSWOF-ZG

program predicted the rainfall-runoff process of overland flows on a pervious surface with reasonable accuracy.

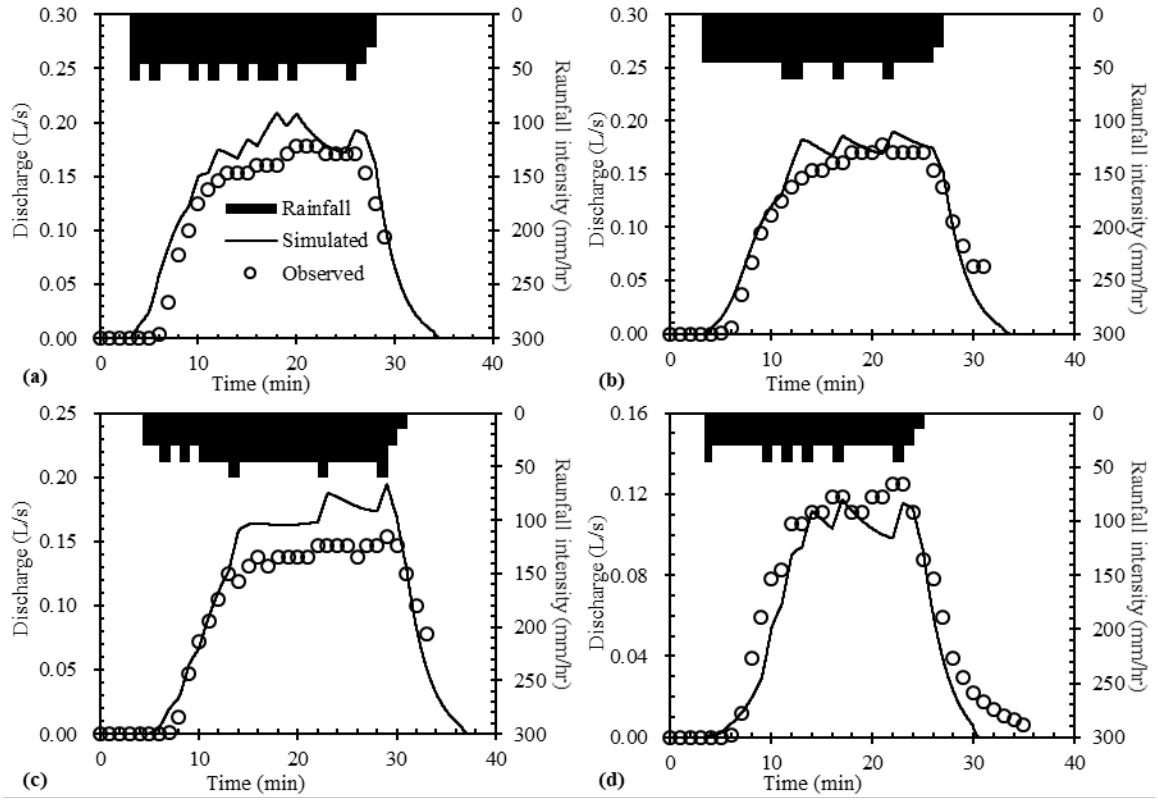

Figure 4.5. Simulated and observed hydrographs of one pervious surface under four events: (**a**) S01R1, (**b**) S01R2, (**c**) S01R3, and (**d**) S01R4 (Table 4.2).

Table 4.2. Comparison of simulated and observed discharge and volume results for eight rainfall events.

Events	S_0 (-)	NSE (-)	V_r (m^3)	V_{ob} (m^3)	V_{si} (m^3)	ΔV_p (%)	Q_{po} (L/s)	Q_{ps} (L/s)	ΔQ_p (%)
S01R1	0.001	0.85	0.35	0.20	0.25	22.2	0.18	0.21	15.4
S01R2	0.001	0.93	0.32	0.20	0.21	4.9	0.18	0.19	5.4
S01R3	0.001	0.83	0.32	0.19	0.22	14.6	0.15	0.19	23.5
S01R4	0.001	0.92	0.20	0.13	0.11	−16.7	0.12	0.12	0.0
S02R5	0.002	0.83	0.21	0.12	0.12	0.0	0.12	0.15	22.2
S02R6	0.002	0.84	0.27	0.15	0.15	0.0	0.12	0.15	22.2
S02R7	0.002	0.79	0.25	0.16	0.14	−13.3	0.15	0.14	−6.9
S05R8	0.005	0.87	0.19	0.09	0.10	10.5	0.12	0.16	28.6

Note: S_0 (-) is the testing bed's surface slope, V_r (m^3) is the calculated rainfall volume, V_{ob} (m^3) is the observed total runoff volume, V_{si} (m^3) is the simulated total runoff volume, ΔV_p (%) is the percent difference of the simulated runoff volume = $(V_{si} - V_{ob})/[(V_{ob} + V_{si})/2] \times 100\%$, Q_{po} (L/s) is the observed peak runoff rate, Q_{ps} (L/s) is the simulated peak runoff rate, ΔQ_p (%) is the percent difference of the simulated peak discharge = $(Q_{ps} - Q_{po})/[(Q_{po} + Q_{ps})/2] \times 100\%$.

4.3.1.2 Results of Curb Inlet Interception

Twenty modeling cases for the type C inlet on the road surfaces (Table 4.3) covered six longitudinal slopes (0.004–0.07), two cross slopes (0.0208 and 0.0407), and 12 spreads (2.16–4.27 m), and 20 upstream inflows (Q_{in} 0.1031–0.2453 m^3/s). All these model input parameter values were exactly the same as the experimental setup information (Fang et al., 2009; Mark Alan Hammonds and Edward R. Holley, 1995). The curb inlet interception efficiency (E_{ci}) was evaluated with the curb intercepted flow rate (observed Q_{cio} or simulated Q_{cis}) divided by the upstream inflow rate (Q_{in}) after the system reached equilibrium.

Table 4.3 shows that the simulated intercepted flows and inlet efficiencies of type C curb inlets on the road surfaces with different longitudinal and cross slopes have great consistency with the observed results from the laboratory experiments conducted by Hammonds and Holley (1995). The coefficient of determination (R^2) of the linear relationship between the simulated and observed curb inlet interception efficiencies was 0.94. The high R^2 value with lower differences (ΔE) is evidence to support that the FullSWOF-ZG model, which predicted the curb inlet interception efficiency with good performance.

The differences between the simulated and observed interception efficiencies (ΔE) ranged from −3.2% to 13.2%, with an average ± standard deviation of 3.5 ± 3.5%. The percent differences (PD_E) of the simulated and observed intercepted efficiencies ranged from −6.0% to 28.7%, with an average ± standard deviation of 6.6 ± 7.3%. In a previous study by Fang et al. (2009), a three-dimensional fluid simulation software, FLOW-3D, was applied to simulate complex 3D shallow flow over the drainage pavement and flow leaving through type C and type D inlets. The differences (ΔE) ranged from −7.0% to 17.6%, with an average ± standard deviation of 1.0 ± 4.87% for type C cases in their 3D simulations. The percent differences (PD_E) for Fang's study ranged from −19.7% to 6.1%, with an average ± standard deviation of −0.8 ± 5.7%. These 2D SWEs models using the FullSWOF-ZG program were almost as good as the FLOW-3D models used in the previous study when trying to simulate the interception efficiency of the type C curb inlet under different operation conditions. The results for all 20 modeling cases (Table 4.3) showed that the FullSWOF-ZG program was not only able to simulate the complicated flow over type C curb inlets but also predicted the curb inlet interception efficiency well.

Table 4.3. Curb inlet test cases' setting parameters and simulation results.

Case No.	S_0 (-)	S_x (-)	T (m)	Q_{in} (m^3/s)	Q_{cio} (m^3/s)	E_{cio} (%)	Q_{cis} (m^3/s)	E_{cis} (%)	ΔE (%)	PD_E (%)
C01	0.004	0.0208 (1:48)	4.27	0.2400	0.1256	52.3	0.1306	54.4	2.1	3.9
C02	0.004	0.0208	4.27	0.1076	0.0829	77.0	0.0872	81.0	4.0	5.0
C03	0.010	0.0208	4.27	0.2361	0.1098	46.5	0.1185	50.2	3.7	7.7
C04	0.010	0.0208	4.27	0.1806	0.0983	54.4	0.1047	58.0	3.5	6.3
C05	0.020	0.0208	3.45	0.1246	0.0741	59.5	0.0793	63.6	4.2	6.8
C06	0.020	0.0208	4.27	0.2424	0.0979	40.4	0.1139	47.0	6.6	15.1
C07	0.040	0.0208	4.07	0.1281	0.0698	54.5	0.0734	57.3	2.8	5.1
C08	0.040	0.0208	4.07	0.1589	0.0762	48.0	0.0823	51.8	3.8	7.7
C09	0.060	0.0208	4.07	0.1166	0.0653	56.0	0.0615	52.8	−3.2	−6.0
C10	0.060	0.0208	4.27	0.2451	0.0853	34.8	0.0896	36.6	1.8	4.9
C11	0.004	0.0417 (1:24)	3.87	0.2316	0.1488	64.2	0.1539	66.4	2.2	3.4
C12	0.004	0.0417	3.21	0.1439	0.1182	82.1	0.1194	83.0	0.8	1.0
C13	0.010	0.0417	2.84	0.1433	0.1133	79.1	0.1145	79.9	0.9	1.1
C14	0.010	0.0417	3.37	0.2320	0.1369	59.0	0.1436	61.9	2.9	4.8
C15	0.020	0.0417	2.97	0.2433	0.1215	49.9	0.1359	55.9	5.9	11.2
C16	0.020	0.0417	2.28	0.1031	0.0870	84.4	0.0886	86.0	1.6	1.9
C17	0.050	0.0417	2.16	0.1724	0.0874	50.7	0.0983	57.0	6.3	11.7
C18	0.050	0.0417	3.09	0.2381	0.0940	39.5	0.1255	52.7	13.2	28.7
C19	0.070	0.0208	4.07	0.1542	0.0700	45.4	0.0682	44.2	−1.2	−2.6
C20	0.070	0.0417	3.05	0.1535	0.0803	52.3	0.0927	60.4	8.1	14.3

Note: S_0 (-) is the road longitudinal slope, S_x (-) is the road cross slope, T (m) is the upstream flow spread width, Q_{in} (m^3/s) is the upstream inflow rate, Q_{cio} (m^3/s) is the observed curb inlet intercepted flow rate, E_{cio} (%) is the observed curb inlet intercepted efficiency, Q_{cis} (m^3/s) is the simulated curb inlet intercepted flow rate, E_{cis} (%) is the simulated curb inlet intercepted efficiency, ΔE (%) is the difference of the simulated intercepted efficiency = $E_{cis} - E_{cio}$, PD_E (%) is the percent difference of the simulated intercepted efficiency = $(E_{cis} - E_{cio})/[(E_{cis} + E_{cio})/2] \times 100\%$.

4.3.2 Results of Rd and RBS Modeling Cases

4.3.2.1 Example Modeling Results

As an example of modeling results for the RBS systems, the performance of the case, RBS19, was first evaluated and compared with the modeling case, Rd19, that has no curb inlet. Figure 4.6 shows the simulated hydrographs for the Rd19 and RBS19 cases, the ponding depth in the RBS, infiltration rate, and cumulative infiltration depth for the RBS19 case (Table 4.1). A summary of the results for all modeling cases for the road-only and the RBS is given in Tables 4.4 and 4.5, respectively. Figure 4.6a shows the rainfall intensity over 20 min, hydrographs of the bypass flow (Q_{bp}), and the flow into the road grate inlet (Q_{rg}) of the 30 min simulation period. The runoff generated from the road surface took 32 s to reach the grate inlet, the discharge into the grate inlet then increased rapidly to a 98% peak in 85 sec, and reached the equilibrium discharge of 11.96 L/s at 180 sec under the constant rainfall. The grate inlet discharge took about 300 sec to decrease to 0 L/s after the rainfall stopped. The rest part of the overland runoff that was not captured by the grate inlet discharges to the downstream as the bypass flow, which had a peak discharge of 1.91 L/s at 91 sec. The sum of the peak flows of Q_{rg} and Q_{bp} was 13.87 L/s, which was the same as the peak discharge from the rational formula.

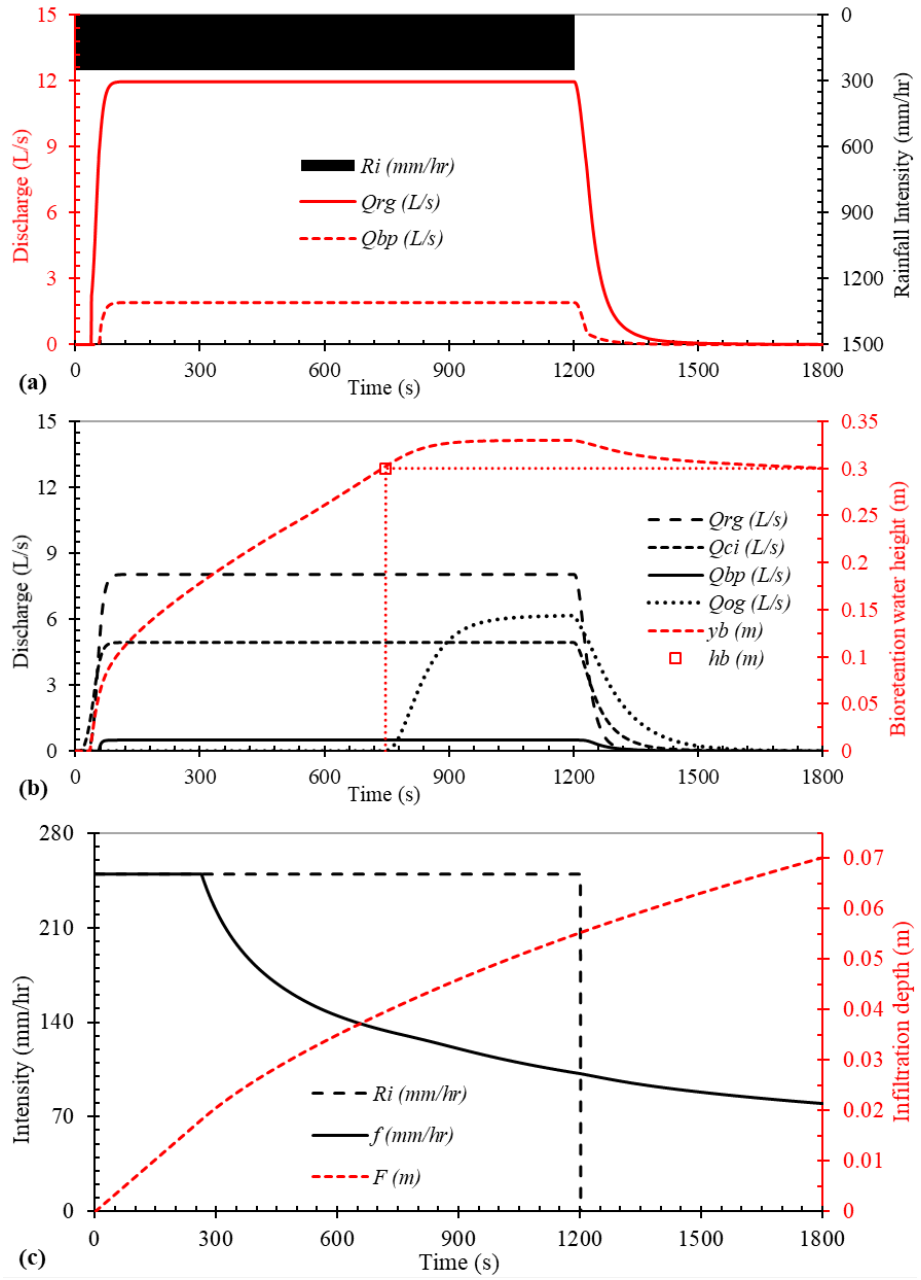

Figure 4.6. Simulation results of case Rd19 (**a**) and case RBS19 with an undepressed curb inlet (**b**,**c**). All symbols are defined in the text and summarized in Appendix A.

In comparison, Figure 4.6b shows simulated hydrographs for Q_{rg}, Q_{bp}, the curb inlet intercepted flow (Q_{ci}), and the overflow from the grate inlet in bioretention (Q_{og}) as well as the bioretention water depth (y_b) of the modeling case, RBS19. The peak or equilibrium

discharges of Q_{rg}, Q_{ci}, and Q_{bp} were 8.03 L/s, 4.94 L/s, and 0.50 L/s, respectively. The flow interception by the curb inlet seemed to slow down the flow a little bit to make more runoff into the grate inlet. Therefore, the sum of the peak Q_{rg} and Q_{ci} for RBS 19 was 12.97 L/s, which was larger than the Q_{rg} of 11.96 L/s for the Rd19 case.

Under a rainfall event, the interception efficiency, E_{ci}, of a curb inlet is not constant, but changes with time. For RBS19, the runoff first reached the curb inlet at 11 sec, and E_{ci} was 100% when the runoff rate was small at 11 sec < t < 31 sec, then E_{ci} decreased with time and became 36.7% when Q_{ci} reached the equilibrium discharge. At the end of the 40-min simulation, the runoff volume, intercepted by the curb inlet and generated from the road, can be computed and the volumetric interception efficiency was computed as 37.4% for the RBS19 case, which will be further discussed later using Table 4.5. Therefore, for RBS19, the grate inlet on the road still intercepted a large percent (~60%) of the incoming runoff, and only about 2.6% of the runoff volume was bypassed downstream. This is important information to the road and bioretention design since many designers think the curb inlet can intercept all runoff and adding or keeping the grate inlet on the road is not necessary. Figure 4.6 also shows that the geometry of the experiment and the model allowed for a fully developed flow by the time the flow reached the inlet. This was true for all modeling cases.

Under 250 mm/h rainfall over 20 min, the bioretention overflow Q_{og} started at 748 sec, reached the peak discharge of 6.16 L/s (at the 1200 sec), and decreased after the rainfall stopped (Figure 4.6b). The red dash line in Figure 4.6b shows that the ponding depth (y_b) adjacent to the bioretention overflow grate inlet increased to become higher than the bioretention overflow height (h_b = 0.3 m) at 748 sec and decreased to 0.3 m slowly after

the rainfall stopped. There was a time period when Q_{og} was larger than Q_{ci}, which seemed impossible in the first impression. This was because the grate inlet discharge capacity was usually higher than the curb inlet capacity. In this study, the corresponding overflow weir length of the grate inlet [2 × (0.45 + 0.75) m] was much larger than the curb inlet opening (0.6 m), and the hydraulic head above the grate inlet could be larger also. It was verified that the mass conservation of the runoff in the simulation domain was valid (Figure 4.6) and the simulated larger Q_{og} was correct.

Figure 4.6c shows the bioretention infiltration rate (f) and cumulative infiltration (F) over time. The infiltration rate was calculated using the Green-Ampt method in FullSWOF-ZG, which considers the soil infiltration parameters, runoff ponding depth, and rainfall intensity (R_i) at every time step. The bioretention infiltration rate was equal to the rainfall intensity, R_i, when the calculated soil infiltration capacity was larger than R_i. The infiltration rate started to decrease at 263 sec and decreased to 80.1 mm/h at the end of the simulation. The cumulative infiltration, F, kept increasing during the simulation period and reached 0.07 m at 30 min, which seemed small, but the infiltration continued at ~80 mm/h to gradually deplete all ponding water in the bioretention cell. The heavy rainfall (250 mm/h) over 20 min was used for the simulation to generate the overflow in the grate inlet at the RBS so that FullSWOF-ZG was fully tested.

Table 4.4. Summary of simulation results of 20 road-only modeling cases (grouped by inlet length *L*).

Case No.	V_{rd} (m^3)	V_{srd} (m^3)	ΔV_{rd} (%)	V_{rg} (m^3)	P_{rg} (%)	V_{bp} (m^3)	P_{bp} (%)	Q_{prg} (L/s)	Q_{pbp} (L/s)
Rd04 (10 m) [1]	8.33	8.24	−1.02	8.10	98.3	0.14	1.7	6.81	0.13
Rd08	8.33	8.30	−0.34	8.16	98.3	0.14	1.7	6.82	0.12
Rd12	8.33	8.31	−0.21	8.06	97.0	0.25	3.0	6.74	0.20
Rd16	8.33	8.31	−0.17	7.92	95.3	0.39	4.7	6.62	0.32
Rd20	8.33	8.31	−0.18	7.67	92.3	0.64	7.7	6.42	0.52
Rd03 (20 m)	16.66	16.45	−1.25	14.85	90.3	1.60	9.7	12.43	1.45
Rd07	16.66	16.60	−0.33	13.10	78.9	3.50	21.1	10.80	3.08
Rd11	16.66	16.63	−0.17	13.81	83.0	2.82	17.0	11.43	2.45
Rd15	16.66	16.63	−0.13	14.05	84.5	2.58	15.5	11.66	2.22
Rd19	16.66	16.64	−0.11	14.39	86.5	2.25	13.5	11.97	1.91
Rd02 (30 m)	24.98	24.49	−2.00	21.52	87.9	2.97	12.1	18.01	2.81
Rd06	24.98	24.84	−0.58	19.98	80.4	4.86	19.6	16.55	4.27
Rd10	24.98	24.92	−0.24	17.00	68.2	7.93	31.8	13.94	6.88
Rd14	24.98	24.95	−0.13	18.50	74.1	6.45	25.9	15.25	5.57
Rd18	24.98	24.96	−0.10	19.18	76.8	5.78	23.2	15.86	4.96
Rd01 (40 m)	33.31	32.22	−3.28	22.85	70.9	9.37	29.1	19.02	8.73
Rd05	33.31	33.02	−0.88	21.87	66.2	11.15	33.8	17.97	9.79
Rd09	33.31	33.16	−0.44	17.71	53.4	15.45	46.6	14.38	13.38
Rd13	33.31	33.24	−0.22	20.61	62.0	12.62	38.0	16.87	10.89
Rd17	33.31	33.27	−0.13	22.96	69.0	10.31	31.0	18.89	8.87

Note: [1]—the road length, *L*, is given in brackets and there is the same length for other modeling cases in the same group, V_{rd} (m^3) is the total rainfall volume fell on the road surface, V_{rg} (m^3) is the runoff volume captured by the road grate inlet, V_{bp} (m^3) is the bypass runoff volume (to the road downstream), P_{rg} (%) is the percent of runoff captured by the grate inlet = $V_{rg}/(V_{rg} + V_{bp}) = V_{rg}/V_{srd}$, P_{bp} (%) is the percent of the bypass runoff = V_{bp}/V_{srd}, ΔV_{rd} (%) is the percent difference of the simulated runoff volume = $(V_{srd} - V_{rd})/V_{rd} \times 100\%$, Q_{prg} (L/s) is the peak discharge of the runoff captured by the road grade inlet, Q_{pbp} (L/s) is the peak discharge of the bypass runoff.

Table 4.5. Simulation results of road-bioretention cases (grouped by L).

Case No.	V_{ci} (m^3)	P_{ci} (%)	V_{rg} (m^3)	P_{rg} (%)	V_{bp} (m^3)	P_{bp} (%)	V_{rb} (m^3)	V_{inf} (m^3)	V_{bog} (m^3)	V_{bio} (m^3)	ΔV (%)	ΔV_{rd} (%)	ΔV_{rb} (%)
RBS04 (10 m) [1]	3.30	40.8	4.76	58.9	0.02	0.3	0.83	1.24	0.00	3.13	0.0	−2.9	5.8
RBS08	3.33	41.2	4.64	57.5	0.10	1.3	0.83	1.25	0.00	3.16	0.0	−3.0	5.9
RBS12	3.22	39.9	4.62	57.2	0.23	2.9	0.83	1.24	0.00	3.06	0.0	−3.0	6.1
RBS16	3.27	40.5	4.42	54.7	0.39	4.8	0.83	1.25	0.00	3.10	0.0	−3.0	5.9
RBS20	3.21	39.8	4.22	52.3	0.64	8.0	0.83	1.24	0.00	3.05	0.0	−3.0	6.0
RBS03 (20 m)	5.61	34.6	10.00	61.7	0.60	3.7	1.67	1.63	0.26	5.83	0.0	−2.7	6.1
RBS07	5.85	36.1	9.89	61.1	0.44	2.7	1.67	1.63	1.03	5.33	0.0	−2.8	6.3
RBS11	6.09	37.7	9.76	60.4	0.32	2.0	1.67	1.62	1.73	4.89	0.0	−2.9	6.3
RBS15	5.99	37.1	9.76	60.4	0.41	2.6	1.67	1.61	2.09	4.45	0.0	−3.0	6.4
RBS19	6.04	37.4	9.50	58.8	0.61	3.8	1.67	1.58	2.82	3.80	0.0	−3.0	6.5
RBS02 (30 m)	9.24	38.0	14.28	58.7	0.80	3.3	2.50	2.70	2.66	7.03	0.0	−2.6	5.5
RBS06	9.13	37.5	13.61	56.0	1.59	6.5	2.50	2.65	3.72	5.91	0.0	−2.6	5.6
RBS10	10.05	41.4	12.57	51.7	1.68	6.9	2.50	2.60	5.69	4.94	0.0	−2.7	5.4
RBS14	10.78	44.4	12.59	51.8	0.92	3.8	2.50	2.54	7.45	3.98	0.0	−2.8	5.2
RBS18	10.49	43.2	12.89	53.1	0.89	3.7	2.50	2.30	8.60	2.80	0.0	−2.8	5.4
RBS01 (40 m)	12.18	37.5	16.87	52.0	3.40	10.5	3.33	4.28	5.01	7.06	−0.1	−2.6	5.4
RBS05	12.47	38.4	15.81	48.7	4.19	12.9	3.33	4.12	7.45	5.07	0.0	−2.5	5.2
RBS09	12.96	39.9	15.64	48.2	3.87	11.9	3.33	3.85	9.85	3.43	0.0	−2.5	5.1
RBS13	14.75	45.4	14.34	44.2	3.37	10.4	3.33	3.42	13.09	2.42	0.0	−2.6	4.7
RBS17	15.72	48.4	14.67	45.2	2.06	6.3	3.33	3.09	15.14	1.68	0.0	−2.6	4.5

Note: [1]—the road length, L, is given in brackets and there is the same length for other modeling cases in the same group, V_{ci} (m^3) is the runoff volume intercepted by the curb inlet, V_{rg} (m^3) is the runoff volume captured by the road grate inlet, V_{bp} (m^3) is the bypass runoff volume, P_{ci} (%) is the percentage of the total runoff volume that is intercepted by the curb inlet (V_{ci}/V_{rd}), P_{rg} (%) is the road grate inlet captured runoff percentage, P_{bp} (%) is the road end bypass runoff percentage, V_{rb} (m^3) is the runoff generated on the bioretention surface from the rainfall, V_{inf} (m^3) is the bioretention infiltrated runoff volume, V_{bog} (m^3) is the bioretention overflow grate inlet discharge volume, V_{bio} (m^3) is the runoff ponded in bioretention at the end of the simulation, ΔV (%) is the runoff volume percent difference of the whole simulation domain = $(V_{rg} + V_{bp} + V_{inf} + V_{bog} + V_{bio} - V_{rd} - V_{rb})/(V_{rd} + V_{rb}) \times 100\%$, ΔV_{rd} (%) is the runoff volume percent difference of the road surface = $(V_{ci} + V_{bp} + V_{rg} - V_{rd})/V_{rd} \times 100\%$, ΔV_{rb} (%) is the runoff volume percent difference of the bioretention cell = $(V_{inf} + V_{bog} + V_{bio} - V_{ci} - V_{rb})/(V_{ci} + V_{rb}) \times 100\%$, P_{inf} (%) is the infiltrated runoff percentage = $V_{inf}/(V_{ci} + V_{rb}) \times 100\%$.

4.3.2.2 Modeling Results for Road-Only (Rd) Cases

Modeling results for 20 road-only cases are first presented in Figure 4.7a and summarized in Table 4.4 to compare them with modeling results for the road-bioretention cases (Figure 4.7b, Table 4.5, and Table 4.6) in the next section. For the road-only cases, the rainfall volume, V_{rd}, was transformed into the runoff volume captured by the road grate inlet (V_{rg}) and the bypass runoff volume (V_{bp}). The percent differences (ΔV_{rd}) between the simulated runoff volume, $V_{srd} = V_{rg} + V_{bp}$, and the rainfall volume V_{rd} for 20 road-only cases ranged from −3.3% to 0.1%. The average ± standard deviation of ΔV_{rd} was −0.6 ± 0.8% for 20 road-only cases (Table 4.4), which indicated FullSWOF-ZG had a higher accuracy in mass balance. These 20 modeling cases were regrouped into five groups (by alternating two colors in Table 4.4): The road length L decreased from 40 m to 10 m as the modeling case number increased when S_o is the same in each group (Table 4.1). Since the same rainfall was used for all modeling cases, all runoff volumes decreased with the decrease of the road length (Table 4.4), e.g., V_{rg} decreased from 22.96 m^3 (Rd17, L = 40 m) to 7.67 m^3 (Rd20, L = 10 m); and the corresponding V_{bp} decreased from 10.31 m^3 to 0.64 m^3. Because of the volume decrease or less flow velocity due to less L, the percent of V_{rg} ($P_{rg} = V_{rg}/V_{srd}$) increased with the additional influence of the increase of the cross slope, e.g., Rd01–Rd04 from 70.9% to 98.3% (Figure 4.7a). The percent of V_{rg} ranged from 53.4% (Rd09, S_x = 2%) to 98.3% (Rd08, S_x = 4%), with an average ± standard deviation of 80.7 ± 21.5%. The percent of V_{bp} ($P_{bp} = V_{bp}/V_{srd}$) ranged from 1.7% (Rd08) to 46.6% (Rd09), with an average ± standard deviation of 19.3 ± 13.0%. The relatively large variations of P_{rg} and P_{bp} were due to the change of the road length or upstream inflow.

If sorting the modeling cases by the road length, L (Table 4.4), the average P_{rg} for the same L cases decreased from 96.2% to 64.3% for L increases from 10 to 40 m, but the standard deviation from the mean increased from 2.5% to 7.0%. Therefore, L had more influence on P_{rg} than S_o did. When L was smaller, the incoming runoff from the upstream road was small, more runoff as intercepted by the grate inlet, and less runoff was bypassed downstream. Only 20 individual road-only cases (4 L × 5 S_o) were modeled here; when S_o was increased, the cross slope, S_x, was also increased to allow and guide more runoff to the grate inlet. S_x ranged from 3.0%–6.5% at L = 10 m to 1.0%–4.0% at L = 40 m (Table 4.1). For Rd09, both V_{bp} and P_{bp} were the highest and indicated a high potential of the local flooding on the road. For all road-only cases, the peak discharges of the grate inlet (Q_{prg}) were 6.68 $\pm$ 0.17 L/s for the L = 10 m group, 11.66 $\pm$ 0.61 L/s for the L = 20 m group, 15.92 $\pm$ 1.51 L/s for the L = 30 m group, and 17.43 $\pm$ 1.91 L/s for the L = 40 m group. The peak discharges of the bypass flow (Q_{pbp}) were 0.26 $\pm$ 0.17 L/s for the L = 10 m group, 2.22 $\pm$ 0.61 L/s for the L = 20 m group, 4.90 $\pm$ 1.51 L/s for the L = 30 m group, and 10.33 $\pm$ 1.91 L/s for the L = 40 m group. Both Q_{prg} and Q_{pbp} increased with the increase of the catchment length.

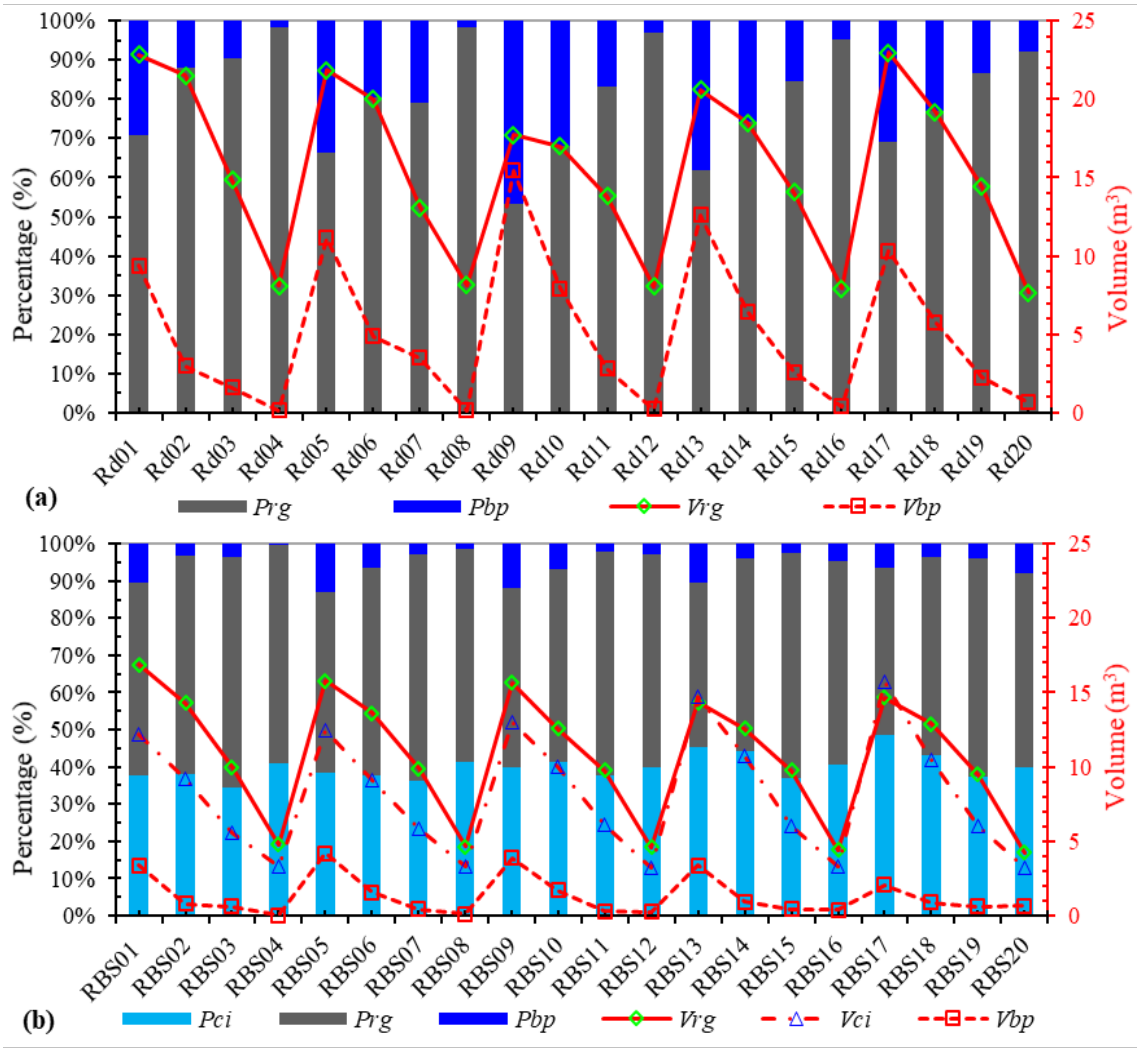

Figure 4.7. Runoff volumes and corresponding percentages captured by the road grate inlet (V_{rg} and P_{rg}), bypassed downstream (V_{bp} and P_{bp}) for **(a)** 20 road-only (Rd01–Rd20) and **(b)** 20 RBS modeling cases, and **(b)** intercepted by the curb inlet (V_{ci} and P_{ci}) for RBS modeling cases. Percentages are shown as a 100% stacked column diagram using a major *y*-axis and volumes (m^3) are shown as lines with symbols using a secondary *y*-axis.

Table 4.6. Mean and standard deviation (numbers inside brackets) of parameters calculated from each of the five road-bioretention cases with the same L (10 m–40 m).

Length (L)	V_{ci} (m^3)	P_{ci} (%)	V_{rg} (m^3)	P_{rg} (%)	V_{bp} (m^3)	P_{bp} (%)	V_{rb} (m^3)	V_{inf} (m^3)	V_{bog} (m^3)	V_{bio} (m^3)
10 m RBS [1]	3.27	40.5	4.53	56.1	0.28	3.4	0.83	1.24	0.00	3.10
	(0.05)	(0.6)	(0.21)	(2.6)	(0.25)	(3.1)	(0.00)	(0.00)	(0.00)	(0.05)
20 m RBS [2]	5.91	36.6	9.78	60.5	0.48	2.95	1.67	1.61	1.59	4.86
	(0.19)	(1.2)	(0.18)	(1.1)	(0.12)	(0.8)	(0.00)	(0.02)	(0.98)	(0.78)
30 m RBS [3]	9.94	40.9	13.19	54.3	1.17	4.8	2.50	2.56	5.62	4.93
	(0.74)	(3.07)	(0.74)	(3.0)	(0.42)	(1.7)	(0.00)	(0.16)	(2.48)	(1.65)
40 m RBS [4]	13.62	42.0	15.46	47.6	3.38	10.4	3.33	3.75	10.11	3.93
	(1.54)	(4.76)	(1.00)	(3.1)	(0.81)	(2.5)	(0.00)	(0.50)	(4.10)	(2.16)

Note: [1] for RBS04, 08, 12, 16, and 20; [2] for RBS03, 07, 11, 15, and 19; [3] for RBS02, 06, 10, 14, and 18; and [4] for RBS01, 05, 09, 13, and 17.

4.3.2.3 Modeling Results for Road-Bioretention Strip (RBS) Cases

1. Mass Balance on the Road with a Curb Inlet

First, we studied the mass (i.e., runoff volume) balance or redistribution on the road with a curb inlet for the RBS, which was compared with the road-only cases. Results are summarized in columns 2 to 7 in Table 4.5 and plotted on Figure 4.7b. For the corresponding 20 bioretention modeling cases (Figure 4.7b), a part of the road runoff (V_{srd}) was intercepted by the curb inlet (V_{ci}), resulting in a reduction of the runoff incepted by the road grate inlet (V_{rg}) and bypass runoff (V_{bp}). For the 20 RBS cases (Table 4.5), V_{ci} increased from 3.27 $\pm$ 0.05 m^3 (L = 10 m) to 13.6 $\pm$ 1.54 m^3 (L = 40 m) (Table 4.6), but the percentage ($P_{ci} = V_{ci}/V_{srd} = V_{ci}/(V_{ci} + V_{rg} + V_{bp})$) of runoff volume intercepted by the curb inlet (or curb inlet efficiency by volume) was similar: 40.0 $\pm$ 3.3%. This was because

the curb inlet length, L_{ci}, was also increased from 0.45 m to 1.2 m for L = 10–40 m. The corresponding runoff volume (V_{rg}) captured by the road grate inlet increased from 4.53 ± 0.21 m^3 (L = 10 m) to 15.46 ± 1.00 m^3 (L = 40 m); the bypass runoff volume (V_{bp}) from 0.28 ± 0.25 m^3 to 3.38 ± 0.81 m^3. The percentage of the runoff captured by the grate inlet on the road ($P_{rg} = V_{rg}/V_{srd}$) decreased from 56.1 ± 2.6% (L = 10 m) to 47.6 ± 3.1% (L = 40 m), with an overall average ± standard deviation of 54.6 ± 5.2%. Due to the curb inlet interception, each RBS system diverted a part of the runoff from the impervious road to the bioretention strip for infiltration and treatment (e.g., to allow sediments to settle and improve water quality). Therefore, less runoff flowed into the grate inlet on the road, and then the P_{rg} for the RBS (Table 4.5) was always smaller than for the corresponding road-only case (Table 4.4). The differences of P_{rg} between the road-only and corresponding RBS modeling cases ranged from 5.2%–40.8%, with an average difference of 26.0 ± 9.6%.

For all RBS cases under 250 mm/h rainfall, the road surface runoff was not 100% intercepted by the curb inlet, which indicated that the curb inlet was the bottleneck of the RBS system and impeded the runoff flowing into the bioretention strip for detention and infiltration to improve the stormwater quality. Therefore, the grate inlet was necessary to capture the road surface runoff and discharge into an underground drainage pipe to relieve road local flood inundation and ensure traffic safety. The bypass runoff percentage, P_{bp}, for the RBS cases (Figure 4.7 and Table 4.5) ranged from 0.3% (RBS04) to 12.9% (RBS05), with an average ± standard deviation of 5.4 ± 3.6%. The V_{bp} and P_{bp} for all RBS cases (Table 4.5) were lower than them for the corresponding road-only cases (Table 4.4), which means the curb inlet and grate inlet combination was more efficient than the grate inlet only for intercepting the road surface runoff. The mass balance as percent differences of

the whole simulation domain (ΔV), on the road (ΔV_{rd}) and in the bioretention strip (ΔV_{rb}), were small (Table 4.5).

2. Mass Balance in the Bioretention Strip

The mass (i.e., runoff volume) balance or redistribution in the bioretention strip are summarized in columns 8 to 11 in Table 4.5. For RBS systems, the inflow to the bioretention strip included the runoff intercepted by the curb inlet (V_{ci}) and generated on the bioretention surface from rainfall (V_{rb}). The bioretention outflow included the infiltration (V_{inf}) and the overflow through the grate inlet near the check dam (Figure 4.1, V_{bog} in Table 4.5). The difference between the inflow and the outflow was the ponding volume (V_{bio}) in the bioretention strip. V_{rb} was the rainfall depth (250 mm/h × 20 min) times the area (L × 1 m) of the bioretention strip and linearly increased from 0.83 m^3 to 3.33 m^3 for L = 10 m to 40 m.

The cumulative infiltration volume of bioretention (V_{inf}) was calculated (Table 4.5), and the mean V_{inf} ranged from 1.24 m^3 for the L = 10 m group to 3.75 m^3 for the L = 40 m group over 40 min simulation periods. To understand the soil infiltration performance of the bioretention, loamy sand was used for the L of 10 m and 40 m cases, sandy loam for L of 20 m cases, and loam for L of 30 m cases. The average and standard deviation of the infiltrated runoff percentage, i.e., $V_{inf}/(V_{ci} + V_{rb})$, were 30.4 ± 0.3% for loamy sand (L = 10 m group), 21.3 ± 0.8% for sandy loam (L = 20 m group), 20.7 ± 6.5% for loam (L = 30 m group), and 22.5 ± 8.5% for loamy sand (L = 40 m group).

The infiltration in the bioretention cell is influenced by the runoff inflow, the soil infiltration capacity, and the ponding depth as FullSWOF_2D considers the water depth when applying the Green-Ampt method [32]. Under small rainfall intensity and higher

infiltration rate, it was possible for all runoff to infiltrate downward and the bioretention cell did not have any ponding. The infiltrated runoff volume, V_{inf}, decreased from RBS01 (4.28 m^3) to RBS17 (3.09 m^3, Table 4.5, L = 40 m group), mainly because the smaller longitudinal slope, S_o, increased the ponding area, since h_b and the infiltration parameters were the same for these five modeling cases. For RBS01, RBS05, and RBS09, $L \times S_o \leq h_b$, so that the maximum ponding area was 40 m × 1 m (width of the bioretention strip); for RBS13 and RBS17, $L \times S_o > h_b$, so that the maximum ponding area was less than 40 m × 1 m (only covered 28.6 m and 20 m, respectively).

There was no overflow through the grate inlet in the bioretention strip for the modeling cases of L = 10 m (V_{bog} = 0) because the overflow height of the grate inlet (h_b) was the largest (0.4 m, D_b—0.05 in Table 4.1), but the maximum ponding depth (h_{max}, Table 4.7) was less than h_b for these cases. All other three modeling groups (L = 20, 30, and 40 m) overflowed through the grate inlet in the bioretention ($h_{max} > h_b$, Table 4.7). The increase of the overflow grate-inlet volume V_{bog} (Table 4.5) was mainly because of the increase of the longitudinal slope (S_o) when L and h_b were unchanged. The mean V_{bog} increased from 1.59 m^3 (L = 20 m group) to 10.11 m^3 (L = 40 m group) when h_b decreased from 0.3 to 0.2 m. This indicated that the overflow height, h_b, was a key design parameter of the RBS to retain the runoff inside the bioretention.

The mean V_{bog} percentage, i.e., $V_{bog}/(V_{ci} + V_{rb})$, increased when h_b decreased: 20.7 ± 12.7% for the L = 20 m group (h_b = 0.30 m), 44.4 ± 8.8% for the L = 30 m group (h_b = 0.25 m), and 58.4 ± 10.2% for the L = 40 m group (h_b = 0.20 m). When h_b was small, the grate-inlet overflow became the main mechanism to remove the extra runoff in the bioretention strip as indicated by the larger V_{bog} percentage.

The mean overflow peak discharge, Q_{pog}, increased from 4.81 L/s to 12.65 L/s for L = 20–40 m groups (Table 4.7) when the total inflow (V_{ci} + V_{rb}) increased, h_b decreased also. The bioretention overflow-start-time, (T_{bog}) and Q_{pog}, were mainly related to V_{ci} and h_b. T_{bog} decreased from 974.8 ± 188.2 sec (L = 20 m group) to 391.6 ± 252.5 sec (L = 40 m group).

Table 4.7. Mean and standard deviation (numbers inside brackets) of additional simulation results calculated from each of the five road-bioretention cases with the same L (10–40 m).

Length (*L*)	h_{max} **(m)**	T_{bog} **(s)**	Q_{pog} **(L/s)**	V_{pc} **(m^3)**	$V_{bio(40)}/V_{pc}$ **(-)**	Q_{prgb} **(L/s)**	Q_{prgb}/Q_{prg} **(-)**
10 m RBS [1]	0.36	-	0.00	4.02	0.77	3.84	0.57
	(0.02)		(0.00)	(0.22)	(0.03)	(0.19)	(0.02)
20 m RBS [2]	0.32	975	4.81	5.12	0.95	8.30	0.71
	(0.01)	(188)	(2.17)	(0.80)	(0.01)	(0.19)	(0.04)
30 m RBS [3]	0.29	650	9.43	5.27	0.93	11.23	0.71
	(0.00)	(255)	(1.15)	(1.67)	(0.02)	(0.72)	(0.03)
40 m RBS [4]	0.24	392	12.65	4.36	0.89	13.14	0.76
	(0.01)	(252)	(1.81)	(2.22)	(0.03)	(0.92)	(0.10)

Note: [1] for RBS04, 08, 12, 16, and 20; [2] for RBS03, 07, 11, 15, and 19; [3] for RBS02, 06, 10, 14, and 18; [4] for RBS01, 05, 09, 13, and 17; h_{max} (m) is the maximum ponding depth (water height) in the bioretention, T_{bog} (sec) is the time when the bioretention overflow starts, Q_{pog} (L/s) is the bioretention overflow peak discharge, V_{pc} (m^3) is the calculated maximum bioretention ponding volume based on bioretention-strip geometry, $V_{bio(40)}/V_{pc}$ is the percentage of the bioretention ponding volume at the end of the 40-min simulation to the calculated bioretention ponding volume, Q_{prgb} (L/s) is the road grate inlet peak discharge for RBS cases, Q_{prgb}/Q_{prg} is the ratio of the road grate inlet peak discharge for RBS case to corresponding Rd case.

The bioretention overflow was delayed when the overflow height, h_b, increased. The bioretention overflow was first projected to start at 163 sec in the RBS17 modeling case and reached the peak discharge of 14.92 L/s. The main reason was the largest curb inlet

intercepted runoff volume of RBS17 (15.72 m^3) due to the large L and S_x and the lowest h_b = 0.20 m.

For all 20 RBS cases (Table 4.5), the mean ponding volume in the bioretention (V_{bio}) were 3.10 m^3 for the L = 10 m group, 4.86 m^3 for the L = 20 m group, 4.93 m^3 for the L = 30 m group, and 3.93 m^3 for the L = 40 m group when the rainfall intensity was large (250 mm/h). V_{bio} is a function of time and shows the integrated/cumulative effects of different flow processes (inflow from curb inlet, outflow through the overflow grate inlet, rainfall, and infiltration). $V_{bio}(t)$ is also related to the bioretention strip's ponding capacity, which was determined by the bioretention-strip geometry as shown in Equation (4.9). There are four modeling cases (RBS09, 13, 17, and 18; Table 4.1) with $L \times S_o \geq h_b$; therefore, the overflow height, h_b, was the only controlling factor for $V_{bio}(t)$, independent of $L \times S_o$ for these four cases.

From the beginning of the simulation, when the ponding depth was zero (more infiltration and zero runoff), $V_{bio}(t)$ was zero. When the ponding depth increased from zero to h_b, $V_{bio}(t)/V_{pc}$ increased from zero to 1.0, since V_{pc} (Equation (4.9) is the calculated maximum bioretention ponding volume at h_b. When the overflow through the grate inlet took place in the bioretention strip, $V_{bio}(t)/V_{pc}$ was greater than 1.0. After the rainfall stopped, eventually, $V_{bio}(t)$ was zero when the ponding depth decreased to zero. In this study, $V_{bio}(t)$ at the end of the simulation (t = 40 min) for each RBS case is shown in Table 4.5 and was used to calculate the runoff-volume mass-balance percent difference (ΔV) in the whole simulation domain. These percent differences (Table 4.5) were very small, with an average of −0.02%, and indicated that the RBS simulation results were reasonable.

The average $V_{bio}(40)$ percentage, $V_{bio}(40)/(V_{ci} + V_{rb})$ at the end of simulation, t = 40 min, was larger when h_b was larger: 75.6 $\pm$ 0.2% for the L = 10 m group (h_b = 0.4 m), 64.3 $\pm$ 11.8% for the L = 20 m group, 40.3 $\pm$ 26.7% for the L = 30 m group, and 24.2 $\pm$ 26.3% for the L = 40 m group (h_b = 0.2 m). The higher $V_{bio}(40)$ percentage means that more runoff was ponded and waited for infiltration when the simulation ended. The ponding volume, $V_{bio}(40)$, for each case was compared with V_{pc}, and the ratio ranged from 0.73 to 0.96 (Table 4.7).

At the end of the simulation, $V_{bio}(40)$ was smaller than $V_{pc,}$ and the mean ratios of V_{bio}/V_{pc} were 0.77–0.95 for the changing L. The results in Table 4.7 and Equation (4.9) indicate that it is necessary to consider three parameters, S_o, L, and h_b, when calculating the ponding capacity of the bioretention; this was especially important in the continuous RBS system when these three parameters changed in different RBSs. In this study, the vegetation volume fraction was not considered when calculating V_{pc}. Therefore, we need to use a safety factor to calculate the actual ponding volume based on the bioretention geometry and vegetation volume fraction when designing a continuous RBS system.

4.3.3 Implications of the Simulation Results on RBS Design

In this study, three implications can be drawn through the detailed analysis of the simulation results of the 20 RBS cases.

(1) The curb inlet could be the bottleneck of a continuous road-bioretention facility that impedes the runoff generated from the road flowing into the bioretention to infiltrate, detain (pond), and improve the stormwater quality. The analysis of 20 RBS performance indicated only 34.6–48.4% of the total runoff volume (Table 4.5) was intercepted by the curb inlet when the intensity was 250 mm/h for 20 min, and the remaining part of the runoff

flowed downstream along the road, which may cause local inundation and become a safety hazard. Many bioretention system designs do not pay much attention to the curb inlet interception efficiency but only focus on the bioretention BMP itself. It is necessary to appropriately design the curb inlet to intercept enough stormwater runoff to improve the performance of RBS based on detailed hydraulic calculations, for example, using the HEC-22 method. Equations (4.1)–(4.3) indicate that HEC-22 considers the effects of the road longitudinal slope, cross slope, surface roughness, incoming flow or spread, and the inlet length on the curb inlet interception efficiency. The HEC-22 method has been widely used in the USA for drainage inlet design but is seldom used for designing inlets for LID facilities. The HEC-22 calculated and FullSWOF-ZG simulated curb inlet efficiencies will be compared and evaluated in a future study.

It also should be mentioned that the bottleneck of the curb inlet to RBS was simulated to occur under heavy rainfall intensity (250 mm/hr) over a short duration (20 minutes). Further studies to identify the bottleneck of RBS are necessary when the rainfall intensity is smaller over a long duration, which could lead to saturation in bioretention media layer and gravel storage layer (infiltration is limited by the native soil and the capacity of underdrain). It is still possible for the curb inlet to be the bottleneck of an RBS when the inlet length is small, e.g., 6 inches (smallest curb inlet length for the bioretention facilities in Philadelphia), and the rainfall intensity is normal or moderately severe.

(2) Bioretention BMP is intended to detain the runoff intercepted by the inlet under frequent rainfall events (e.g., the 95th percentile rainfall), and some current practices of the RBS design in China that eliminate necessary grate inlets on the road could cause local flooding (inundation) on the road under heavy rainfall events. The analysis of 20 RBS's

performances indicated that the runoff generated from the road, but could not be intercepted by the curb inlet. Thus it needed to be captured by the grate inlet downstream from the curb inlet (Figure 4.4). In this study, the percent of runoff captured by the road grate inlet for the RBS system ranged from 44.2% to 61.7% (Table 4.5) under 250 mm/h heavy rainfall over 20 min. This indicated the importance of the grate inlet downstream of the curb inlet for the RBS system. The curb inlet intercepted the runoff for the bioretention strip, and the grate inlet intercepted the bypassed flow after the curb inlet.

The peak discharges of the road grate inlet for 20 RBS modeling cases (Q_{prgb}, Table 4.7) were compared with the corresponding Q_{prg} for the road-only modeling cases. For all 20 RBS cases, the average Q_{prgb} increased from 3.84 L/s to 13.14 L/s for an L increase from 10 to 40 m. Comparing with Q_{prg}, the average ratio of Q_{prgb}/Q_{prg} were from 0.57 to 0.76 for L = 10–40 m groups. The overall average $\pm$ standard deviation of Q_{prgb}/Q_{prg} for 20 modeling cases was 0.69 $\pm$ 0.09, which indicates that the curb inlet and grate inlet combination could reduce the road grate inlet peak discharge and help to relieve road local flood inundation. Therefore, the curb inlet and grate inlet combination greatly benefit the runoff control, local flood inundation relief, and traffic safety, especially for continuous road-bioretention. Eliminating the grate inlets on the road for the RBS system is not a recommended design practice.

(3) A safety factor should be adopted to calculate the bioretention ponding volume when designing the RBS system. The actual ponding volume should be equal to the ponding volume calculated based on the bioretention geometry (V_{pc}) multiplied by the safety factor used for RBS design. The berm at the end of a bioretention cell (Figures 4.1 and 4.2) is typical to pond the runoff for infiltration and to ensure that the overflow

discharges through the grate inlet rather than flowing into the bioretention downstream. For the RBS13, RBS17, and RBS18 modeling cases, $L \times S_o > h_b$, so that the maximum ponding and infiltration area was less than the total bioretention surface area (e.g., 40 m × 1 m in this study), which is not a recommended design configuration for the bioretention strip. The distance between the ditch dikes should be small enough to have $L \times S_o \leq h_b$ or pond the runoff in the whole bioretention area. The bioretention ponding volume is influenced by the bioretention cells' geometry, including the length, longitudinal slope, and overflow height; it can be computed using Equation (4.9), but the vegetation volume fraction can be important when the vegetation density in the bioretention is very high (Figure 4.2a) so that a ponding volume safety factor should be introduced. The EPA-SWMM model suggests the vegetation volume fraction of 0.1–0.2; therefore, the safety factor used for RBS design in computing the ponding volume should be 0.8–0.9.

4.4 Summary and Conclusions

The open-source Full Shallow-Water equations for Overland Flow in the two-dimensional (FullSWOF_2D) program, which applies the uniform rainfall and infiltration parameters to the whole simulation domain, was revised to include 2D plane zones (Z) with different rainfall and infiltration parameters and a 2D-1D grate-inlet (G) drainage module. The FullSWOF-ZG program was tested with the overland flow of eight pervious surface rainfall-runoff events and 20 impervious roads with a type C curb inlet to study whether the program could accurately simulate the overland flow on a pervious and impervious surface and accurately predict the curb inlet interception efficiency. Twenty road-bioretention strip or RBS modeling cases were designed based on the commonly used parameters (longitudinal and cross slopes, curb opening length, soil infiltration parameters,

the bioretention depression depth, and the overflow height) and evaluated with FullSWOF-ZG. The simulation results were analyzed and demonstrated that the RBS hydrological performance, i.e., to intercept then infiltrate the runoff, was jointly influenced by several parameters. Even if the complex relationship between the RBS performance and all input parameters were not fully explored by using only 20 cases, we would suggest three main points resulting from this study. (1) The RBS's curb inlet could be the bottleneck of its hydrologic performance and should be designed to improve inlet interception efficiency, e.g., using procedures and equations in HEC-22; (2) The curb inlet and road grate inlet combination is necessary for continuous RBS because the road surface runoff could not be 100% intercepted by the curb inlet alone; and (3) it is necessary to consider the safety factor of the high-density vegetation and the relationship of overflow height, bioretention cell length, and longitudinal slope when calculating the ponding volume for the RBS design. The RBS performance evaluation and design under different rainfall distribution and intensity situations will be conducted in a future study. The performance improvement of RBS with different types of curb inlet will also be conducted in a future study to provide suggestions for SPC construction in China and LID practices (especially bioretention BMPs) over the world.

Chapter 5. Exploration and Quantification of Curb Inlet Efficiency Improvement

5.1 Introduction of the deep-cut curb inlets

The deep-cut (DC) curb inlets were used in some of the retrofit sponge-city (SPC) projects for that they were easily implemented and based on engineer's or design's field experience. The efficiencies of the deep-cut curb inlets in those projects were unknown because there is no standard equation that can be used to calculate their efficiencies. Two kinds of retrofit scenarios were simulated in this study (Figure 5.1): 1) the deep cut is made only over the width of the curb inlet (Figure 5.1b); 2) both the curb inlet and a small part of road surface have a deep cut (Figure 5.1c). For the first scenario, two hundred cases with one longitude slope (S_o), 10 cross slopes (S_x), 10 upstream inflows (Q_{in}) to determine the 100% interception curb inlet lengths, L_T with a cut depth d equal to 0.1 m and 0.15 m. Another two hundred cases with the same longitude slope and 10 cross slopes plus 10 curb inlet lengths (L_{ci}) were used to determine the curb inlet efficiencies, E_{ci} with d = 0.1 m and 0.15 m. For the second scenario, two hundred cases with one longitude slope, 10 cross slopes, 10 upstream inflows to determine the 100% interception curb inlet lengths, L_T with a cut width w on the road surface equal to 0.05 m and 0.1 m (Figure 5.1a). Another two hundred cases with the same longitude slope and 10 cross slopes plus 10 curb inlet lengths were used to determine the curb inlet efficiencies, E_{ci} with cut width equal to 0.05 m and 0.1 m. Therefore, a total of eight hundred modeling cases for the deep cut curb inlets were designed and modeled using the FullSWOF-ZD program. These cases were compared with the results in Chapter 3 to explore and quantify the efficiency improvement by cutting the curb inlet simply (Figure 5.1).

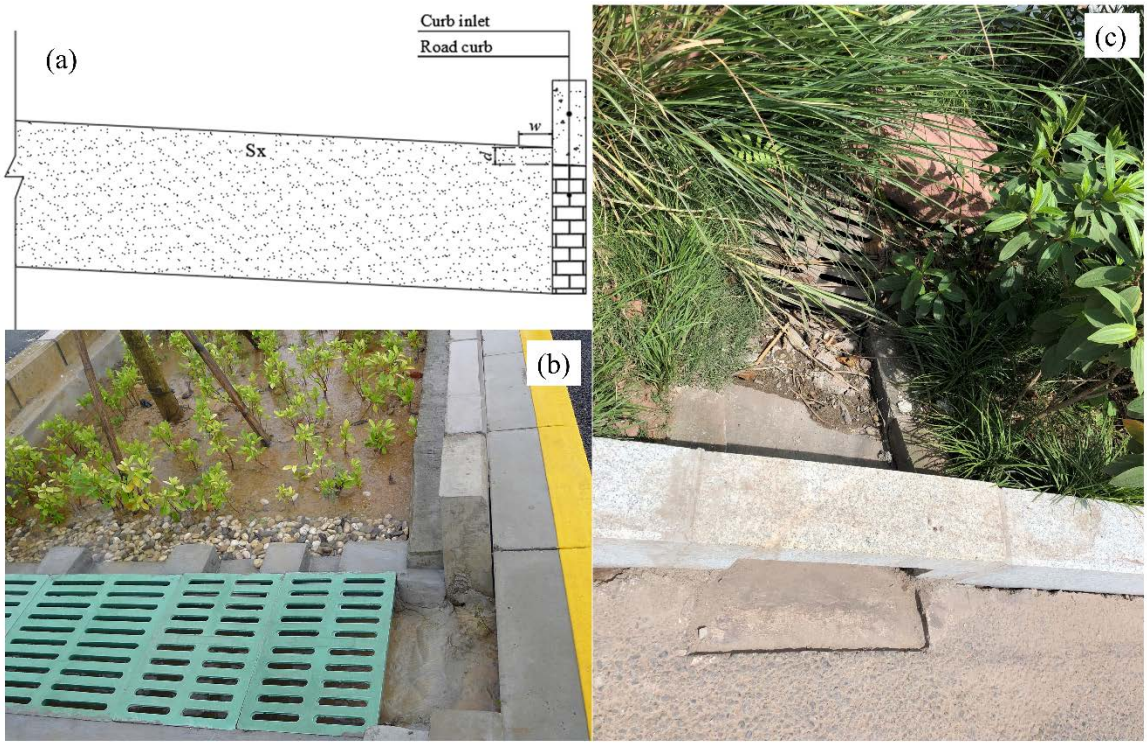

Figure 5.1. (**a**) Cross-section view of simply cut curb inlet, where S_x is the cross slope, *d* is the deep-cut depth, and *w* is the width of the deep cut on the road surface, (**b**) the deep cut over the curb inlet width only, (**c**) the deep cut over the curb inlet and a small part of the road surface. Photos (**b**) and (**c**) show these deep cuts have been implemented in sponge city projects in Shenzhen and Ningbo, respectively.

The deep-cut (DC) curb inlets have been used to retrofit the undepressed (UD) curb inlets, where there is one cross slope for the road surface including the gutter and the curb inlet (Figure 5.1). In this study, the curb width or thickness was set at 0.1 m (10 cm) along the cross-slope direction. The deep cut for the curb inlet and the road surface results in a local depression of *d* m (Figure 5.1a). When a deep cut is also made on the road surface, the width on the road surface is *w* m along the cross-slope direction (Figure 5.1a) having a local depression *d*. Therefore, the elevation of the deep cut over the curb inlet or plus *w*-

width road surface is *d* m lower than the nearby road/gutter surface. Typically, *d* could be about 0.05–0.2 m. The implementation of the deep cuts was based on some field observations that the UD curb inlets are not effectively intercept the runoff into the bioretention strip. To improve the interception efficiency, the curb inlets were retrofitted by simply cutting the curb inlet deeper to create a local depression, for example, making the curb inlet opening area to be 0.1–0.15 m lower than the original surface (Figure 5.1b). The effectiveness of the retrofitted curb inlet to increase the interception efficiency is still unknown and worth to be investigated.

Compared to undepressed curb inlets, the composite-cross-slope curb inlets with larger cross slope at the gutter have larger interception capacity for the road-bioretention strips (Brown et al., 2009). However, the performance of the UD curb inlets with two kinds of deep cuts (Figure 5.1b and Figure 5.1c) was still not quantified in previous studies.

5.2 Materials and Methods

5.2.1 100% Interception Curb Inlet Evaluation Cases for the Curb-Cut Scenarios

The DEMs for the two kinds of the DC inlets under different longitudinal slopes, cross slopes, and curb inlet lengths were established using MATLAB code. Figure 5.2 shows the plan view and high-resolution DEMs for three modeling cases with $S_0 = 0.01$ and $S_x = 0.06$. The only difference for Figure 5.2 (a), (b), and (c) is that the deep cut depth *d* over the curb inlet. The cut depths of Figure 5.2 (a), (b), and (c) are 0 m (a UD inlet), 0.1 m, and 0.15 m, respectively. The area in the red rectangular is the simulation domain for all modeling cases in this study and is 15 m in length and 6.7 m in width. The part in the black rectangular

(outlined as a dashed line) is the curb inlet opening used to determine the 100% interception curb inlet length for different deep-cut scenarios.

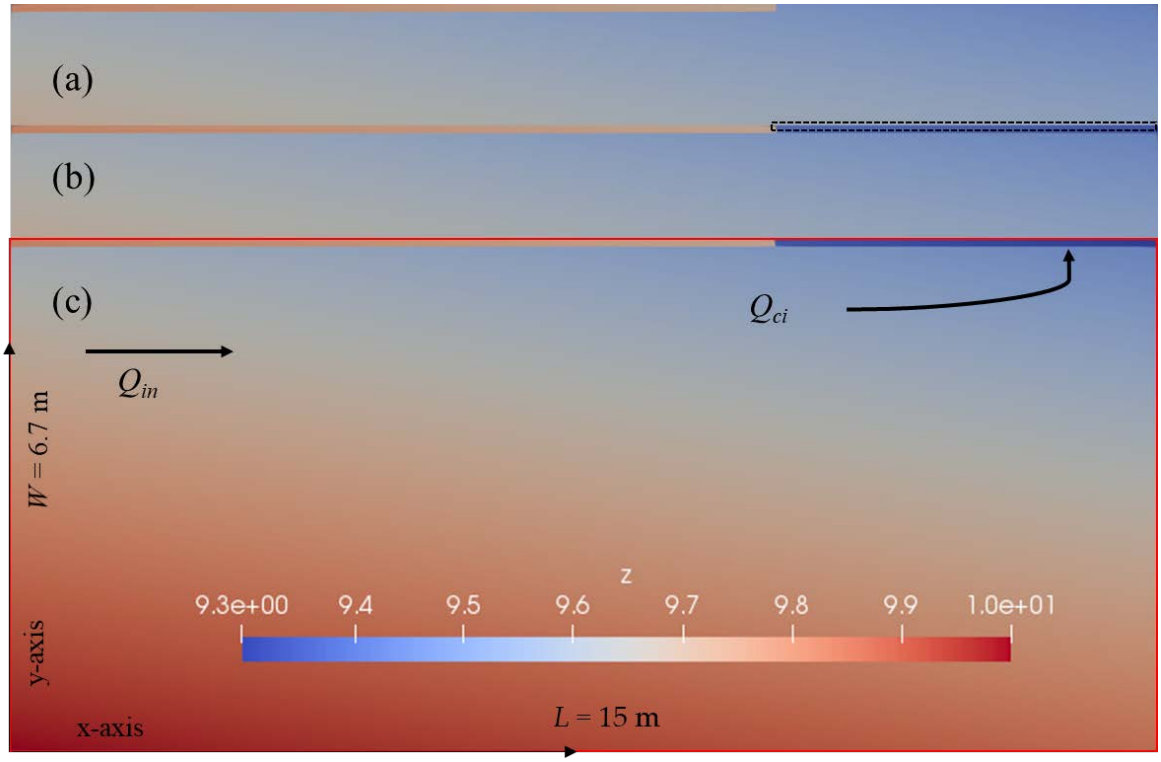

Figure 5.2. Plan view of three deep cut cases to explore 100% interception curb inlet lengths (L_T) with S_0 = 0.01, S_x = 0.06. The deep cut depth d = 0 m for (**a**), 0.1 m for (**b**), and 0.15 m for (**c**). The area in the red rectangular is the whole simulation domain, the part in the black rectangular is the curb inlet part used to determine the L_T.

In this study, the main purpose is to quantify the improvement of the deep-cut curb inlet efficiency compared to undepressed curb inlets. The upstream inflow Q_{in} is set at the left boundary of the simulation domain and flows towards the downstream to the right boundary. The 100% interception curb inlet length L_T is the curb-opening length when all upstream inflow is intercepted by the deep cut curb inlet ($Q_{in} = Q_{ci}$). In the model set up

(Figure 5.2), the curb opening length was made to be relatively long (5 m), longer than L_T to be determined.

All cell's elevations in the simulation domain were calculated using a MATLAB program when the bottom-left-corner reference cell's elevation (the highest in the domain) was assumed to be 10 m. The road surface elevations vary with longitudinal and cross slopes. All cells for the 0.1 m wide curb were set 0.2 m higher than the road surface cells. The cell's elevations inside the curb inlet were first calculated using the same cross slope of the road surface and then subtracted by the deep-cut depth (d in Figure 5.1) to obtain the final cell's elevation for the deep cut modeling cases, which was expected to help and allow the runoff to flow into the bioretention. The deep cut inside the curb inlet has a local depression d from the nearby road surface. It is simple and easy to implement when retrofitting the bioretention strip projects to hopefully improve the road-bioretention strip performance.

Two hundred modeling cases were selected and modeled to determine the curb inlet length L_T of 100% interception under different S_0, S_x, and Q_{in}. The length and width of the simulation domain for these 200 modeling cases were 15 m (x-direction) including 10 m road surface before the inlet opening and 6.7 m (y-direction) including 3 m wide car lane stripe, 1.5 m wide bike lane strip, 2.1 m parking stripe (1.5 m + 0.6 m gutter), and 0.1 m curb width. The cell size of DEMs for all 200 cases was 0.025 m determined by a sensitivity analysis. The depth limit equal to 0.2 mm was used to determine the L_T which is already tested in chapter 3.

Commonly used S_0 and S_x values in stormwater drainage design were chosen from the HEC-22 (Brown et al., 2009) for 100 modeling cases, which are the combinations of one

longitudinal slope S_0 = 0.01 (1%), 10 cross slopes S_x = 0.015–0.06 (1.5–6%), and 10 upstream inflows Q_{in} = 6–24 L/s (Table 5.1). The first 100 modeling cases have a deep-cut depth d of 0.1 m and the second 100 modeling case having d = 0.15 m. The case number was named using the sequence number (1–10) of the parameter's choice of S_x, and Q_{in}; for example, the modeling case D1X1Q1 means the road having S_0 = 0.01 (1%), a cut depth d = 0.10 m, S_x = 0.015 (1.5%) with Q_{in} = 6 L/s for upstream inflow. The modeling case D2X1Q1 has a cut depth d = 0.15 m with the same S_0, S_x, and Q_{in} for D1X1Q1 case.

Table 5.1. Sequence numbers and corresponding geometry and inflow parameters of deep cut curb inlet modeling cases.

Sequence No.	**S_x (%)**	**Modeling case index [1]**	**Q_{in} (L/s)**	**Modeling case index [2]**	**L_{ci} (m)**
1	1.5	D1X1Q1	6	D1X1L1	0.15
2	2.0	D1X2Q2	8	D1X2L2	0.30
3	2.5	D1X3Q3	10	D1X3L3	0.45
4	3.0	D1X4Q4	12	D1X4L4	0.60
5	3.5	D1X5Q5	14	D1X5L5	0.75
6	4.0	D1X6Q6	16	D1X6L6	0.90
7	4.5	D1X7Q7	18	D1X7L7	1.05
8	5.0	D1X8Q8	20	D1X8L8	1.20
9	5.5	D1X9Q9	22	D1X9L9	1.35
10	6.0	D1X10Q10	24	D1X10L10	1.50

Note: [1] - modeling case for determining curb inlet length L_T of 100% interception when cut depth d = 0.1 m, [2] - modeling cases for determining inlet efficiency E_{ci} of different length L_{ci} when Q_{in} = 10 L/s.

5.2.2 Curb Inlet Efficiency Evaluation Cases for the Curb-Cut Scenarios

To evaluate the curb inlet efficiency E_{ci} at different inlet lengths (Figure 5.3), the second 200 modeling cases were selected using 10 choices of L_{ci}, 2 cut depths d, and the same 10 choices for S_x, which were used for the 200 modeling cases to determine L_T. Ten curb inlet opening lengths L_{ci} range from 0.15–1.5 m (6–60 inches) with an increase of 0.15 m (6 inches), which was adapted based on the curb inlet survey conducted by Stoolmiller et al. (2018). The imposed upstream inflow Q_{in} was chosen as 10 L/s for the left boundary condition of the domain for the second 200 modeling cases, and a part of the inflow is intercepted by the curb inlet, i.e., Q_{ci} , and the remainder of the inflow is discharged or bypassed downstream along the road (Q_{bp}), where the inlet length L_{ci} is less than L_T for 100% interception. The modeling case D1X1L1 means the road having S_0 = 0.01 (1%), cut depth d = 0.10 m, S_x = 0.015 (1.5%) with L_{ci} = 0.15 m. Figure 5.3 shows DEMs and model set up for D1X10L10 and D2X10L10 (L_{ci} = 1.50 m), and it is a UD curb inlet when d = 0, which has been simulated in Chapter 3.

This study aims to attract more engineers and designers focus on the curb inlet design for road-bioretention strips with quantified performance improvement instead of designing them only considering the landscape perspectives. The quantified results also hope to provide the proof in the road-bioretention strips curb inlet design and retrofit and to understand whether and how the deep cut should be implemented.

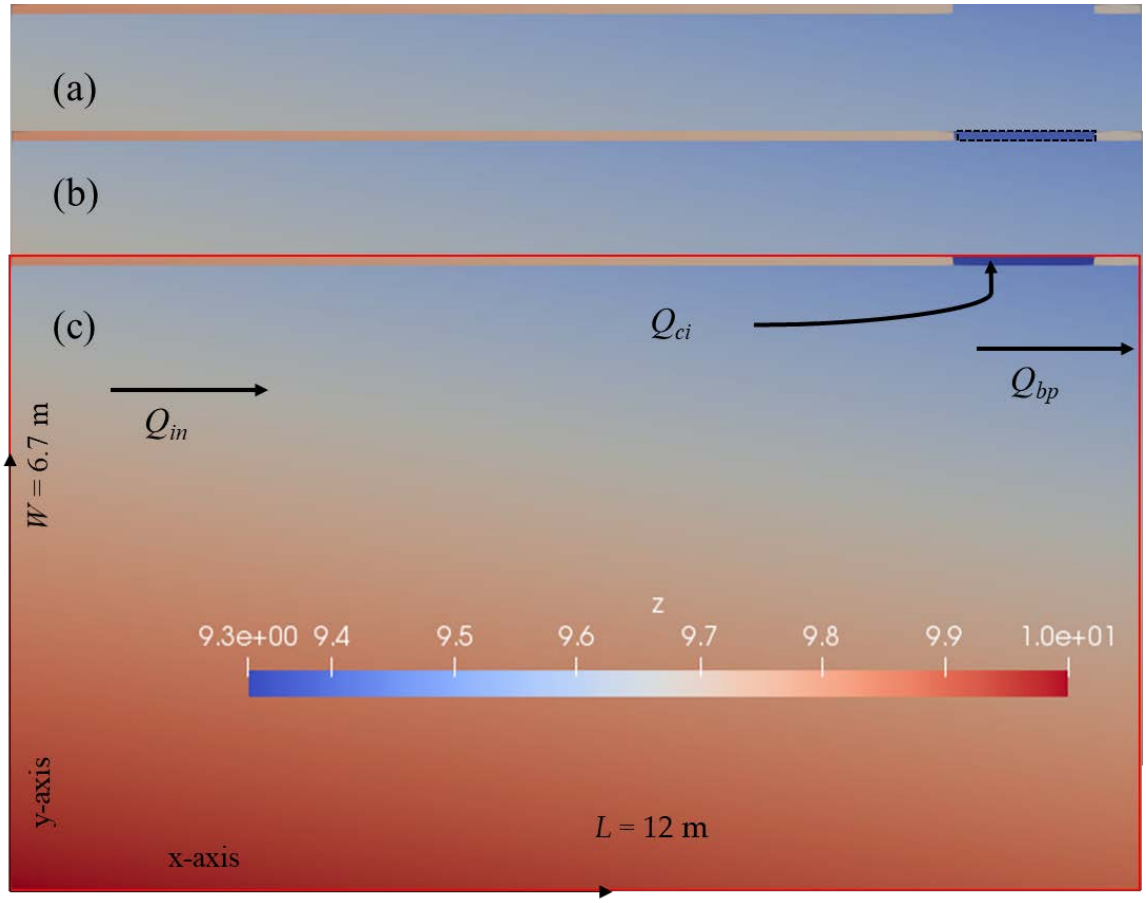

Figure 5.3. Plan view and DEMs of three deep cut cases to explore curb inlet efficiency with S_0 = 0.01, S_x = 0.06. The deep-cut depth d = 0 m for (**a**), 0.1 m for (**b**), and 0.15 m for (**c**). The area in the red rectangular is the whole simulation domain, the part in the black rectangular is the curb inlet part used to determine the E_{ci}.

5.2.3 100% Interception Curb Inlet Evaluation Cases for the Road-Curb Cut Scenarios

Figure 5.4 shows the plan view and high-resolution DEMs for three modeling cases with S_0 = 0.01 and S_x = 0.06 for the road-curb cut scenarios. The difference for Figure 5.4 (a), (b), and (c) is the cut width w on the road surface. The road cut width w of Figure 5.4 (a), (b), and (c) are 0 m, 0.05 m, and 0.10 m, respectively; and the deep cut over the curb

is always 0.1 m. The case *a* in Figure 5.4 is the same as the case *a* in Figure 5.2 with a cut depth of 0 m.

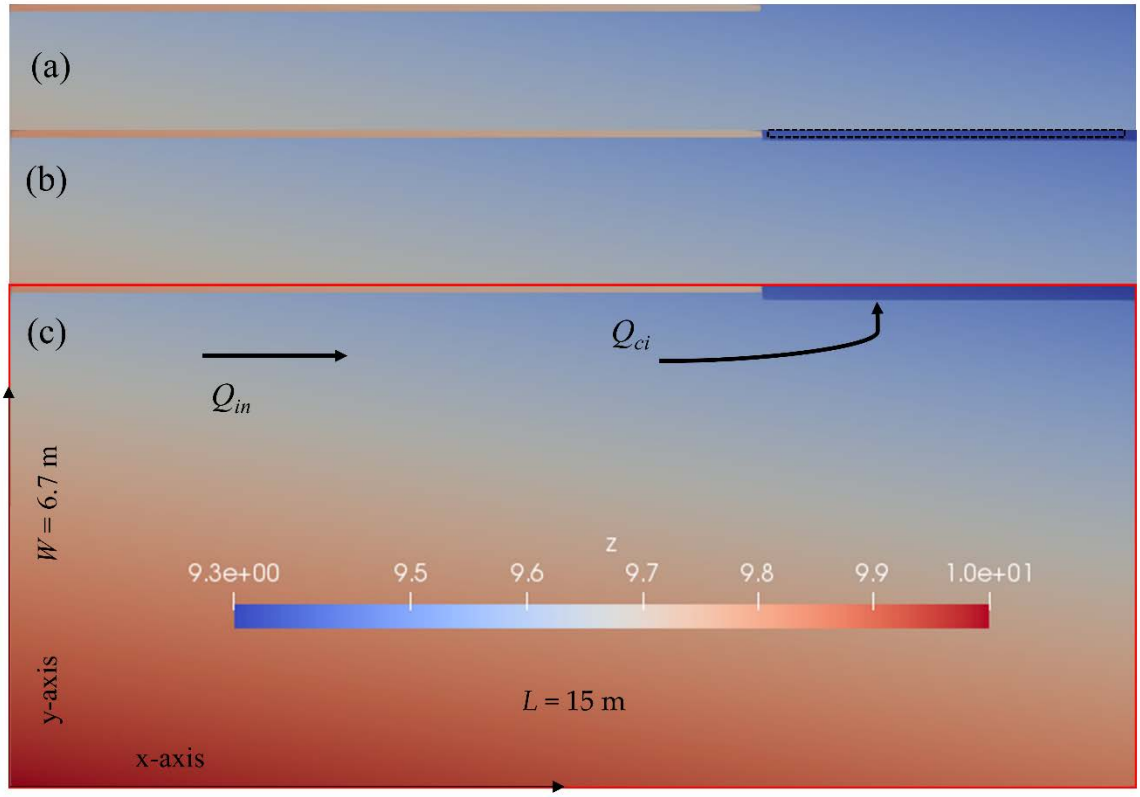

Figure 5.4. Plan view and DEMs of three deep cut cases to explore 100% interception curb inlet length with S_0 = 0.01, S_x = 0.06. The road cut width w = 0 m for (**a**), 0.05 m for (**b**), and 0.10 m for (**c**). The area in the red rectangular is the whole simulation domain, the part in the black rectangular is the curb inlet part used to determine the L_T.

In this part of the study, the deep-cut depth for the curb inlet and road surface was fixed at 0.1 m for all cases with S_0 = 0.01 (1%). The case number was named using the sequence number (1–10) of the parameter's choice of w, S_x, and Q_{in}; for example, the modeling case R1X1Q1 means the road having a cut width w = 0.05 m, S_x = 0.015 (1.5%), and Q_{in} = 6 L/s for upstream inflow. Ten R1X*m*Q*m* (*m* = 1, 2, …, 10) modeling cases and parameters are listed in Table 5.2. The 100 modeling cases R2X*m*Q*n* (*m* or *n* = 1, 2, …,

10) mean the road having a cut width w = 0.10 m. The curb opening length was set large enough to intercept 100% inflow for these third 200 modeling cases.

5.2.4 Curb Inlet Efficiency Modeling Cases for the Road-Cut Scenarios

To evaluate the curb inlet efficiency E_{ci} at different inlet lengths (Figure 5.5) with different cut widths over the road and curb inlet, the fourth 200 modeling cases were selected using 10 choices of L_{ci}, 2 cut widths w, and the same 10 choices for S_x, which were used for the third 200 modeling cases to determine L_T.

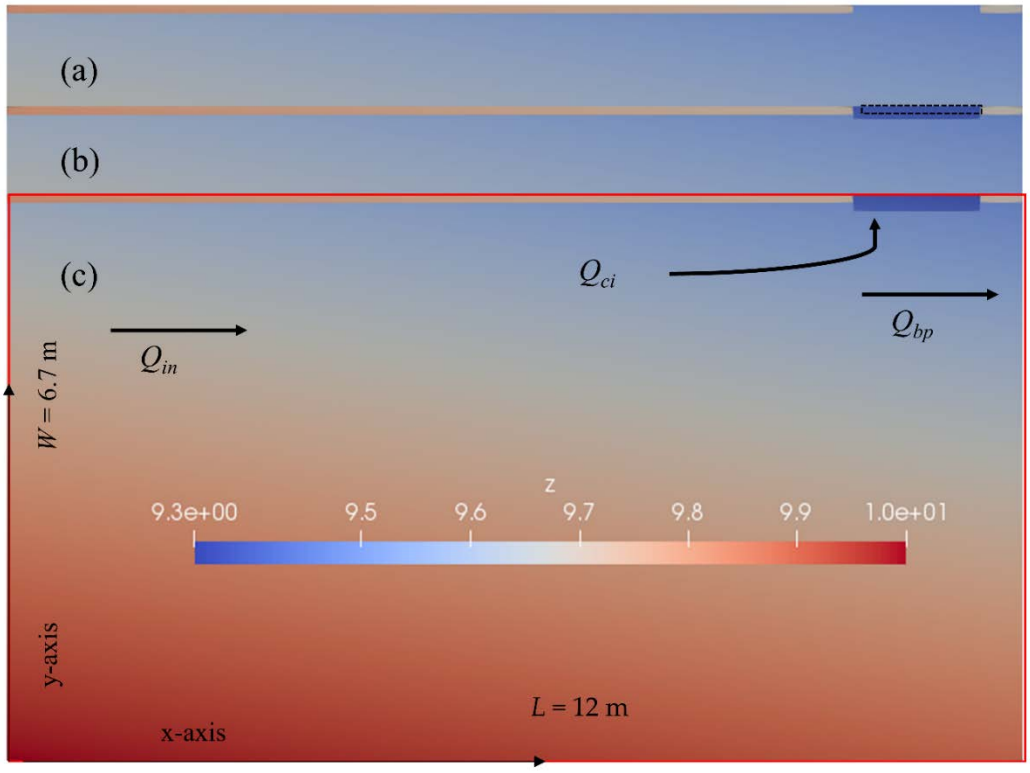

Figure 5.5. Plan view and DEMs of three deep-cut cases to explore curb inlet efficiency with S_0 = 0.01, S_x = 0.06, L_{ci} = 1.50 m. The deep cut depth w = 0 m for (**a**), 0.05 m for (**b**), and 0.10 m for (**c**). The area in the red rectangular is the whole simulation domain, the part in the black rectangular is the curb inlet part used to determine the E_{ci}.

Ten curb inlet lengths L_{ci} were again ranged from 0.15–1.5 m (6–60 inches) with an increase of 0.15 m (6 inches) (Stoolmiller et al., 2018). The imposed upstream inflow Q_{in} was chosen as 10 L/s for the left boundary condition of the domain. The modeling case R1X1L1 means the road having a cut width w = 0.05 m, S_x = 0.015 (1.5%), and L_{ci} = 0.15 m. Figure 5.5a is the same as the case *a* in Figure 5.3.

Table 5.2. Sequence numbers and corresponding geometry and inflow parameters of road cut curb inlet modeling cases.

Sequence No.	**S_x (%)**	**Modeling case index [1]**	**Q_{in} (L/s)**	**Modeling case index [2]**	**L_{ci} (m)**
1	1.5	R1X1Q1	6	R1X1L1	0.15
2	2.0	R1X2Q2	8	R1X2L2	0.30
3	2.5	R1X3Q3	10	R1X3L3	0.45
4	3.0	R1X4Q4	12	R1X4L4	0.60
5	3.5	R1X5Q5	14	R1X5L5	0.75
6	4.0	R1X6Q6	16	R1X6L6	0.90
7	4.5	R1X7Q7	18	R1X7L7	1.05
8	5.0	R1X8Q8	20	R1X8L8	1.20
9	5.5	R1X9Q9	22	R1X9L9	1.35
10	6.0	R1X10Q10	24	R1X10L10	1.50

Note: [1] - modeling case for determining curb inlet length L_T of 100% interception when cut depth d = 0.1 m, [2] - modeling cases for determining inlet efficiency E_{ci} of different lengths L_{ci} when Q_{in} = 10 L/s.

5.3 Results and Discussion

5.3.1 100% Interception Curb Inlet Lengths for the Curb Cut Scenarios

Figure 5.6 shows the comparison of 100% interception curb-inlet lengths L_T for 100 undepressed cases, 200 deep-cut modeling cases with d = 0.10 m and 0.15m. The 100%

interception curb-inlet length for 100 undepress cases range from 1.91 m to 7.59 m with average ± standard deviation equal to 3.69 ± 1.24 m. The percentage changes of L_T between the deep-cut cases (D1 and D2) and the undepressed cases (UD) with the same S_0, S_x and Q_{in} range from -1.09% to 0.00% with the mean absolute percentage change equal to -0.25%. The standard deviation of the percentage changes between the undepressed cases and the deep-cut cases was equal to 0.33%. The 100% interception curb-inlet lengths for the 200 deep-cut cases with different cut depths were basically the same as L_T for corresponding undepressed cases with the same cross slope and upstream inflow. It means if the deep cut is only made over the curb inlet width, the deep-cut depth (d = 0, 0.05, and 0.1 m) does not make any difference on L_T.

In this study, the cross slopes were from 1.5% to 6%. As reported in *Pavement and Geometric Design Criteria for Minimizing Hydroplaning (22), a* cross slope of 2% has little effect on driver effort in steering or on friction demand for vehicle stability. Use of a cross slope steeper than 2% on pavements with a central crown line is not desirable. In areas of intense rainfall, a somewhat steeper cross slope (2.5%) may be used to facilitate drainage. HEC-22 (Brown et al., 2009) states “On multi-lane highways where three lanes or more are sloped in the same direction, it is desirable to counter the resulting increase in flow depth by increasing the cross slope of the outermost lanes. The two lanes adjacent to the crown line should be pitched at the normal slope, and successive lane pairs, or portions thereof outward, should be increased by about 0.5 to 1%. The maximum pavement cross slope should be limited to 4%.” In China, many roads were constructed with small cross slopes, and there are also many roads with steep longitudinal slopes over the world.

Whether the deep cut can affect L_T for the roads with other slopes is still unknown since all modeling cases had 1% longitudinal slope.

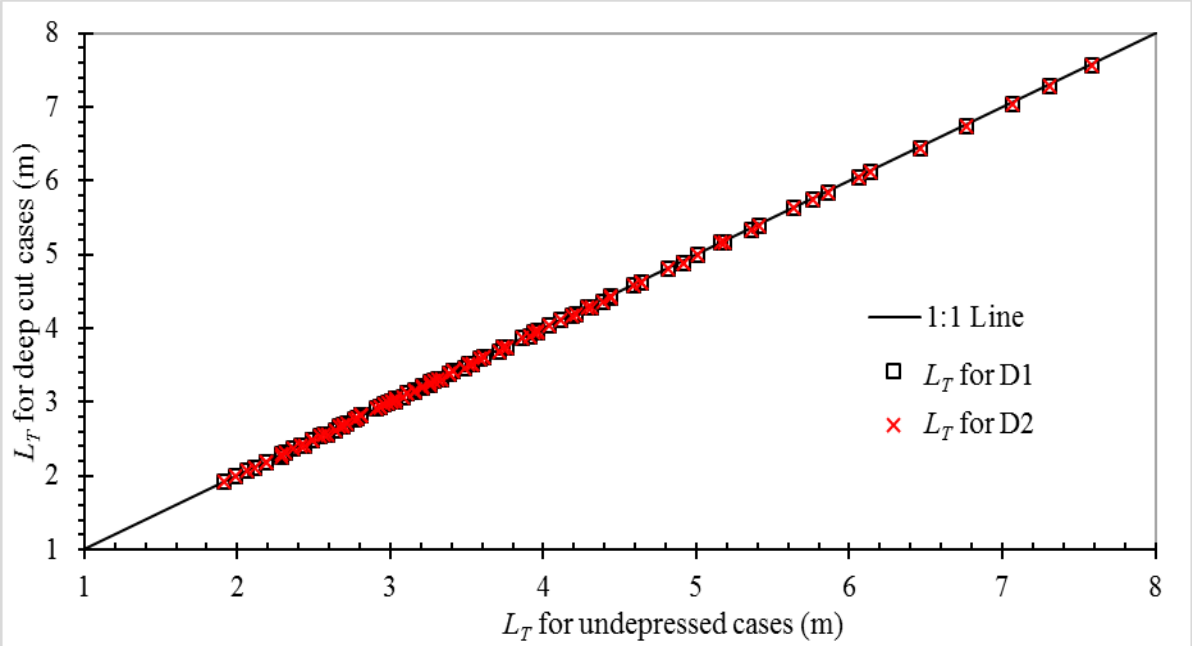

Figure 5.6. Comparison of 100% interception curb inlet length for undepressed, D1 (d = 0.1 m), and D2 (d = 0.15 m) cases.

5.3.2 Curb Inlet Efficiency for the Curb Cut Scenarios

Figure 5.7 shows the comparison of simulated curb inlet efficiencies for 100 undepressed modeling cases, 200 deep-cut modeling cases with d = 0.10 m and 0.15 m. The inlet efficiencies for the undepress curbs range from 4.68% to 94.47% with average $\pm$ standard deviation equal to 43.68% $\pm$ 25.04% when L_{ci} varied from 0.15 to 1.5 m. Simulated curb inlet efficiencies are the exactly same for d = 0.1 m and 0.15 m when other parameters are the same. The percent changes of the curb inlet efficiencies between the deep-cut cases (D1 and D2) and the undepressed cases (UD) range from 0.41% to 26.92% with the mean percentage change of 8.91% and the standard deviation of 6.87%. Since E_{ci}

for some cases is very small (< 20%), these percentage changes could be misleading. The E_{ci} changes between the deep-cut cases (D1 and D2) and the undepressed cases (UD) range from 0.39% to 6.01% and are greater than zero so that the deep cut only increases E_{ci} a few percents.

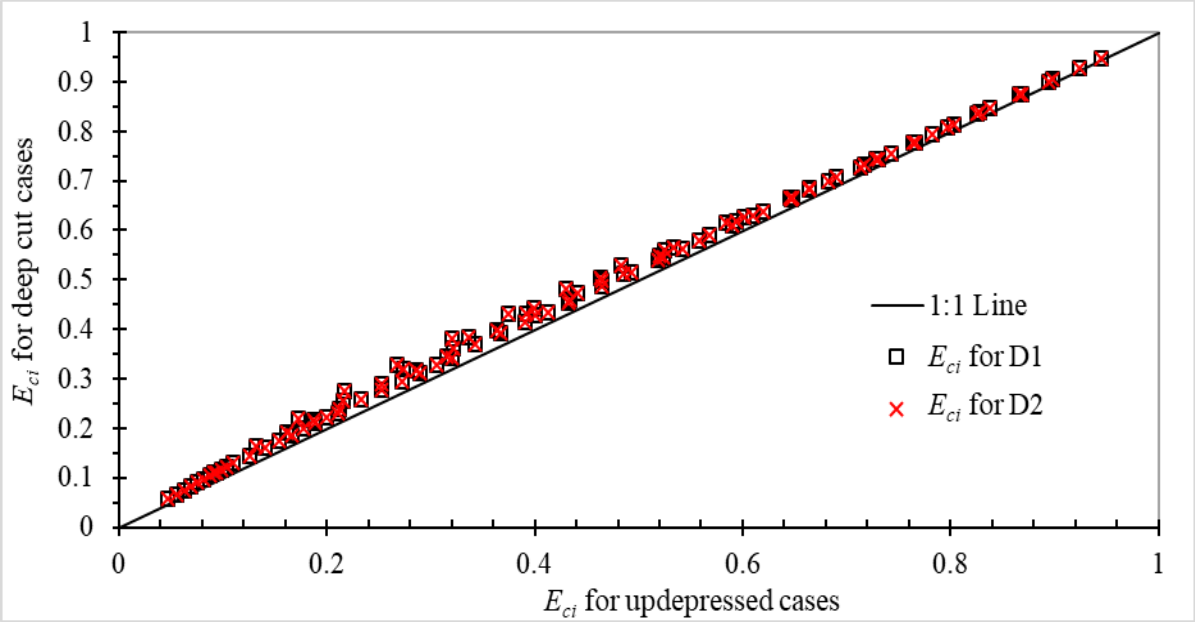

Figure 5.7. Comparison of curb inlet efficiency for undepressed, D1 (d = 0.1 m), and D2 (d = 0.15 m) cases.

Figure 5.6 and Figure 5.7 show that the differences of modeling cases between the deep cut at the curb inlet and undepressed curb inlets are very small in terms of the 100% interception curb inlet length and the inlet efficiency. Therefore, it is not an efficient method to improve the curb inlet efficiency only cutting the curb inlet because E_{ci} only increases 0.39–6.01%. The cut depth from 0.1 to 0.15 m has really no influence on the 100% interception curb inlet length and the curb inlet efficiency based on the simulation results.

5.3.3 100% Interception Curb Inlet Lengths for the Road-Curb Cut Scenarios

Figure 5.8 shows the comparison of 100% interception curb inlet lengths for the undepressed inlets and the road-curb cut inlets with w = 0.05 m and 0.10 m from 100 modeling cases by varying S_x and Q_{in}. The percentage changes of L_T between the road-curb cut cases with w = 0.05 m (R1) and the undepressed cases (UD) range from -3.92% to -1.47% with the mean change and its standard deviation of -2.31% and 0.48%. The percentage changes of L_T between the road-curb cut cases with w = 0.1 m (R2) and the undepressed cases (UD) range from -6.54% to -3.08% with the mean change and its standard deviation of -4.45% and 0.78%. The 100% interception curb inlet length sequence from the largest to smallest was UD > R1 > R2. The maximum reduction of L_T for R1 and R2 cases in comparison to corresponding UD cases is 0.15 and 0.25 m, respectively.

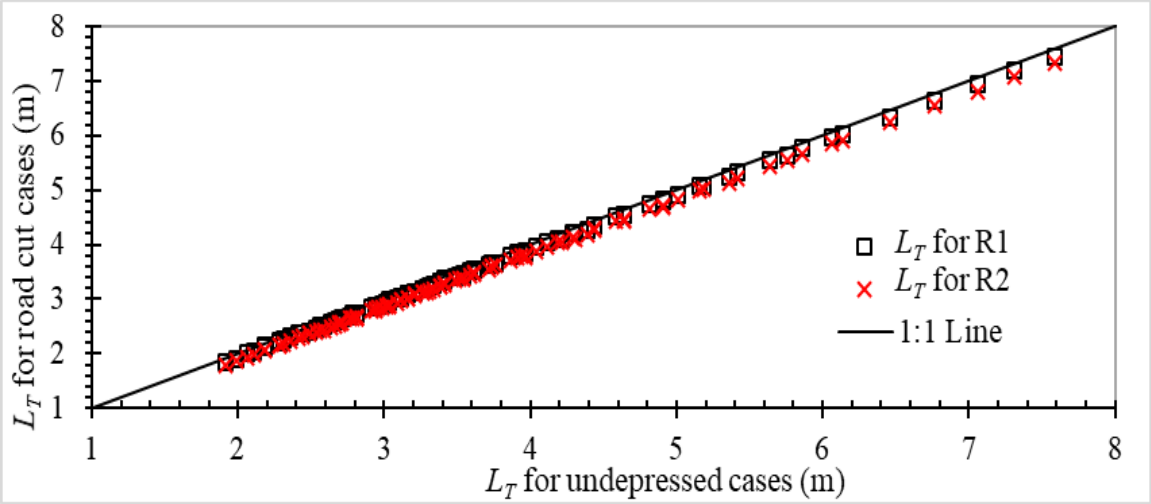

Figure 5.8. Comparison of 100% interception curb inlet length for undepressed, R1 (w = 0.05 m), and R2 (w = 0.10 m) cases.

5.3.4 Curb Inlet Efficiencies for the Road-Curb Cut Scenarios

Figure 5.9a shows the comparison of curb inlet efficiency for undepressed cases, road-curb cut cases with w = 0.05 m and 0.10 m. The change of curb inlet efficiency between the road-curb cut cases (R1) and undepressed cases (UD) range from 2.79% to 14.16% with the average ± standard deviation equal to 8.21 ± 2.55%. The percentage change of curb inlet efficiency between road cut cases (R2) and undepressed cases (UD) range from 4.29% to 27.88% with the average ± standard deviation equal to 15.63 ± 5.16%.

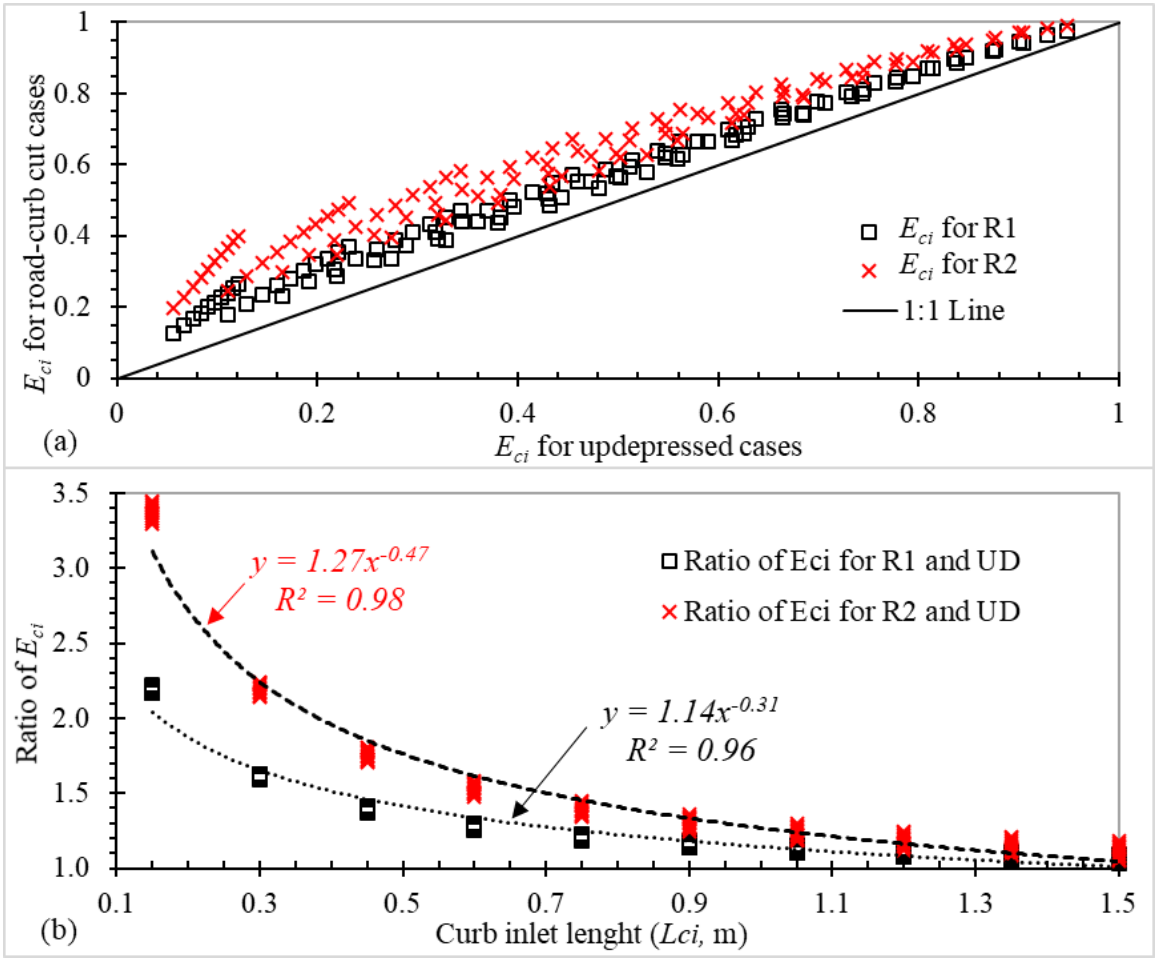

Figure 5.9. (**a**) comparison of curb inlet efficiency for undepressed UD, the toad-curb cut R1 (w = 0.05 m), and R2 (w = 0.10 m) modeling cases when Q_{in} = 10 L/s, (**b**) ratio of curb inlet efficiency for R1 and R3 cases versus curb inlet length.

Figure 5.9b plots the ratio of curb inlet efficiency for the road-curb cut cases and corresponding undepressed cases versus the curb inlet length. It is clear shows that the curb inlet efficiency was largely improved for small curb inlet length. For bioretention facilities in Spong City projects (Figure 5.1), many curb inlets have short opening lengths. When L_{ci} is 0.15 m (~6 inches) and 0.3 m (~12 inches), the curb inlet efficiency is average 2.19 and 3.37 times of E_{ci} for undepressed inlets, respectively, when Q_{in} = 10 L/s. The road cut width w increases from 0.05 m (R1) to 0.10 m (R2), E_{ci} for R2 is 1.0–1.55 times of E_{ci} for R1.

Figure 5.10 shows the curb inlet efficiency E_{ci} for the undepressed cases, the road-curb cut cases with w = 0.05 m and 0.10 m versus the ratio of L_{ci}/L_T. The dark line in Figure 5.10 shows the calculated efficiencies using the newly developed equation (Equation 3.13) in Chapter 3.

For Equation (3.13), the root mean square error (RMSE) between fitted and simulated E_{ci} is 3.93%. The differences of curb inlet efficiency between the calculated and simulated results for undepressed cases (UD) range from -2.43% to 7.43% with the average $\pm$ standard deviation equal to 4.06 $\pm$ 2.34%. The calculated E_{ci} is therefore on the average 4.06% larger than the simulated E_{ci} (Figure 5.10). Its RMSE is 4.68%, just slightly larger than RMSE of Equation (3.13). It shows the calculated results with Equation 3.13 match well with the undepressed cases.

The differences of curb inlet efficiency between the calculated and simulated results for the road-curb cut cases (R1) range from -10.70% to 0.35% with the average $\pm$ standard deviation equal to -3.25 $\pm$ 2.28%, which is within RMSE of Equation 3.13. The percentage change of curb inlet efficiency between the calculated and simulated results for road-curb

cut cases (R2) range from -24.07% to -4.86% with the average ± standard deviation equal to -9.79 ± 4.50%. Therefore, the Equation (3.13) underestimated the curb inlet efficiencies for the road-curb cut cases with w =0.01 m, and the average difference is more than twice of the RMSE of Equation (3.13).

A new regression equation of E_{ci} to L_{ci}/L_T for R2 cases was developed:

$$E_{ci} = 1 - \left[1 - \left(\frac{L_{ci}}{L_T}\right)\right]^{3.44} \tag{5.1}$$

Equation 5.1 has an RMSE of 6.26%. Equation 5.1 was developed only based on those 100 cases with longitudinal slope equal to 1%. A general equation that can be used to calculate the road-cut curb inlet efficiency with a wide range of parameters for the road surface curb inlet and cut width still needs to be determined based on more simulation cases in the future study.

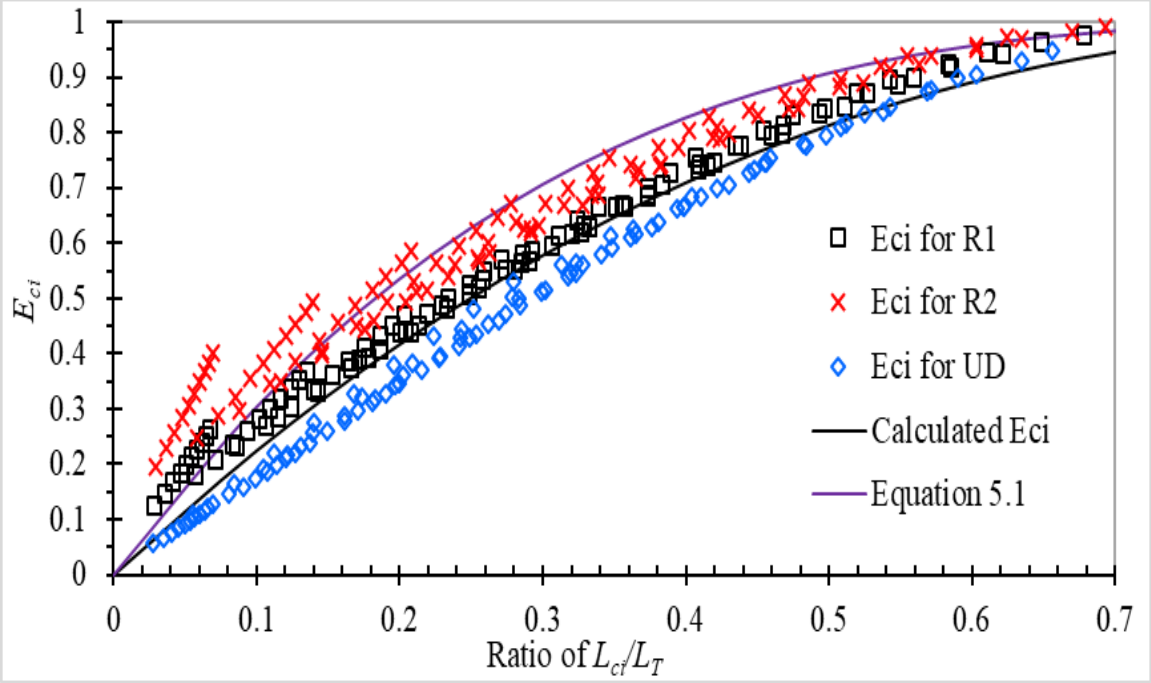

Figure 5.10. Curb inlet efficiency for undepressed UD, the road-curb cut R1 (w = 0.05 m) and R2 (w = 0.10 m) modeling verse ratio of L_{ci}/L_T.

5.4 Summary and Conclusions

The deep-cut (DC) curb inlets were used in some of the retrofit sponge-city projects for that they were easily implemented and based on engineer's or design's field experience. Two kinds of retrofit scenarios were simulated in this study: 1) the deep cut is made only over the width (0.01 m) of the curb inlet; 2) both the curb inlet and a small part of road surface have a deep cut. For the first scenario, two hundred cases with one S_o, 10 S_x, and 10 Q_{in} were used to determine the 100% interception curb inlet lengths L_T with a cut depth d equal to 0.1 m and 0.15 m. Another two hundred cases with the same longitude slope and 10 S_x plus 10 curb inlet lengths L_{ci} were used to determine the curb inlet efficiencies E_{ci}.

For the second scenario, two hundred cases with one S_0, 10 S_x, and 10 Q_{in} to determine the 100% interception curb inlet lengths with a cut width w on the road surface equal to 0.05 m and 0.1 m. Another two hundred cases with the same S_0 and 10 S_x plus 10 L_{ci} were used to determine E_{ci}. Therefore, a total of eight hundred modeling cases for the deep-cut curb inlets were designed and modeled using the FullSWOF-ZD program.

These cases were compared with the results in Chapter 3 to explore and quantify the efficiency improvement by cutting the curb inlet simply. The percentage changes of L_T between the deep-cut cases (D1 and D2) and the undepressed cases (UD) with the same S_0, S_x and Q_{in} range from -1.09% to 0.00% with the mean absolute percentage change equal to -0.25%. The 100% interception curb-inlet lengths for the 200 deep-cut cases with different cut depths were basically the same as L_T for corresponding undepressed cases with the same cross slope and upstream inflow. It means if the deep cut is only made over the curb inlet width, the deep-cut depth (d = 0, 0.05, and 0.1 m) does not make any difference on L_T. The E_{ci} changes between the deep-cut cases (D1 and D2) and the undepressed cases

(UD) range from 0.4% to 6.0% and are greater than zero so that the deep cut only increases E_{ci} a few percents. Therefore, it is not an efficient method to improve the curb inlet efficiency only cutting the curb inlet because E_{ci} only increases up to 6.0%.

The 100% interception curb inlet length sequence from the largest to smallest was UD > R1 > R2. The maximum reduction of L_T for R1 and R2 cases in comparison to corresponding UD cases is 0.15 and 0.25 m, respectively. The increases of curb inlet efficiency between the road-curb cut cases R1 or R2 and the undepressed cases (UD) range from 2.79% to 14.2% and 4.3% to 27.9%, respectively. The road-curb cut cases improved the curb inlet efficiency in a large extent which could be used in the SPC retrofit projects. However, a general equation used to design and evaluate the road-curb cut inlets should be developed based on more simulation cases with a wide range of input parameters.

Chapter 6. Summary, Conclusions, and Future Study

6.1 Summary

To achieve the first objective of the study, the particle tracking method PTM module was added into the 2D overland flow simulation program based on the open-source program FullSWOF_2D that can be used to estimate the time of concentration for impervious and pervious surfaces. The new program called FullSWOF-PTM was tested using published rainfall and runoff data, and simulated hydrographs match well with observed data, which proves it can predict the overland flow accurately. Four hundred forty-six impervious modeling cases using the combinations of model input parameters (longitudinal slope S_0, length L, Manning's roughness n, and rainfall intensity i) were developed and simulated to explore T_{ci} of overland flow on impervious surfaces first. The travel time of 85% particles to arrive at the drainage outlet (T_{r_p85}) was calculated by FullSWOF-PTM for determining the time of concentration of impervious and pervious surfaces in this study. A regression equation of T_{ci} was derived using the MLR regression method and as a power function of $\frac{Ln}{\sqrt{S_0}}$ and i. The derived impervious surface T_{ci} equation match well with T_{r_p85} and correlates well with T_{ci} from other five published equations, which further proves FullSWOF-PTM can be used to estimate T_{cp} of overland flow on pervious surfaces.

Seven hundred fifty (750) pervious modeling cases were developed and simulated to explore the T_{cp} equation. T_{cp} is considered as T_{r_p85} of pervious surfaces determined from FullSWOF-PTM minus the ponding time t_p. A regression equation for T_{cp} was developed using simulated T_{rp_p85} and calculated t_p from 750 pervious modeling cases, which include

combinations of soil infiltration parameters (K, φ, and $\Delta\theta$) in addition to surface geometry and roughness parameters. The new T_{ci} and T_{cp} equations can be used to determine the time of concentration for urban drainage and road-bioretention facilities design.

To achieve the second objective, the updated FullSWOF-ZG program based on the open-source overland flow simulation program FullSWOF_2D was tested with 20 different locally depressed Texas type D curb inlet cases to simulate inlet efficiency. The differences between simulated and observed E_{ci} ranged from −2.28% to 4.21% with the average $\pm$ standard deviation being 1.10% $\pm$ 1.67%. The FullSWOF-ZG program was also validated using 80 laboratory tests to simulate the curb inlet length of 100% interception with an RMSE equal to 0.27 m and MAPE equal to 6.04%. These validation runs indicated that the FullSWOF-ZG program can accurately simulate the overland flow through the curb inlets with the high agreement and small error with observed ones so that it can be used to determine L_T and E_{ci}. One thousand (1000) undepressed curb inlet modeling cases of the road with 10 S_0, 10 S_x, and 10 Q_{in} were established and modeled to determine L_T, and then a new estimation equation of L_T was developed by the regression with the input parameters. The second set of 1000 road modeling cases of undepressed curb inlets with 10 S_0, 10 S_x, and 10 L_{ci} and a constant Q_{in} (10 L/s) were established and modeled to determine E_{ci}, and then a new estimation equation of E_{ci} was developed as a function of L_{ci}/L_T. The newly developed L_T equation was compared with three previous methods, including Izzard (1950), HEC-22 (2009), and Muhammad (2018) for predicting L_T for 1000 undepressed curb inlet cases. Finally, L_T and E_{ci} equations for four methods were applied together to predict E_{ci} for 10,000 curb-inlet cases of all ten S_0, S_x, Q_{in}, and L_{ci} combinations listed in Table 3.1. Predicted E_{ci} values for all 10,000 cases from Izzard (1950), HEC-22 (2009),

and Muhammad (2018) method had RMSE < 8.5% and MAPD < 13% in comparison with ones from the newly developed L_T and E_{ci} equations in this study. The newly developed equations gave more accurate estimations of L_T and E_{ci} over a wide range of input parameters. These equations can be applied to design urban drainage and road bioretention facilities since they were developed using a large number of simulation runs with diverse input parameters, but previous methods often overpredict the gutter flow Q_{g100} of total interception when longitudinal slope S_0 is small. In future studies, the equations used to evaluate the efficiency of locally depressed and continuously depressed curb inlets can be developed using simulation results from the FullSWOF-ZG program. The hydraulic-performance-based equations for different types of curb inlets should be promoted for the design of road bioretention facilities, instead of only considering landscape and safety perspective.

The open-source Full Shallow-Water equations for Overland Flow in two-dimensional (FullSWOF_2D) program, which applies the uniform rainfall and infiltration parameters to the whole simulation domain, was revised to include 2D plane zones with different rainfall and infiltration parameters and a 2D-1D grate-inlet flow interception module. The FullSWOF-ZD program was tested with the overland flow of 8 pervious surface rainfall-runoff events and 20 impervious roads with type C curb inlet to study whether the program could accurately simulate the overland flow on pervious and impervious surface and predict curb inlet interception efficiency with accuracy. Twenty road-bioretention strip or RBS modeling cases were designed based on the commonly used parameters (longitudinal and cross slopes, curb opening length, soil infiltration parameters, the bioretention depression depth, and the overflow height) and evaluated with FullSWOF-ZD. The

simulation results were analyzed and demonstrated that the RBS hydrological performance, i.e., to intercept then infiltrate the runoff, was jointly influenced by several parameters. Even the complex relationship between the RBS performance and all input parameters were not fully explored by using only 20 cases; some useful insights and conclusions were obtained from numerical simulations presented in Chapter 4.

The deep-cut curb inlets have been implemented in some retrofit projects in China by some engineers and designers who thought they could improve the curb inlet efficiency. The E_{ci} improvement of the deep cut over the curb inlet only and the road-curb cuts with different road widths was explored and quantified with numerical simulations of two-dimensional overland flow on the road surfaces with curb inlets. The road-curb deep cuts were also simulated when the deep cut was cross the curb inlet width and a small distance (width of 0.05 and 0.10 m) into the road surface. The 100% interception length and inlet efficiencies were determined and analyzed using FullSWOF-ZG program.

6.2 Conclusions

(1). A regression equation of T_{cp}, Equation (2.11) for the time of concentration on pervious surfaces was developed using simulated results from 750 pervious modeling cases. Equation (2.11) includes T_{ci} for an equivalent impervious surface using ($i - K$) as effective rainfall and additional travel time due to infiltration (T_{rs}) to slow down the runoff movement as a function of rainfall intensity and the soil infiltration parameters (K, φ, and $\Delta\theta$). Equation (2.11) can be used for both impervious and pervious surfaces. The derived T_{cp} equation has higher R^2 and smaller RMSE compared to Akan's equation as well as wide ranges of input parameters.

(2). The newly developed L_T and E_{ci} equations were compared with three previous methods, including Izzard (1950), HEC-22 (2009), and Muhammad (2018) for 1000 undepressed curb inlet cases. Finally, L_T and E_{ci} equations for four methods were applied together to predict E_{ci} for 10,000 curb-inlet cases of all ten S_0, S_x, Q_{in}, and L_{ci} combinations listed in Table 3.1. Predicted E_{ci} values for all 10,000 cases from Izzard (1950), HEC-22 (2009), and Muhammad (2018) method had RMSE < 8.5% and MAPD < 13% in comparison with ones from the newly developed L_T and E_{ci} equations in this study. The newly developed equations gave more accurate estimations of L_T and E_{ci} over a wide range of input parameters. These equations can be applied to design urban drainage and road bioretention facilities since they were developed using a large number of simulation runs with diverse input parameters.

(3) When the road, curb inlet, and bioretention strip were modeled together as an integral system, it was found that the RBS's curb inlet could be the bottleneck of its hydrologic performance and should be designed to improve inlet interception efficiency. The curb inlet and road grate inlet combination is necessary for continuous RBS because the road surface runoff could not be 100% intercepted by the curb inlet alone.

(4) The 100% interception curb-inlet lengths for the 200 deep-cut cases with different cut depths were basically the same as L_T for corresponding undepressed cases with the same cross slope and upstream inflow. It means if the deep cut is only made over the curb inlet width, the deep-cut depth (d = 0.05, and 0.1 m) does not make any difference on L_T. Therefore, it is not an efficient method to improve the curb inlet efficiency only making a cut at the curb inlet because E_{ci} only increases up to 6.0%. The 100% interception curb inlet length sequence from the largest to smallest was UD > R1 (the road cur width w = 0.05

m) > R2 (w = 0.10 m). The increases of curb inlet efficiency between the road-curb cut cases R1 or R2 and the undepressed cases (UD) range from 2.79% to 14.2% and 4.3% to 27.9%, respectively. The road-curb cut cases improved the curb inlet efficiency in a large extent which could be used in the SPC retrofit projects. However, a general equation used to design and evaluate the road-curb cut inlets should be developed based on more simulation cases with a wide range of input parameters.

6.3 Future study

The peak discharge Q_p for the pervious surface could be evaluated using the FullSWOF-PTM to develop the model for the pervious surface cases. The equation used to determine Q_p could be developed based on simulation results of a large number of modeling cases varying surface geometry parameters (longitudinal slope S_0, roughness coefficient n, and length L), surface/soil infiltration parameters (Green-Ampt model), and rainfall intensity i. The relationship between Q_p and surface geometry parameter $\frac{Ln}{\sqrt{S_0}}$ and i as well as the infiltration parameter K, φ, and $\Delta\theta$ could be developed using multiple linear regression method. The peak discharge for pervious surfaces also could be used for the urban drainage and green infrastructure design.

The curb inlet efficiency under the rainfall situations could be evaluated using the FullSWOF-ZG program for that the program could simulate the whole rainfall-runoff generation and concentration process. The difference in curb inlet efficiency under rainfall and upstream inflow situations could be compared and evaluated based on the simulation results. Currently used equations to evaluate the efficiency of local depressed and composite cross slope curb inlets are complex to implement in these two kinds of curb inlet

design. The equations that accurately evaluate the efficiencies of these two kinds of curb inlets and are easy to use in the curb inlet design practices need to be developed in the future study. The factors that influence the curb inlet performance should also be determined based on the simulation results or laboratory experiments. For example, the influence of upstream and downstream transition lengths on the local depressed curb inlet performance is not clear yet. These detailed hydraulic problems for curb inlet design and evaluation should be explored with the help of numerical simulation models. The risk of road safety and transportation should also be considered for the local depressed curb inlet design and evaluated in the future study.

The FullSWOF-ZG can only simulate the overland flow on the surface while no drainage pipe module was coupled in the program. In the urban stormwater and flood simulation, the drainage pipe is a big portion of the stormwater management and flood control system. In the future study, the FullSWOF-ZG could be coupled with the widely used stormwater management model (SWMM) to enable it to handle the complex 1D-2D coupled situations in urban stormwater management. The FullSWOF-ZG program could be further developed to take consideration of the transportation risk in an urban area for that the road flood has a big influence on transportation. The FullSWOF-ZG could be further developed to build an alert system used in the urban transportation control system. Finally, the FullSWOF-ZG program could be the cornerstone of the flood resilient city which take the consideration of urban stormwater management, real-time control, and flood risk alert together.

References

Abily, M., Bertrand, N., Delestre, O., et al. (2016a). "Spatial Global Sensitivity Analysis of High Resolution classified topographic data use in 2D urban flood modelling." *Environmental Modelling & Software*, 77, 183-195.

Abily, M., Delestre, O., Amossé, L., et al. (2016b). "Use of 3D classified topographic data with FullSWOF for high resolution simulation of a river flood event over a dense urban area." *arXiv preprint arXiv:1603.07463*, 3-5.

Akan, A. O. (1985). "Similarity solution of overland flow on pervious surface." *Journal of Hydraulic Engineering*, 111(7), 1057-1067.

Akan, A. O. (1986). "Time of concentration of overland flow." *Journal of Irrigation and Drainage Engineering*, 112(4), 283-292.

Akan, A. O. (1989). "Time of concentration formula for pervious catchments." *Journal Of Irrigation and Drainage Engineering*, 115(4), 733-735.

Akan, A. O. (2006). *Open channel hydraulics*, Elsevier, Butterworth-Heinemann.

Audusse, E., Bouchut, F., Bristeau, M.-O., et al. (2004). "A fast and stable well-balanced scheme with hydrostatic reconstruction for shallow water flows." *SIAM Journal on Scientific Computing*, 25(6), 2050-2065.

Barré de Saint-Venant, A. J. C. (1871). "Théorie du mouvement non permanent des eaux, avec application aux crues des rivières et à l'introduction des marées dans leurs lits." *Comptes Rendus des séances de l'Académie des Sciences*, 73, 237-240.

Bensabat, J., Zhou, Q., and Bear, J. (2000). "An adaptive pathline-based particle tracking algorithm for the Eulerian–Lagrangian method." *Advances in Water Resources*, 23(4), 383-397.

Bondelid, T. R., McCuen, R. H., and Jackson, T. J. (1982). "Sensitivity of SCS Models to Curve Number Variation." *JAWRA Journal of the American Water Resources Association*, 18(1), 111-116.

Bouchut, F. (2004). *Nonlinear stability of finite Volume Methods for hyperbolic conservation laws and Well-Balanced schemes for sources*, Springer Science & Business Media.

Bristeau, M.-O., and Coussin, B. (2001). "Boundary Conditions for the Shallow Water Equations solved by Kinetic Schemes." INRIA.

Brown, S., Stein, S., and Warner, J. (2009). "Urban drainage design manual: hydraulic engineering circular No. 22 (FHWA-NHI-10-009, HEC-22)." National highway institute, Colorado.

Chapman, C., and Horner, R. R. (2010). "Performance assessment of a street-drainage bioretention system." *Water Environment Research*, 82(2), 109-119.

Chatterjee, S., and Simonoff, J. S. (2013). *Handbook of regression analysis*, John Wiley & Sons.

Chen, X. (2004). "Research on classification system of urban road in Shanghai (in Chinese)." *Urban Transport of China*, 2(1), 39-45.

Cheng, H. P., Cheng, J. R., and Yeh, G. T. (1996). "A particle tracking technique for the Lagrangian-Eulerian finite element method in multi-dimensions." *International Journal for Numerical Methods in Engineering*, 39(7), 1115-1136.

Cheshmehzangi, A. (2016). "China's New-Type Urbanisation Plan (NUP) and the foreseeing challenges for decarbonization of cities: a review." *Energy Procedia*, 104, 146-152.

Chow, V. T. (1959). *Open channel hydraulics*, McGraw-Hill Book Company, Inc; New York.

Chow, V. T., Maidment, D. R., and Mays, L. W. (1988). *Applied hydrology*, McGraw Hill, New York.

Comport, B. C., and Thornton, C. I. (2012). "Hydraulic efficiency of grate and curb inlets for urban storm drainage." *Journal of Hydraulic Engineering*, 138(10), 878-884.

Control, D. N. R. a. E. (2005). "Green technology: the Delaware urban runoff management approach." *Standards, specifications and details for green technology BMPs to minimize stormwater impacts from land development*, Delaware department of natural resources and environmental control, Division of soil and water conservation, Dover, Delaware, 93.

Cordes, C., and Kinzelbach, W. (1992). "Continuous groundwater velocity fields and path lines in linear, bilinear, and trilinear finite elements." *Water resources research*, 28(11), 2903-2911.

Cordier, S., Coullon, H., Delestre, O., et al. "FullSWOF Paral: Comparison of two parallelization strategies (MPI and SKELGIS) on a software designed for hydrology applications." *Proc., ESAIM: Proceedings*, EDP Sciences, 59-79.

Davis, A. P. (2008). "Field performance of bioretention: Hydrology impacts." *Journal of Hydrologic Engineering*, 13(2), 90-95.

Davis, A. P., Hunt, W. F., Traver, R. G., et al. (2009). "Bioretention technology: Overview of current practice and future needs." *Journal of Environmental Engineering*, 135(3), 109-117.

Delestre, O., Darboux, F., James, F., et al. (2014). "FullSWOF: A free software package for the simulation of shallow water flows." *arXiv 2014, e-print arXiv:1401.4125*.

Delestre, O., Lucas, C., Ksinant, P. A., et al. (2013). "SWASHES: a compilation of shallow water analytic solutions for hydraulic and environmental studies." *International Journal for Numerical Methods in Fluids*, 72(3), 269-300.

Deng, Z. Q., De Lima, J. L. M. P., and Singh, V. P. (2005). "Transport rate-based model for overland flow and solute transport: Parameter estimation and process simulation." *Journal of Hydrology*, 315(1), 220-235.

Dietz, M. E. (2007). "Low impact development practices: A review of current research and recommendations for future directions." *Water, air, and soil pollution*, 186(1-4), 351-363.

Dietz, M. E., and Clausen, J. C. (2006). "Saturation to improve pollutant retention in a rain garden." *Environmental science & technology*, 40(4), 1335-1340.

Diskin, M., and Nazimov, N. (1996). "Ponding time and infiltration capacity variation during steady rainfall." *Journal of Hydrology*, 178(1-4), 369-380.

Esteves, M., Faucher, X., Galle, S., et al. (2000). "Overland flow and infiltration modelling for small plots during unsteady rain: numerical results versus observed values." *Journal of hydrology*, 228(3), 265-282.

Fang, X., Jiang, S., and Alam, S. R. (2009). "Numerical simulations of efficiency of curb-opening inlets." *Journal of Hydraulic Engineering*, 136(1), 62-66.

Fiuzat, A., Soares, C., and Sill, B. (2000). "Design of curb opening inlet structure."

García Serrana, M., Gulliver, J. S., and Nieber, J. L. (2017). "Non-uniform overland flow-infiltration model for roadside swales." *Journal of Hydrology*, 552(Supplement C), 586-599.

George's, C. P. (1993). "Design manual for use of bioretention in stormwater management." *Prince George's County (MD) Government, Department of Environmental Protection. Watershed Protection Branch, Landover, MD*.

George's, C. P. (2002). "Bioretention manual." *Prince George's County (MD) Government, Department of Environmental Protection. Watershed Protection Branch, Landover, MD*.

Godlewski, E., and Raviart, P.-A. (2013). *Numerical approximation of hyperbolic systems of conservation laws*, Springer Science & Business Media.

Gourbesville, P., Cunge, J., and Caignaert, G. (2014). *Advances in Hydroinformatics-SIMHYDRO 2014*, Springer Singapore, Singapore.

Guo, J. C. (2006). "Design of street curb opening inlets using a decay-based clogging factor." *Journal of Hydraulic Engineering*, 132(11), 1237-1241.

Guo, J. C. Y. (1998). "Overland flow on a pervious surface." *Water International*, 23(2), 91-96.

Guo, J. C. Y., and MacKenzie, K. (2012). "Hydraulic efficiency of grate and curb-opening inlets under clogging effect (CDOT-2012-3)." Colorado Department of Transportation, DTD Applied Research and Innovation Branch, Denver, Colorado.

Hammonds, M. A., and Holley, E. (1995). "Hydraulic characteristics of flush depressed curb inlets and bridge deck drains (FHWA/TX-96/1409-1)." Texas department of transportation, Texas.

Hammonds, M. A., and Holley, E. R. (1995). "Hydraulic characteristics of flush depressed curb inlets and bridge deck drains." *Rep. No. 1409*, Texas department of transportation, Texas.

Hamouda, B., and Lahbassi, O. (2012). "Integration of pervious area stream flow in urban hydrological model." *Energy Procedia*, 18(Supplement C), 1573-1582.

Hatt, B. E., Fletcher, T. D., and Deletic, A. (2009). "Hydrologic and pollutant removal performance of stormwater biofiltration systems at the field scale." *Journal of Hydrology*, 365(3), 310-321.

Henderson, F. M., and Wooding, R. A. (1964). "Overland flow and groundwater flow from a steady rainfall of finite duration." *Journal of Geophysical Research*, 69(8), 1531-1540.

Hjelmfelt, A. (1978). "Influence of infiltration on overland flow." *Journal of Hydrology*, 36(1-2), 179-185.

Hodges, B. R., Barrett, M. E., Ashraf, M., et al. (2018). "Interception capacity of conventional depressed curb inlets and inlets with channel extension." Texas Department of Transportation, Austin, Texas, 54-57.

Hromadka II, T. V., McCuen, R. H., and Yen, C. C. (1987). "Comparison of overland flow hydrograph models." *ASCE, Journal of Hydraulic Engineering*, 113(11), 1422-1439.

Hunt, W., Jarrett, A., Smith, J., et al. (2006). "Evaluating bioretention hydrology and nutrient removal at three field sites in North Carolina." *Journal of Irrigation and Drainage Engineering*, 132(6), 600-608.

Izzard, C. F. "Hydraulics of runoff from developed surfaces." *Proc., Proc. of the 26th Annual Meetings of the Highway Research Board*, Highway Research Board, Washington, D.C., USA, 129-150.

Izzard, C. F. (1950). "Tentative results on capacity of curb opening inlets." *Proc., 29th Annual Conference of the Highway Research Board*, Highway Research Board, Washington, D. C., December 12-15, 1950, 11-13.

Jens, S. (1979). "Design of urban highway drainage." Federal Highway Administration, Washinton, D. C., 198-226.

Jia, H., Wang, Z., and Yu, S. L. (2016). "Opportunity and Challenge: China's Sponge City Plan." *Hydrolink*, 4, 100-102.

Jia, H., Wang, Z., Zhen, X., et al. (2017). "China's Sponge City construction: A discussion on technical approaches." *Frontiers of Environmental Science & Engineering*, 11(4), 18.

Johnson, F. L., and Chang, F. F. (1984). "Drainage of highway pavements: hydraulic engineering circular No. 12 (HEC-12)." Federal highway administration, McLean, Virginia, 39-64.

Johnstone, D., and Cross, W. P. (1949). *Elements of Applied Hydrology*, Ronald Press, New York.

KC, M., and Fang, X. (2015). "Estimating time parameters of overland flow on impervious surfaces by the particle tracking method." *Hydrological Sciences Journal*, 60(2), 294-310.

KC, M., Fang, X., Yi, Y.-J., et al. (2014). "Improved time of concentration estimation on overland flow surfaces including low-sloped planes." *Journal of Hydrologic Engineering*, 19(3), 495-508.

Kibler, D. F. (1982). "Desk‐Top Methods for Urban Stormwater Calculation." *Urban stormwater hydrology*, 87-135.

Kirpich, Z. P. (1940). "Time of concentration of small agricultural watersheds." *Civil Engineering*, 10(6), 362.

Kuichling, E. (1889). "The relation between the rainfall and the discharge of sewers in populous areas." *Transactions, American Society of Civil Engineers* 20(1), 1–56.

Leandro, J., and Martins, R. (2016). "A methodology for linking 2D overland flow models with the sewer network model SWMM 5.1 based on dynamic link libraries." *Water Science and Technology*, 73(12), 3017-3026.

Li, H., Ding, L., Ren, M., et al. (2017). "Sponge city construction in China: A survey of the challenges and opportunities." *Water*, 9(9), 594.

Li, M.-H., Sung, C., Kim, M., et al. (2011). "Assessing performance of bioretention boxes in hot and semiarid regions: Highway application pilot study." *Transportation Research Record: Journal of the Transportation Research Board*(2262), 155-163.

Li, M.-H., Swapp, M., Kim, M. H., et al. (2014). "Comparing bioretention designs with and without an internal water storage layer for treating highway runoff." *Water Environment Research*, 86(5), 387-397.

Li, W. H. (1954). "Hydraulic theory for design of stormwater inlets." *Proc., 33rd Annual Meeting of the Highway Research Board*, Highway Research Board, Washington, D.C., January 12-15, 1954, 83-91.

Li, X., Fang, X., Gong, Y., et al. (2018a). "Evaluating the road-bioretention strip system from a hydraulic perspective—case studies." *Water*, 10(12), 1778.

Li, X., Fang, X., Li, J., et al. (2018b). "Estimating time of concentration for overland flow on pervious surfaces by particle tracking method." *Water*, 10(4), 379.

Li, X., Li, J., Fang, X., et al. (2016). "Case studies of the sponge city program in China." *Proc., World Environmental and Water Resources Congress*, American Society of Civil Engineers, West Palm Beach, Florida, May 22–26, 2016, 295-308.

Liang, X. (2018). "Hydraulic calculation and design optimization of curb opening in Sponge City construction (in Chinese)." *China Water & Wastewater*, 34(2), 42-45.

Linsley, R. K., Kohler, M. A., and Paulhus, J. L. H. (1958). *Hydrology for Engineers*, McGraw Hill Publications, New York.

Lu, N. (1994). "A semianalytical method of path line computation for transient finite-difference groundwater flow models." *Water Resources Research*, 30(8), 2449-2459.

Lucke, T., and Nichols, P. W. B. (2015). "The pollution removal and stormwater reduction performance of street-side bioretention basins after ten years in operation." *Science of The Total Environment*, 536, 784-792.

MacCallan, R., and Hotchkiss, R. (1996). "Hydraulic Efficiency of Highway Stormwater Inlets: Final Report." Research Report NE-DOT.

Mangangka, I. R., Liu, A., Egodawatta, P., et al. (2015). "Performance characterisation of a stormwater treatment bioretention basin." *Journal of Environmental Management*, 150, 173-178.

MathWorks (2017). *MATLAB and Statistics Toolbox Release 2017a*, The MathWorks Inc., Natick, Massachusetts, United States.

McCuen, R. H., Wong, S. L., and Rawls, W. J. (1984). "Estimating urban time of concentration." *Journal of Hydraulic Engineering*, 110(7), 887-904.

Ministry of Housing and Urban-Rural Development. (2016). "Code for design of outdoor wastewater engineering."Beijing, China, 15.

Moglen, G. E. (2009). "Hydrology and impervious areas." *Journal of Hydrologic Engineering*, 14(4), 303-304.

Morgali, J. R., and Linsley, R. K. (1965). "Computer analysis of overland flow." *Journal Of Hydraulics Division*, 91(HY3), 81-100.

Muhammad, M. A. (2018). "Interception capacity of curb opening inlets." Doctor of Philosophy, University of Texas at Austin, Austin, Texas, USA.

Mulvany, T. J. (1851). "On the use of self-registering rain and flood gauges in making observations of the relations of rainfall and flood discharges in a given catchment." *Proceedings of the Institution of Civil Engineers of Ireland*, 4(2), 18-33.

Muzik, I. (1974). "Laboratory experiments with surface runoff." *Journal of the Hydraulics Division*, 100(4), 501-516.

NACTO (2017). *Urban Street Stormwater Guide*, Island Press.

National Bureau of Statistics of China. (2017). *China statistical yearbook-2017*, China Statistics Press, Beijing, China.

Nash, J. E., and Sutcliffe, J. V. (1970). "River flow forecasting through conceptual models part I — A discussion of principles." *Journal of hydrology*, 10(3), 282-290.

Niri, M. Z., Saghafian, B., Golian, S., et al. (2012). "Derivation of travel time based on diffusive wave approximation for the time-area hydrograph simulation." *Journal of Hydrologic Engineering*, 17(1), 85-91.

Olivera, F., and Maidment, D. R. (1999). "Geographic information systems (GIS)-based spatially distributed model for runoff routing." *Water Resources Research*, 35(4), 1155-1164.

Passeport, E., Hunt, W. F., Line, D. E., et al. (2009). "Field study of the ability of two grassed bioretention cells to reduce storm-water runoff pollution." *Journal of Irrigation and Drainage Engineering*, 135(4), 505-510.

Peugeot, C., Esteves, M., Galle, S., et al. (1997). "Runoff generation processes: results and analysis of field data collected at the East Central Supersite of the HAPEX-Sahel experiment." *Journal of Hydrology*, 188, 179-202.

Pollock, D. W. (1994). "User's Guide for MODPATH/MODPATH-PLOT, Version 3: A particle tracking post-processing package for MODFLOW, the U. S. Geological survey finite-difference ground-water flow model." U. S. Geological Survey, Reston, Virginia, 4-9.

Rawls, W. J., Brakensiek, D. L., and Miller, N. (1983). "Green-Ampt infiltration parameters from soils data." *Journal of hydraulic engineering*, 109(1), 62-70.

Russo, B., and Gómez, M. (2013). "Discussion of “hydraulic efficiency of grate and curb inlets for urban storm drainage” by Brendan C. Comport and Christopher I. Thornton." *Journal of Hydraulic Engineering*, 140(1), 121-122.

Schafer‐Perini, A. L., and Wilson, J. L. (1991). "Efficient and accurate front tracking for two‐dimensional groundwater flow models." *Water Resources Research*, 27(7), 1471-1485.

Schalla, F. E., Ashraf, M., Barrett, M. E., et al. (2017). "Limitations of traditional capacity equations for long curb inlets." *Transportation Research Record: Journal of the Transportation Research Board*, 2638(1), 97-103.

Starzec, M., Dziopak, J., Słyś, D., et al. (2018). "Dimensioning of Required Volumes of Interconnected Detention Tanks Taking into Account the Direction and Speed of Rain Movement." *Water*, 10(12), 1826.

State Council of the People's Republic of China. (2014). "National new-type urbanization plan (2014-2020)." <http://www.gov.cn/zhengce/2014-03/16/content_2640075.htm>. (Accessed March 29, 2018).

Stoolmiller, S., Ebrahimian, A., Wadzuk, B. M., et al. (2018). "Improving the design of curb openings in green stormwater infrastructure." *International Low Impact Development Conference*, Environmental & Water Resources Institute, Nashville, Tennessee, August 12-15, 2018, 168-176.

Su, D., and Fang, X. (2003). "Estimating traveling time of flat terrain by 2-dimensional overland flow model." The international symposium on shallow flows, Delft University of Technology, Netherlands.

Suk, H., and Yeh, G. T. (2010). "Development of particle tracking algorithms for various types of finite elements in multi-dimensions." *Computers & Geosciences*, 36(4), 564-568.

Teng, J., Jakeman, A., Vaze, J., et al. (2017). "Flood inundation modelling: A review of methods, recent advances and uncertainty analysis." *Environmental Modelling & Software*, 90, 201-216.

Todeschini, S. (2016). "Hydrologic and environmental impacts of imperviousness in an industrial catchment of northern Italy." *Journal of Hydrologic Engineering*, 21(7), 05016013.

Trowsdale, S. A., and Simcock, R. (2011). "Urban stormwater treatment using bioretention." *Journal of Hydrology*, 397(3-4), 167-174.

Tu, M.-C., and Traver, R. (2018). "Clogging impacts on distribution pipe delivery of street runoff to an infiltration bed." *Water*, 10(8), 1045.

Unterweger, K., Wittmann, R., Neumann, P., et al. (2015). "Integration of FullSWOF2D and PeanoClaw: adaptivity and local time-stepping for complex overland flows." *Recent Trends in Computational Engineering-CE2014*, Springer, 181-195.

Uyumaz, A. "Urban drainage with curb-opening inlets." *Proc., Ninth International Conference on Urban Drainage (9ICUD)*, American Society of Civil Engineers, Portland, Oregon, September 8-13, 2002, 1-9.

Viessman, W., and Lewis, G. L. (2003). *Introduction to hydrology*, Pearson Education, Upper Saddle River, N.J.

Wasley, R. J. (1961). "Hydrodynamics of flow into curb-opening inlets." *Journal of the Engineering Mechanics Division*, 87(4), 1-18.

Wong, T. S. W. (2005). "Assessment of time of concentration formulas for overland flow." *Journal of Irrigation and Drainage Engineering*, 131(4), 383-387.

Wooding, R. A. (1965). "A hydraulic model for the catchment-stream problem: I. Kinematic-wave theory." *Journal of hydrology*, 3(3-4), 254-267.

Woolhiser, D. A., and Liggett, J. A. (1967). "Unsteady, one-dimensional flow over a plane—The rising hydrograph." *Water Resources Research*, 3(3), 753-771.

Yu, S., and Jia, H. (2016). "China's ambitious Sponge City initiative: A monumental effort for green/gray infrastructure integration." *ASCE EWRI Currents*, 17(4), 8-9.

Zhang, W., and Cundy, T. W. (1989). "Modeling of two‐dimensional overland flow." *Water Resources Research*, 25(9), 2019-2035.